A Quasi-distributed Sensing Network Based on Wavelength-Scanning Time-division Multiplexed Fiber Bragg Gratings

Yunmiao Wang

Dissertation submitted to the faculty of the Virginia Polytechnic Institute and State University in partial fulfillment of the requirements for the degree of

Doctor of Philosophy
In
Electrical Engineering

Anbo Wang, Chair
Gary R. Pickrell
Ahmad Safaai-Jazi
Ting-Chun Poon
Yong Xu

August 28th, 2012
Blacksburg, Virginia

Keywords: Fiber Bragg gratings, Multiplexing, Optical fiber sensor, Quasi-distributed sensing, Structure health monitoring

A Quasi-distributed Sensing Network Based on Wavelength-Scanning Time-division Multiplexed Fiber Bragg Gratings

Yunmiao Wang

ABSTRACT

Structural health monitoring (SHM) has become a strong national interest because of the need of reliable and accurate damage detection methods for aerospace, civil and mechanical engineering infrastructure. Health monitoring of these structures usually requires the sensors to have such features as large area coverage, maintenance free or minimum maintenance, ultra-low cost per measurement point, and capability of operation in harsh environments. Fiber Bragg grating (FBG) has attracted considerable interest for this application because of its compactness, electromagnetic immunity, and excellent multiplexing capability. Several FBG multiplexing techniques have been developed to increase the multiplexing number and further reduce the unit cost. To the author's best knowledge, the current demonstrated maximum multiplexing number are 800 FBG sensors in a single array using optical frequency domain reflectometry (OFDR), whose maximum fiber span is limited by the coherence length of light source.

In this work, we proposed and demonstrated a wavelength-scanning time-division multiplexing (WSTDM) of 1000 ultra-weak FBGs for distributed temperature sensing. In comparison with the OFDR method, the WSTDM method distinguishes the sensors by different time delays, and its maximum operation distance, which is limited by the transmission loss of the fiber, can be as high as tens of kilometers. The strong multiplexing capability and low crosstalk of the ultra-weak FBG sensors was investigated through both theoretical analysis and experiment. An automated FBG fabrication system was developed for fast FBG fabrication. With this WSTDM method, we multiplexed 1000 ultra-weak FBGs for distributed temperature sensing. Besides the demonstrated temperature measurement, the reported method can also be applied to measure other parameters, such as strain, pressure.

Acknowledgements

I would like to express my deepest gratitude to my academic and research advisor Dr. Anbo Wang for his continuous encouragement, guidance and support in helping me to conduct and complete this work. I thank him for offering me such a good opportunity to study and work in an excellent research group with so many talented people, for enlightening me when I encounter difficulties in my research, for being a guild and model in my life. I would also like to extend my gratitude to my other committee members: Dr. Gary R. Pickrell, Dr. Ahmad Safaai-Jazi, Dr. Ting-Chun Poon and Dr. Yong Xu. Thank you for the valuable guidance, comments and support during this work.

I also owe a lot of thanks to the staff and students of CPT. Thanks Ms. Debbie Collins for her sincere administrative support. Very special thanks go to Dr. Jianmin Gong and Dr. Bo Dong for the valuable help and collaboration in the design and construction of the automated FBG production line. Thanks Miss Dorothy Y. Wang and Mr. Cheng Ma for your helpful discussions and valuable friendship. The friendship and encouragement from you make me a happy life. Thanks Dr. Kristie L. Cooper, Dr. Ming Han, Dr. Evan Lally, Dr. Yizheng Zhu, Dr. Zhuang Wang, Mr. Tyler Shillig, Mr. Michael Fraser, Mr. Keith Depew, Mr. Zhipeng Tian and Mr. Chennan Hu, for the knowledge and support.

Finally I want to express my deepest love to my parents and my husband, Wei. Thanks for your endless encouragement and support for me when I feel frustrated during the study.

Table of Contents

ABSTRACT ..... **ii**
Acknowledgements ..... **iii**
Table of Contents ..... **iv**
List of Figures ..... **vi**
List of Tables ..... **ix**
Chapter 1 Introduction **1**
1.1 Motivation 1
1.2 Optical fiber sensors 2
1.2.1 Intensity-modulated sensors: 3
1.2.2 Wavelength-modulated sensors 4
1.2.3 Polarization-modulated sensors 6
1.2.4 Phase-modulated sensors: 6
1.3 Configuration of optical fiber sensors 8
1.3.1 Single point fiber optic sensor 9
1.3.2 Fully distributed fiber optic sensor 10
1.3.3 Quasi-distributed fiber optic sensor 13
1.4 Summary and scope of research 14
Chapter2 Wavelength-scanning time division multiplexed fiber Bragg grating sensor network **16**
2.1 Introduction to fiber Bragg gratings 16
2.2 Modeling of fiber Bragg gratings 17
2.3 Multiplexing techniques of FBG sensor network 20
2.3.1 Time division multiplexing 21
2.3.2 Wavelength division multiplexing 22
2.3.3 Frequency division multiplexing 22
2.3.4 Other multiplexing schemes. 23
2.4 Wavelength-scanning time division multiplexing scheme 24
2.4.1 Multiplexing capacity 25
2.4.2 Crosstalk analysis 26
Chapter 3 Construction of an automated fiber Bragg grating fabrication system **34**

3.1 Hydrogen loading of optical fibers 34
3.2 Coating removal 37
3.2.1 Determining the power of CO_2 laser 38
3.2.2 Determining the de-coating length 41
3.3 UV exposure 43
3.4 Translation system 46
3.4.1 System overview 46
3.4.2 Fiber forward mechanism 48
3.4.3 Electric magnet clamps 53
3.4.4 Fiber collection mechanism 54
3.5 FBG mass production system 56
3.5.1 Interface circuits box 57
3.5.2 Software design and program development 61
3.6 Calibration procedures 64
3.7 Performance of fabricated sensors 66
Chapter 4 WSTDM interrogation system 70
4.1 System overview 70
4.1.1 Pulse modulation 71
4.1.2 Signal amplification 72
4.1.3 System timing and trigger signals 74
4.1.4 Software implementation 77
4.2 Signal demodulation 81
4.2.1 Pulse location and pulse measurement 81
4.2 .2 Spectrum reconstruction 83
4.3 Experimental Results 86
4.3.1 Performance of the 1000-FBG sensor network 87
4.3.2 Temperature sensing test 90
Chapter 5 Conclusion 97
5.1 Conclusion 97
References 99

List of Figures

Figure 1.1 Categories of optical fiber sensor 3
Figure 1.2 Sensing theory of an intensity-modulated pressure optical sensor 4
Figure 1.3 Configuration of a blackbody fiber optic sensor 5
Figure 1.4 Illustration of a polarization-modulated fiber optic sensor 6
Figure 1.5 Illustration of Mach-Zehnder fiber optic interferometer 7
Figure 1.6 Illustration of an Fabry-Perot interferometer 8
Figure 1.7 Optical fiber sensor configuration 9
Figure 1.8 Spectrum of backscattered light of optical fiber 11
Figure 2.1 Illustration of FBG principle 16
Figure 2.2 Diagram of refractive index change along the fiber 17
Figure 2.3 Simulated reflection spectra of the FBGs with different grating length L 20
Figure 2.4 Configuration of a TDM FBG sensor network 21
Figure 2.5 Schematic of a WDM FBG sensor network 22
Figure 2.6 Illustration of an OFDR system 23
Figure 2.7 Schematic of WSTDM network 24
Figure 2.8 Returning power of a 1000-sensor array with different reflectivities 26
Figure 2.9 Spectral shading of the FBGs with different peak reflectivity Rg 28
Figure 2.10 Illustration of first order crosstalk 29
Figure 2.11 Illustration of the crosstalk of the 4^{th} FBG 30
Figure 2.12 First-order crosstalk error of a 1000-sensor array with different reflectivity 31
Figure 2.13 Simulation of reflective spectra of the FBGs with different peak reflectivity R_g including the crosstalk 32
Figure 3.1 Calculation of Bobbin Dimensions 35
Figure 3.2 Hydrogen Loading System Diagram 37
Figure 3.3 an optical fiber with (a) partially, (b) fully, removed coati 39
Figure 3.4 The reflection spectra of the FBGs whose fiber coating was removed with (a) CO2 ablation method and (b) mechanical stripping method 40
Figure 3.5 Configuration of a 120 copper mirror 41

Figure 3.6 (a) The bare fibers wound around a pulley and (b) The fibers with different de-coating length as compared to a dime. 42
Figure 3.7 (a) Experiment setup of the coating removal system (b) Surface of a de-coated fiber 43
Figure 3.8 Diffraction of an incident beam by a phase mask 45
Figure 3.9 UV exposure on the optical fiber through a phase mask 45
Figure 3.10 FBG writing system diagram 48
Figure 3.11 Fiber feeding system 49
Figure 3.12 (a) Stepper motor (b) Schematic of the stepper motor 49
Figure 3.13 Schematic of rotary stage driving circuit 52
Figure 3.14 Final version of the stepper motor driver circuit 53
Figure 3.15 Schematic of electric magnet driver 54
Figure 3.16 Electric magnet clamps 54
Figure 3.17 Schematic of the fiber collecting mechanism 55
Figure 3.18 Real fiber collection mechanism 56
Figure 3.19 Schematic of the automated FBG fabrication system 56
Figure 3.20 Schematic of the interface circuit bo 58
Figure 3.21 Front panel of interface circuit box 58
Figure 3.22 The external trigger signal of the Excimer lase 60
Figure 3.23 Picture of the Excimer laser 60
Figure 3.24 Block diagram of the automated FBG fabrication program 61
Figure 3.25 Graphic user interfaces (GUI) of the automatic FBG fabrication program 62
Figure 3.26 FBG spectrum calibration system 65
Figure 3.27 The typical spectrum of an ultra-weak FBG (-43.6 dB) 65
Figure 3.28 Returned pulses from the 100 FBGs 67
Figure 3.29 Resolved spectra of the FBGs with different peak reflectivities 68
Figure 3.30 Pulse intensities at different wavelength of the 100 FBGs 69
Figure 4.1 Interrogation system of a WSTDM sensor array 70
Figure 4.2 (a) The Electro-optical modulator (b) The electrical pulse generator 71
Figure 4.3 Temporal profile of a modulated 0.5ns pulsed light 72
Figure 4.4 Saturation of photo detector when optical gain is too high 73

Figure 4.5 (a) The output signal with the associated amplified-spontaneous –emission (ASE) noise (b) The output signal with the suppressed ASE noise 74
Figure 4.6 Timing of the system 75
Figure 4.7 Distortion of averaged signal induced by the unstable trigger 76
Figure 4.8 Two possible trigger signals of the interrogation system 77
Figure 4.9 The program diagram of interrogation system 78
Figure 4.10 Decoding a single FBG with the interrogation system 79
Figure 4.11 (a) The resolved spectrum of an FBG (b) The SNR of the resolved spectra as a function of the reflectivity of the FBGs 80
Figure 4.12 Illustration of the peak location method 82
Figure 4.13 Pulse area measurement 83
Figure 4.14 Normalized spectra of 12 FBGs 84
Figure 4.15 The average wavelength shifts of the resolved spectra with different SNR .. 86
Figure 4.16 The average wavelength shifts of the 1000 FBGs 87
Figure 4.17 The standard deviation (STD) of wavelength shift 88
Figure 4.18 The returned pulses from the two ends of the same sensor array 89
Figure 4.19 The reconstructed spectra of the 10th and the 870th FBGs 90
Figure 4.20 The experiment setup of the temperature measurement 92
Figure 4.21 Temperature measurement results of the 1000-FBG sensor array 92
Figure 4.22 the wavelength shift versus the temperature change 93
Figure 4.23 The temperature sensitivity of 17 FBGs 93
Figure 4.24 The Rmsd of the 17 FBGs 94
Figure 4.25 Information of 6^{th} FBG (a) Fitted curve of shift wavelength (b) Reconstructed spectra 95
Figure 4.26 Information of 7^{th} FBG (a) Fitted curve of shift wavelength (b) Reconstructed spectra 96

List of Tables

Table 3.1 FBGs with different de-coating lengths 42
Table 3.2 List of actuation modules of FBG automation system 47
Table 3.3 Current output with different control voltage 51
Table 3.4 The fabrication time of one FBG with different parameters 64

Chapter 1 Introduction

1.1 Motivation

Structural health monitoring (SHM) has become a strong national interest because of the need of reliable and accurate damage detection methods for aerospace, civil and mechanical engineering infrastructure. By monitoring geometric properties or material degradation, the performance of a system can be determined. The analysis based on the collected information can help to predict damage and deterioration of these structures, and further avoid accidents. Economic and life-safety issues are the primary driving force behind the development of structural health monitoring technology. For example, unpredicted shutdown of Intel Pentium III fabrication facility in New Mexico can cost Intel $10-$15 US million dollars per hour [1]; in 2010, the Gulf of Mexico oil spill was not only cost-prohibitive to the victims but also caused extensive damage to marine and wildlife habitats.

The foundation of SHM is to monitor structures using embedded or attached non-destructive sensors. SHM usually requires the sensors and measurement devices to have such features as large area coverage, minimum maintenance, ultra-low cost per measurement point, and often capability of operation in harsh environments of different kinds. Over the past decades, a number of technologies have been demonstrated, such as passive acoustic emission sensors, active ultrasonic sensors and so on [2-4]. Most of these technologies are semiconductor-based electronic sensors, like MEMS. These sensors can be made in a batch process so their cost can be extremely low [5, 6]. Also, with the assistance of wireless transmission, many sensors can be deployed to cover a large area. However, these sensors in general all have such serious limitations as susceptibility to electromagnetic interference (EMI), restriction to relatively low temperatures (mostly below 125^{o}C), and rather limited capability for sensor multiplexing [7, 8].

Many optical or optical fiber sensors have been investigated especially in the past decades for infrastructure monitoring. These sensors usually are insensitive to EMI,

often offer excellent resolution and accuracy, and many have much higher temperature capability. For example, Kim and Paik installed Fabry-Perot fiber optic sensors on the Sungsan Bridge in Seoul, Korea for strain measurement [9]. Todd et al. installed fiber Bragg grating (FBG) sensors on the I-10 bridge in southern New Mexico. Their results demonstrated that FBG sensors can be useful in monitoring traffic-induced loads [1]. Teral et al. proposed an optical time domain reflectometry (OTDR) method for measuring temperature along a power transmission line [1]. However, these sensors in general are more expensive than their electronic counterparts. This situation forces researchers to multiplex as many sensors as possible in a system so the cost per measurement point can be significantly lowered. To date, the multiplexing capability is still within hundreds of sensors along a single fiber cable [10]. In this work, we propose to develop a sensor technology that will increase the multiplexing capability by at least one order of magnitude. Further, this capability can be multiplied by many folds through sensor data fusion and computer networking so many thousands of sensors of different types in one system may become possible for real-time key infrastructure monitoring.

1.2 Optical fiber sensors

Optical fibers, emerging in the 1960s, have been used for a variety of sensing purposes, providing a measurement technology, which presents advantages over conventional methods in several areas [11]. Optical fiber sensors have the characteristics of small size, low weight, immunity to electromagnetic interference, chemical passivity and the capability of dense multiplexing and remote measurement. Meanwhile, the well-developed optical components and devices from the optical communication industry provide an economic convenience to the optical sensor industry.

Optical sensors can generally be classified into four categories based on different sensing parameters: intensity modulation, wavelength modulation, polarization modulation and phase modulation.

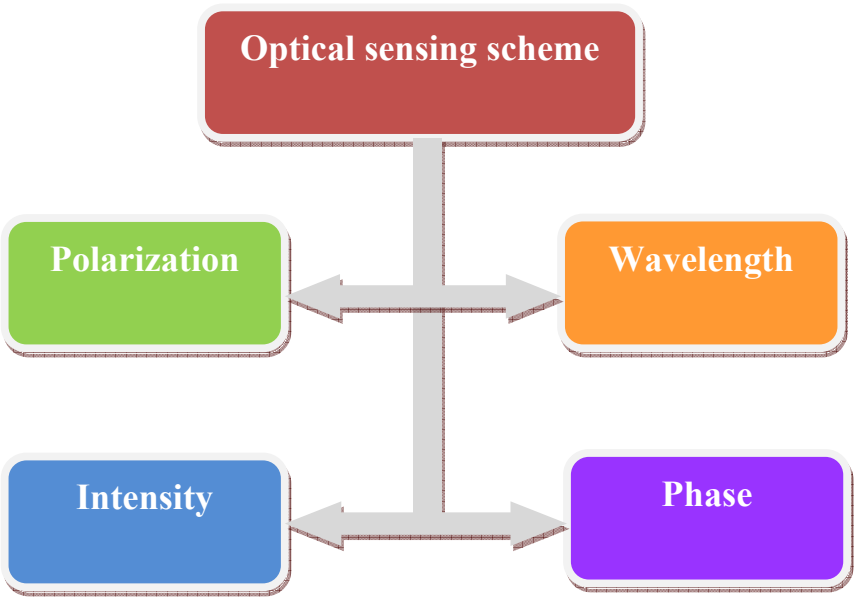

Figure 1.1 Categories of optical fiber sensor

1.2.1 Intensity-modulated sensors:

This method was employed in the early optical sensor development and featured with simplicity, and low cost [12]. The intensity of light launched into a sensor head is changed in accordance with the measurand. The intensity modulated light is detected by a light receiver and converted into an electrical signal. A change in the value of the electrical signal is proportional to the change of measurand. A wide variety of sensors such as pressure, mass and current sensors have been developed based on this modulation scheme [13, 14]. Figure 1.2 illustrates the sensing theory of an optical pressure sensor. Under the normal condition, the fiber is straight, and the photodetector receives high power. When a force is applied to the mechanical transducer outside the fiber, the change in pressure is transmitted to the micro-bending on the fiber. As a result, the induced transmission loss leads to a low output power.

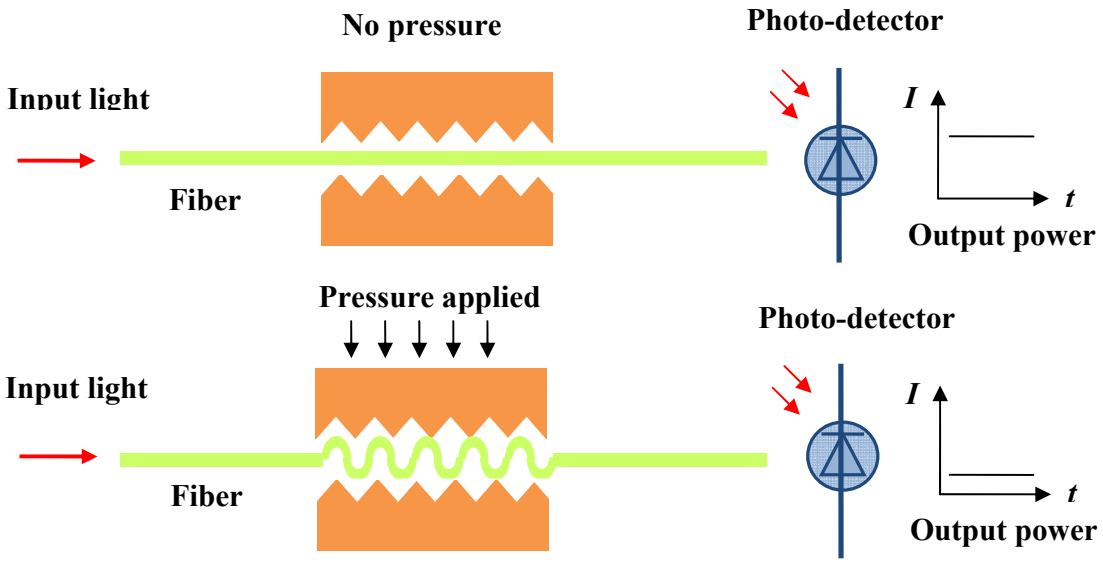

Figure 1.2 Sensing theory of an intensity-modulated pressure optical sensor

If the light source is modulated into pulses, corresponding to each input pulse, a series of pulses return in the time domain, and their intensities carry the information at the different distances. Distributed temperature measurement has been demonstrated based on optical time domain reflectometry [15, 16]. The major advantages of intensity-modulated sensors are the simple sensor design, easy signal processing algorithm and low cost. The limitation of these sensors is the need of some power reference to avoid errors arising from source instability, and variable losses in fibers and connectors.

1.2.2 Wavelength-modulated sensors

The wavelength modulation is a form of modulation at which the spectrum of the light from an optical sensor is changed by some characteristic of the measuring object. A broadband light source is usually used to interrogate the sensor. By the amplitude comparison at two (or several) fixed wavelength or continuous wavelength scanning, the spectral change is obtained. The typical optical sensors of this kind include fluorescence sensors, blackbody sensors and [17-19]. Fluorescence-based sensing has been demonstrated to be a significant technique in prominent fields such as fluorescence-activated cell sorting, DNA sequencing, high-throughput screening, and clinical diagnostics [20]. The general idea is to attach fluorescent material onto a fiber tip as a probe to detect some interested agent; after the reaction between the agent and the

attached material, the resultant fluorescent is captured by the same fiber and directed back to a receiver. Blackbody temperature sensors are based on the thermal radiation effect. As shown in figure 1.3, a blackbody cavity is created and connected to the end of a guide fiber. When temperature increases, it starts to glow and radiation spectrum has a blue shift. Detectors with narrow-band filters are used to characterize the profile of the radiation curve. This sensor based on sapphire is an ideal choice for applications where high temperature and high performance are a requirement.

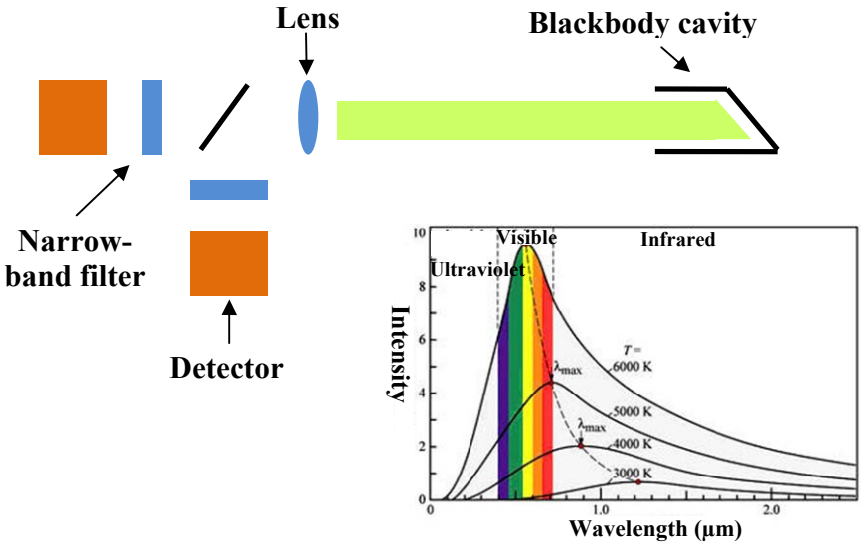

Figure 1.3 Configuration of a blackbody fiber optic sensor

Fiber Bragg gratings (FBGs) are most widely used wavelength-modulated sensors and have been applied for temperature and strain measurement in structural health monitoring. When a broadband light is launched into a fiber, only the light at a specific wavelength is reflected by an FBG, which is defined as the Bragg wavelength and can be changed by environment conditions. Thus by monitoring the wavelength shift of the Bragg wavelength, measurement of an interested parameter can be realized. The advantages of wavelength-modulated sensors include absolute measurement, and intrinsic wavelength-encoded operation, which eliminates the error induced by light power fluctuations. However, for the good sensitivity this configuration usually has the requirement on the bandwidth of the light source and the resolution of the spectrometer, which will increase the system cost.

1.2.3 Polarization-modulated sensors

The scheme realizes the measurement by detecting the change in the polarization of light introduced by a measurand. Under the external perturbation, such as stress or strain, optical fiber works like a linear retarder. Thus by detecting the change in the output polarization state, the external perturbation can be detected. Typically the system consists of a linearly polarized light source, an orthogonal linear polarizer formed crossed analyzer, and a detector. Figure 1.4 illustrates the experimental setup for a polarization-modulated fiber optic sensor. The polarized light from a light source is launched at 45 degrees to the preferred axes of a length of polarization-maintaining fiber. Under an external perturbation, the phase difference between the two polarizations along the two principal axes of the fiber is changed. So the amplitude of the detected signal depends on the change in the state of polarization introduced by the perturbation.

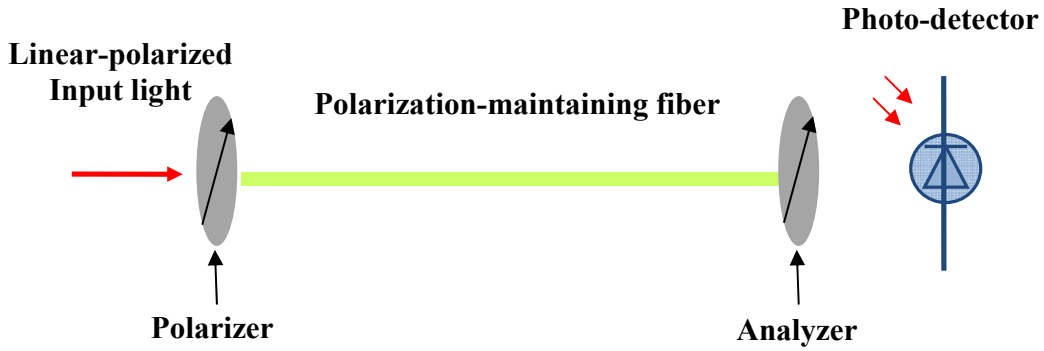

Figure 1.4 Illustration of a polarization-modulated fiber optic sensor

The method has been utilized in biomedical sensing [21] and electrical or magnetic field measurement [22]. The drawback of polarization modulation is the possible error induced by random changes in the birefringence of the fiber.

1.2.4 Phase-modulated sensors:

Phase modulation is the mechanism of all interferometric sensors where the optical phase of the light passing through the fiber is modulated by the measurand. Phase modulated sensors consist in general of a coherent laser, which injects light into two fiber optic beams. If the environment perturbs one or both fibers differently, a phase shift will occur that can easily be detected. Even an extremely small perturbation can be detected using

this technique, which means that the sensors can be made highly sensitive. Mach-Zehnder, Michelson, Sagnac and Fabry-Perot sensors are the most commonly used interferometric sensors. Figure 1.5 contains a schematic of a fiber optic Mach-Zehnder interferometer. The light from a laser is launched into an optical fiber and is split by a coupler into two fiber arms. One arm is treated as a sensing arm and exposed to the environment; while the other reference arm is isolated from the sensing environment. The environment condition introduces the strain in the optical fiber and further induces the optical path difference. Thus, the phase of the light received by the detectors has a shift. Michelson interferometer is often considered to be folded Mach-Zehnder interferometer. Michelson configuration uses only one coupler, so the light passes both two arms twice and the optical phase shift per unit length of fiber is doubled.

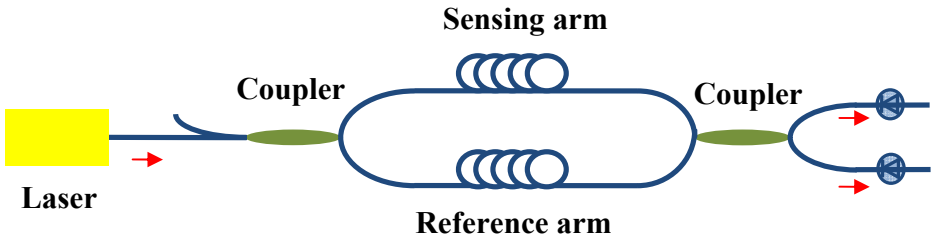

Figure 1.5 Illustration of Mach-Zehnder fiber optic interferometer

Sagnac and Fabry-Perot sensors are both based on multiple reflections. Sagnac interferometer is often called fiber-optic or laser gyroscope and primarily used for rotation velocity measurement; also it can be used for other measurements. It usually consists of a large number of loops of fibers and additional optical components. At each end of the loop, we simultaneously launch a short pulse of light. Both pulses would propagate at a constant velocity, regardless of the angular velocity of the loop. The pulse that travels in the same direction with the loop rotation experiences longer optical path; however the pulse that travels in the opposite direction with the loop rotation takes shorter time. As a result, loop rotation causes the optical path difference of the pulses in two directions, which can be detected. In the past several decades, significant effort has been taken in the development of fiber optic gyroscope.

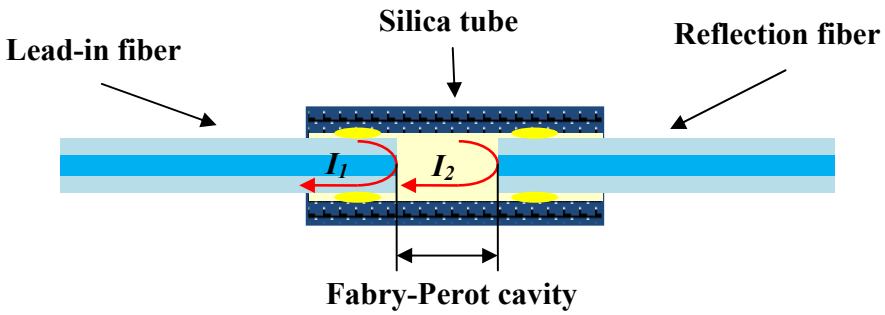

Figure 1.6 Illustration of an Fabry-Perot interferometer

Fiber optic Fabry-Perot interferometer (FFPI) is another widely-applied interferometric sensor. FFPI typically consists of two reflecting surfaces separated by a transparent plate as shown in figure 1.6. When a plane wave of monochromatic light is incident up on a Fabry-Perot cavity, interference is caused by the multiple reflections of light between the two reflecting surfaces. The peaks and valleys of the interference pattern correspond to constructive interference and destructive interference respectively. Based on the interference fringe modulation, the Fabry–Perot cavity length can be interpreted. Since environmental changes in temperature, pressure and or others can influence the Fabry-Perot cavity, sensing of these parameters can be realized by examining the cavity length change. With white-light interferometry, FFPI sensors can achieve high resolution, large dynamic range, and absolute measurement [23]. FFPIs inherit the advantages of interferometer such as high sensitivity, ease of fabrication and location insensitivity.

1.3 Configuration of optical fiber sensors

Fiber sensors can also be generally classified into three different configurations: single point sensor, qausi-distributed sensor and fully-distributed sensor. For a single point sensor, the sensing element is at the head of a fiber, and the signal is collected and guided by the fiber. Qausi-distributed sensor has multiplexing sensing points along a single fiber and these sensing points can be identical and share the same interrogation and demodulation system. Fully-distributed sensor has continuous sensing element, most sensors of this kind are based on the intrinsic properties of fiber, like Raman scattering and Brillion scatter; thus no particular structure is made on the fiber.

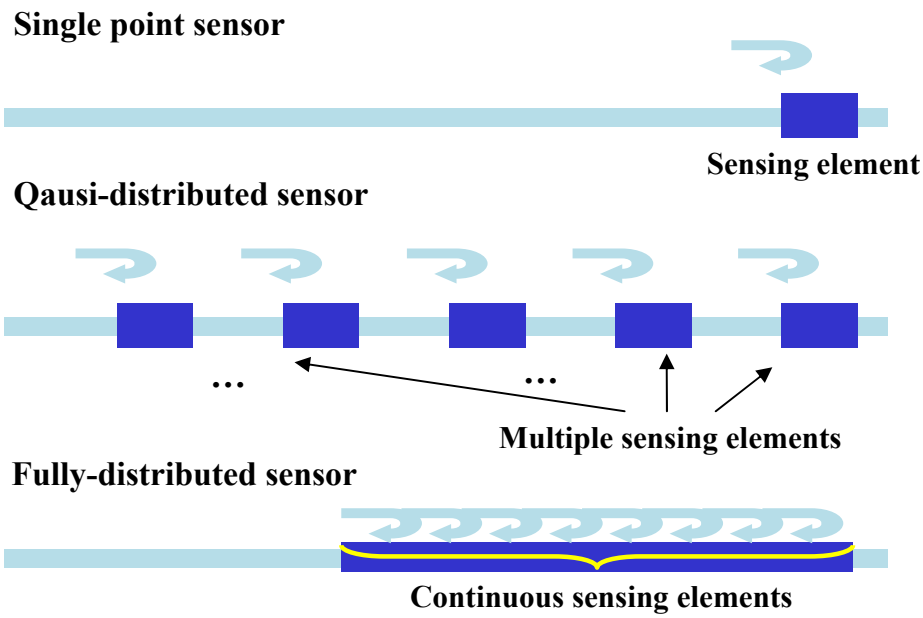

Figure 1.7 Optical fiber sensor configuration

1.3.1 Single point fiber optic sensor

Single point sensors are used in applications where the parameter of interest is at a location, or when it is not possible to use multiple spots due to installation restrictions. For example, biosensors for clinical application require the sensors suitable for small sample volume and invasive diagnosis. Some conventional sensors are also based on a single point measurement like thermometers, strain gauges and pressure meters. However, fiber optic sensors of this kind are more attractive due to some intrinsic advantages such as small size, harsh environment endurance, and electromagnetic interference immunity. These make them a superior choice for some applications such as down-hole oil well temperature and pressure monitoring, in highly electromagnetic interfered environments and chemical constituents in the blood of patients undergoing surgical treatment [24-26]. For single point sensors, the end of a fiber usually works as a probe and light signal is collected and guided by the fiber. For different applications, a transducer attached on the probe interacts with a parameter of interest, and the interaction generates a measurable optical signal. An example is the optical fiber attached with an antibody that reacts specifically with the carcinogen benzopyrene(BaP) for the detection of the cancer-causing agents in groundwater [27]. The binding between the antibody and the BaP will produce fluorescence, which can be guided by the optical fiber and measured. However,

to obtain distributed information of a measurand, installing a number of single point sensors at different locations is often too expensive and not applicable. To fulfill this requirement, a significant effort has been taken to investigate distributed fiber optic sensors.

1.3.2 Fully distributed fiber optic sensor

Distributed sensing is a technique which is unique to fiber-optic technologies. Few electrical cables can be configured to be read through a time-domain reflectometer, none has the ruggedness, flexibility and accuracy of fiber-optic models [28]. Distributed fiber optic sensors are classified into two catalogues: fully-distributed sensors and quasi-distributed sensors. Fully-distributed sensor has continuous sensing points along a single fiber and sensing mechanisms are mostly based on the intrinsic properties of fibers like Rayleigh scattering, Raman scattering and Brillion scattering. Quasi-distributed sensor has a great number of multiplexed sensors along a fiber and only at the points where the sensors are made information can be obtained.

Fully-distributed sensors are based on optical time domain reflectometry (OTDR) or optical frequency domain frequency reflectometry (OFDR), and they are used for monitoring of distributed temperature, strain or pressure [29-31]. OTDR has been the starting points of distributed sensing techniques. In this scheme, an optical pulse is launched into a fiber and the backscattered pulse along the fiber is detected by a photodetector. The detected pulse signal is modulated by the environment condition along the fiber. The time information is converted to distance information provided that the speed of light is known. OFDR is another commonly-used detection scheme in which the probe light is a continuous wave (CW) frequency modulated light. The light is further split into a reference arm and a measurement arm of an interferometer. The reflected light from the measurement arm will beat with the reflection light from the reference arm. The position information can be retrieved from the beat signal. The reflectivity as a function of length is obtained by the Fourier transform. The advantages of the OFDR technique are the high spatial resolution (millimeter-level over 2km of optical fiber) and the achievable sensitivity (-130dB) [32]. According to the types of the intrinsic scatted light, fully distributed can be classified into three main kinds: Rayleigh scattering, Raman

scattering and Brillouin scattering. Figure 1.8 schematically shows the spectrum of the scattered light from a single wavelength λ_0 in the wavelength domain.

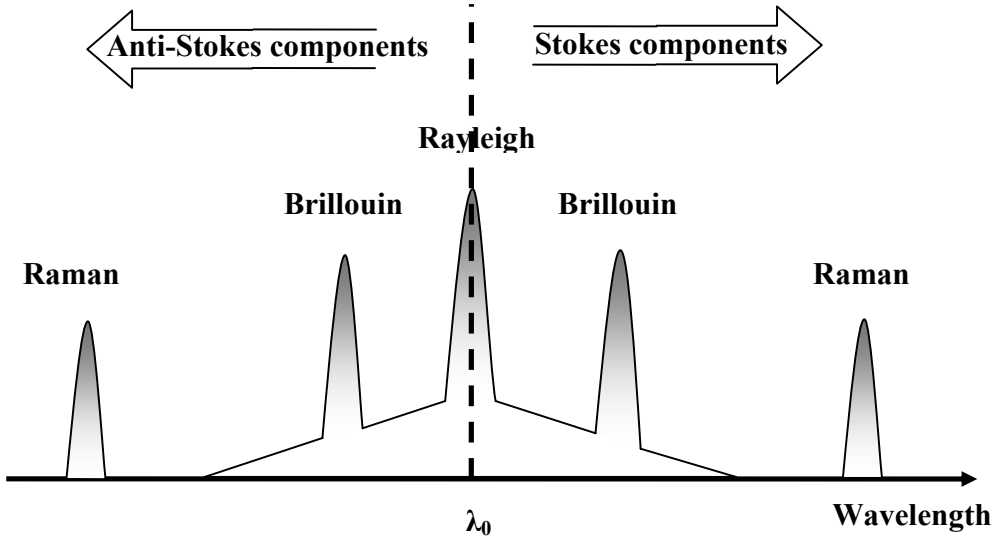

Figure 1.8 Spectrum of backscattered light of optical fiber

Rayleigh scattering

Rayleigh scattering is a type of linear scattering, which is characterized by having no change in frequency in the scatted light. Rayleigh scattering is caused by the elastic collision between the light wave and small particles, which are much smaller than the wavelength of light. Rayleigh scattering accounts for the major attenuation of optical fiber. When coherent light enters an optical fiber, some scattered light is reflected back toward the light source. This light is called back-scatted light. For distributed sensing applications, the intensity or the polarization state of the back-scattered light is changed by environment conditions such as temperature and strain. Hartog and Payne demonstrated distributed temperature measurement using the Rayleigh scattering coefficient of liquid-core and silica fiber [33]. Froggatt et al. introduced an OFDR system to measure distributed strain based on back-scattered Rayleigh scattering [34]. Rogers proposed polarization optical time domain reflectometry (POTDR) based on the detection of the polarization state of backward Rayleigh scattering [35]. Since the distributed sensing based on Rayleigh scattering depends on the intensity or polarization

measurement, the fluctuation of the light source, the fiber bending loss and optical components in the system limit the measurement accuracy and their applications.

Raman scattering

Raman scattering is a type of nonlinear scattering, which is accompanied by a frequency shift of the scatted light. The Raman scattering is caused by thermally-induced molecular vibration of glass fiber. The frequency shift equals the characteristic vibration frequencies of the molecules. Photons scattered to higher frequencies are termed anti-Stokes components and those scattered to lower frequencies are termed Stokes components. For Raman scattering, the amplitude of the anti-Stokes components is strongly temperature dependent whereas the amplitude of the Stokes components is not. Consequently by calculating the ratio between the anti-Stokes amplitude and the Stokes amplitude, the local temperature information at the point where the scattering occurs can be monitored. By using OTDR methods, the spatial distribution of the temperature can be derived. The major difficulty of Raman-OTDR is the low Raman scattering coefficients, which are about three orders of magnitude weaker than that of the Rayleigh. Therefore, integration of the scattering signal over a relatively long fiber segment (~one meter) and a long average time (~one minute) is necessary to obtain accuracy of 1°C. The spatial resolution is also partially limited by the laser pulse width.

Brillouin scattering

Brillouin scattering is another type of nonlinear scattering. Brillouin scattering is caused by the thermally excited acoustic vibration when a light is propagating in an optical fiber. The acoustic vibration introduces an energy transformation from forward-moving input light to a counter-propagating wave, which is called a Brillouin scattering wave. There is a frequency shift between the original light frequency and the Brillouin scattering wave, which is determined by the frequency of the acoustic wave, typically in the order of tens of GHz. The acoustic vibration is directly related to the medium density, which is temperature and strain dependent. Thus, Brillouin scattering can be used for temperature or strain measurement. Brillouin scattering can occur spontaneously at low input optical power. Above a certain threshold power, stimulated Brillouin scattering can happen,

which leads to a much greater intensity of the scattering mechanism and consequently an improved signal-to-noise ratio. Compared with Raman-based techniques, which detect the intensity changes, Brillouin-based techniques are frequency-based detection and inherently more accurate and stable in the long term, because intensity-based techniques often suffer from a higher sensitivity to drifts [36]. In the past two decades, the performance of distributed sensors based on Brillouin scattering has been improved significantly. The longest reported sensing length is 150km with 2m spatial resolution and 1°C temperature resolution. Simultaneous temperature and strain sensing has also been realized in photonics crystal fiber (PCF) and polarization maintaining fiber (PMF) at centimeter spatial resolution [37].

1.3.3 Quasi-distributed fiber optic sensor

In a quasi-distributed fiber optic sensor, a finite number of sensor elements are fabricated a long a single fiber and share the same interrogation system to reduce the cost of each sensing point. Only at the points where sensors are made, a measurand can be monitored. Both quasi-distributed sensors and fully-distributed sensors are attractive for their applications in health monitoring of large scale structures like bridges, dams and aircraft engines. The fully-distributed sensors use standard telecommunication fibers, so no extra structures need to be made on the fiber. Compared with fully distributed sensors, quasi-distributed sensors have more flexibility in the sensor design, which enable the sensor to detect more parameters than the fully-distributed sensors, like pressure, PH values and refractive indices [38-40]. Another common limitation of fully-distributed sensors is the weak scattering signal and consequently poor signal-to-noise ratio, which requires long average time or an expensive high-power light source to compensate. Quasi-distributed fiber optic sensors may be based on a variety of principles such as Fresnel reflection, Fabry-Perot interferometers, and fiber Bragg gratings (FBG) [41-43]. Among different kinds of sensors, fiber Bragg gratings are the most attractive due to the unique features including high sensitivity, a large multiplexing capability and low-lost. To multiplex a large number of sensors along a single link, different kinds of multiplexing techniques have been investigated for a wide variety of applications.

1.4 Summary and scope of research

Several techniques for distributed measurement by optical fibers have emerged from the laboratory and been transitioned to commercial products, including Raman optical time-domain reflectometry (ROTDR), Brillouin optical time-domain analyser (BOTDA), OFDR and many kinds of multiplexed FBG sensors [44-46]. However, the signal-to-noise ratio of the Raman-based system is limited by the extremely weak intensity of the reflected anti-Stokes lines. Therefore, integration of the scattering signal over a relatively long fiber segment and long time is necessary to obtain a favorable accuracy. ROTDR and BOTDA are primarily for temperature measurement. Significant efforts were made to measure other quantities, such as strain and pressure, but since the fiber is much more sensitive to temperature than to these quantities, limited success has been reported. BOTDA has been reported for distributed strain measurement, but the sensitivity coefficient is low compared with temperature measurement [37]. To date, the most successful method for distributed temperature, strain and pressure measurements are based on the use of fiber Bragg grating sensors. FBGs have been shown to be useful in measurement of temperature, strain and pressure [47-49]. In general, their sensitivity to pressure is much lower than to temperature and strain so the use of a mechanical amplifier is often necessary.

Several FBG multiplexing techniques have been developed to reduce the system size and unit cost. To the author's best knowledge, the current maximum multiplexing number is 800 identical FBG sensors in a single array using optical frequency domain reflectometry (OFDR) [10]. Although this method is capable of multiplexing a large number of weak FBGs in one fiber, it suffers from several severe limitations. The first is the polarization fading due to the unpredictable changes in the polarization orientations of the light beams returned from the two fiber arms. The second is the limited operating distance because the maximum fiber length is limited by the coherence length of the tunable laser, which is currently limited to only a few hundred meters.

The discussions above clearly show that there is no technology currently available that allows dense multiplexing of strain or pressure sensors with long distance operating capability. Further the current distributed temperature sensors have rather limited spatial

resolution and accuracy. This situation suggests that a new technology that can support many sensors of different types along a single fiber be developed to meet a wide range of application needs relating to key industrial facilities with strong national interest.

In this work, a wavelength-scanning time division multiplexing (WSTDM) network based on identical ultra-weak FBGs was proposed and has been demonstrated with experimental results. This dissertation has been organized as following chapters:

Chapter 1 introduces the classifications of optical fiber sensors, briefly reviews the distributed fiber optic sensors and discusses the advantages of fiber optic sensors for structure health monitoring applications.

Chapter 2 discusses the theory of fiber Bragg gratings and describes the design of a wavelength scanning time-division multiplexed (WSTDM) sensor network based on ultra-weak fiber Bragg gratings, including investigating the multiplexing capability of ultra-weak FBGs and simulating the spectra of serially multiplexed FBG sensors

Chapter 3 presents the construction of an automated FBG fabrication system, which was further used to write 1000 FBGs. With this system, it takes 48 seconds to fabricate one FBG, and up to 500 FBGs can be made continuously.

Chapter 4 introduces the interrogation system of the WSTDM and a spectrum reconstruction algorithm. We analyzed the performance of a 1000-FBG sensor link and discussed the experimental results for distributed temperature measurement.

Chapter 5 summarizes the contribution of this work and discusses the improvement of future research

Chapter2 Wavelength-scanning time division multiplexed fiber Bragg grating sensor network

2.1 Introduction to fiber Bragg gratings

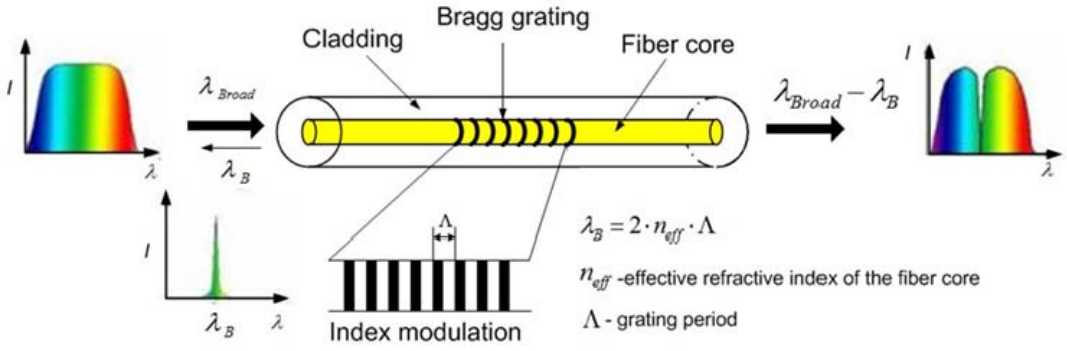

Figure 2.1 Illustration of FBG principle

Since Hill et al. discovered photosensitivity in optical fiber in 1978, rapid progress has been made in many aspects of fiber Bragg gratings (FBGs) including sensing principles, properties, interrogation, fabrication and multiplexing of FBG sensors. When germanium doped fiber is exposed to ultraviolet (UV) light, its refractive index will increase as irradiation time and power. FBG is a structure formed by periodically changing the refractive index of a fiber core as shown in figure 2.1. When a broadband light is launched into a fiber, only the light at a specific wavelength will be reflected, which is defined as Bragg wavelength λ_B and it can be described by this simple model:

$$\lambda_B = 2 \times n_{eff} \times \Lambda \tag{2.1}$$

where Λ is the period of the pattern and n_{eff} is the effective refractive index. Both these two parameters Λ and n_{eff} can be modulated by the environment condition. Thus by monitoring the change of the Bragg wavelength, measurement of a parameter can be realized, such as strain, temperature and pressure. FBG sensors have been successfully embedded into composite materials as a temperature or strain sensor for structural health monitoring in industry [31, 47, 49]. Advantages of FBG sensors include: absolute

measurement without reference, intrinsic wavelength-encoded operation which eliminates the error induced by light power fluctuations, and distributed sensing capability. Among these advantages, multiplexing capability for distributed measurement is the most notable one.

2.2 Modeling of fiber Bragg gratings

The properties of FBGs such as the bandwidth, Bragg wavelength and dispersive coefficient can be specifically designed. Therefore, FBGs have been used for different applications, including dispersion compensation, filters for WDM networks and distributed sensors in structural health monitoring. In order to design fiber gratings for various applications, several models are developed to investigate the characteristics of fiber gratings, including the coupled-mode theory, the transfer matrix method and the [50-53]. The most-commonly used mathematical model is the coupled-mode theory, which is straightforward and accurately models the optical properties of most fiber Bragg gratings of interest [54]. In this section, we will briefly introduce the coupled-mode theory. The detailed analysis can be found in [51, 53, 54].

A grating is regarded as a perturbation to the fiber. For a uniform grating, the effective refractive index n_{eff} of the fiber core approximates as

$$n_{eff} = n_1 + \overline{\Delta n} + \frac{\Delta n}{2}\cos\left(\frac{2\pi}{\Lambda} + \Phi(z)\right), \quad 0 < z < L \tag{2.2}$$

$$n_{eff} = n_1, \quad z\ otherwise$$

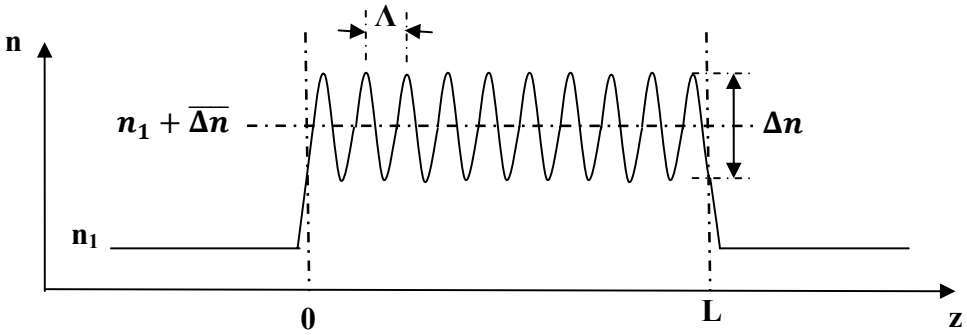

Figure 2.2 Diagram of refractive index change along the fiber

where n_1 is the unperturbed refractive index of the fiber core, $\overline{\Delta n}$ is the average (DC)

index change in the grating region, $\frac{\Delta n}{2}$ is the amplitude (AC) of index modulation, Λ is the modulation period, $\Phi(z)$ is the initial phase of the modulation. The index modulation profile is given in figure 2.2.

Assuming that the fiber is lossless and single mode in the wavelength range of interest, only one forward mode and one backward mode are considered. In other words, the total electric field is a superposition of forward and backward propagating modes:

$$\vec{E}(x,y,z,t) = [A(z)\exp(i\beta z) + B(z)\exp(-i\beta z)]\overrightarrow{e_t}(x,y)\exp(-iwt) \qquad (2.3)$$

where A(z) and B(z) are the slowly varying amplitudes of the mode traveling in +z and –z direction, β is mode propagation constant $\beta = \frac{2\pi}{\lambda} n_{eff}$, and *w* is the angular frequency of the light. A grating structure introduces a coupling between the forward-propagating and the backward-propagating modes. If we choose the appropriate synchronous terms, the coupling is dominated by the following simple coupled-mode equations [53, 55]:

$$\frac{\partial A}{\partial z} = i\kappa_{dc}A + i\kappa_{ac}Bexp(-i(\Delta\beta z - \Phi[z])) \qquad (2.4)$$

$$\frac{\partial B}{\partial z} = -i\kappa_{dc}B - i\kappa_{ac}^{*}Aexp(i(\Delta\beta - \Phi[z])) \qquad (2.5)$$

where $\Delta\beta = 2\beta - \frac{2\pi}{\Lambda}$ is a phase mismatch term and referred as a detuning, κ_{dc} is the DC coupling constant, κ_{ac} is the AC coupling constant:

$$\kappa_{dc} = \frac{n_1 w\varepsilon_0}{2}\iint_{core}\overline{\Delta n}|\overrightarrow{e_t}(x,y)|^2\,dxdy \qquad (2.6)$$

$$\kappa_{ac} = \frac{n_1 w\varepsilon_0}{4}\iint_{core}\frac{\Delta n}{2}|\overrightarrow{e_t}(x,y)|^2 dxdy \qquad (2.7)$$

where ε_0 is the permittivity of vacuum. To find a solution, the following substitutions are made for the forward (R) and backward propagating(S) modes [53, 55]:

$$R = Aexp[\tfrac{i}{2}(\Delta\beta z - \Phi(z))] \qquad (2.8)$$

$$S = Bexp[\tfrac{-i}{2}(\Delta\beta z - \Phi(z))] \qquad (2.9)$$

Substituting Eq. (2.8) (2.9) into Eqs. (2.4) and (2.5), the following coupled-mode equations are obtained:

$$\frac{dR}{dz} - i\left[\kappa_{dc} + \frac{1}{2}\left(\Delta\beta - \frac{d\Phi(z)}{dz}\right)\right]R = i\kappa_{ac}S \tag{2.10}$$

$$\frac{dS}{dz} + i\left[\kappa_{dc} + \frac{1}{2}\left(\Delta\beta - \frac{d\Phi(z)}{dz}\right)\right]S = -i\kappa_{ac}^{*}R \tag{2.11}$$

For uniform gratings, the coupling coefficient is constant over the grating length L and thus z-independent. In this situation, the coupled mode equations are coupled first-order differential equations with constant coefficients, for which analytical solutions can be solved by specifying appropriate boundary conditions [55]. We assume that the amplitude of forward-going wave at z=0 is R(0)=1 and the amplitude of backward-going wave at z=L is S(L)=0. With these initial boundary conditions, the following reflection coefficient and transmission coefficient are obtained:

$$r = \frac{S(0)}{R(0)} = \frac{-\kappa_{ac}\sinh(\alpha L)}{\delta\sinh(\alpha L) + i\alpha\cosh(\alpha L)} \tag{2.12}$$

$$t = \frac{R(L)}{S(0)} = \frac{i\alpha}{\delta\sinh(\alpha L) + i\alpha\cosh(\alpha L)} \tag{2.13}$$

where $$\delta = \kappa_{dc} + \frac{1}{2}\left(\Delta\beta - \frac{d\Phi(z)}{dz}\right) \tag{2.14}$$

and $$\alpha = \sqrt{|\kappa_{ac}|^2 - \delta^2} \tag{2.15}$$

The power reflection coefficient is

$$|r|^2 = \frac{|\kappa_{ac}|^2 sinh^2(\alpha L)}{|\kappa_{ac}|^2 cosh^2(\alpha L) - \delta^2} \tag{2.16}$$

For single mode fiber, DC and AC coupling coefficients are approximated with $\kappa_{ac} \cong \frac{\pi}{\lambda}\frac{\Delta n}{2}$, $\kappa_{dc} \cong \frac{2\pi}{\lambda}\overline{\Delta n}$ [53, 55], for uniform FBGs $\frac{d\Phi(z)}{z} = 0$. Substituting these terms in Eqs (2.14-2.16), the reflection spectra of the uniform FBGs with different parameters can be simulated. Figure 2.3 shows the spectra of the FBGs with different grating lengths *L*. In this simulation, Λ =535.2nm, $\overline{\Delta n} = 1 \times 10^{-4}$, and $\Delta n_1 = 0.5 \times 10^{-4}$. The simulation

spectra show that a longer grating length results in a stronger reflectivity and a narrower bandwidth.

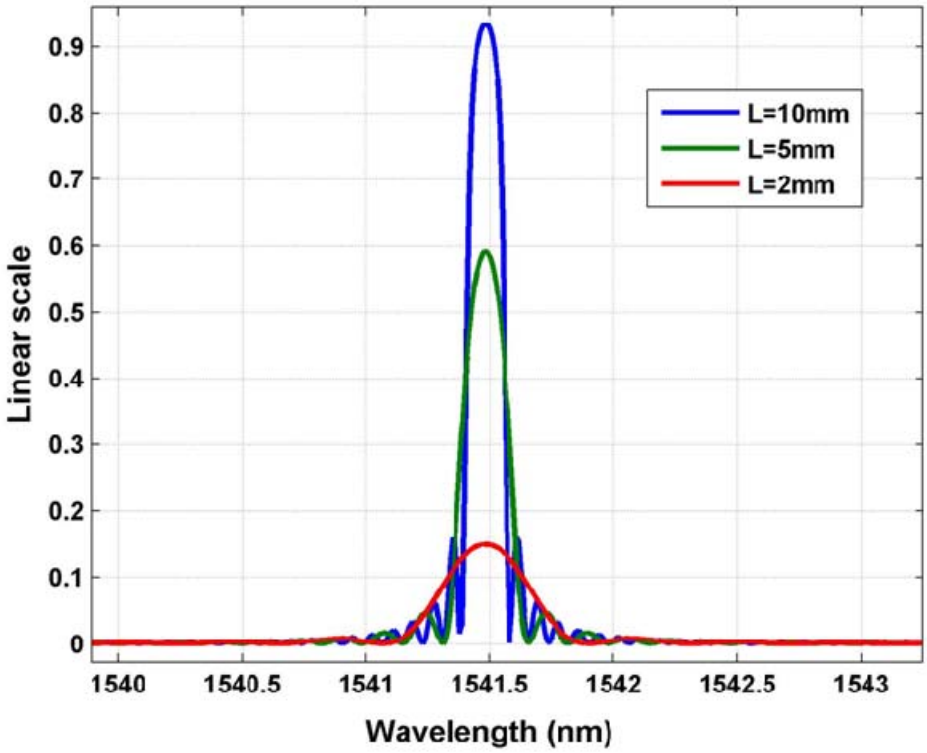

Figure2.3Simulated reflection spectra of the FBGs with different grating length L

For non-uniform gratings, the couple mode equations must be solved by numerical methods and a variety of numerical methods have been investigated to calculate the reflectivity, transmission and dispersion of various types of FBGs, such as apodization FBG, chirped FBG and tilted fiber gratings [55]. These modeling methods provide the theoretical analysis for the FBG structure design, several and other parameters, such as the grating length and effective index modulation profile, and arbitrary apodization profiles can be adjusted for variable practical applications.

2.3 Multiplexing techniques of FBG sensor network

FBGs have been employed as an attractive sensing element for various measurands such as temperature, strain and pressure. A distinctive advantage of FBGs is their multiplexing

capability. In applications where dense sensing points are desired, a large number of sensing FBGs are distributed to a sensing region. To reduce the unit sensor cost, FBG sensors have been multiplexed by various methods. To date, several FBG multiplexing techniques have been developed including time division multiplexing (TDM), wavelength division multiplexing (WDM), frequency division multiplexing (FDM) and other multiplexing methods.

2.3.1 Time division multiplexing

TDM is a commonly used method and various TDM systems have been developed in the past [56]. In this method, a pulsed light is launched into a sensor network and reflected pulses from FBG sensors with different time delays are used to identify the sensors in the link. FBGs used in this method can have identical resonant wavelength. Figure 2.4 shows a TDM system: a CW light from a laser diode is modulated into a pulse and launched into a sensor link by a circulator. A photodector is used to detect the time delays of the reflected light from the sensors. The shifts of the resonant wavelengths of the FBG sensors are detected to measure the parameters of interest.

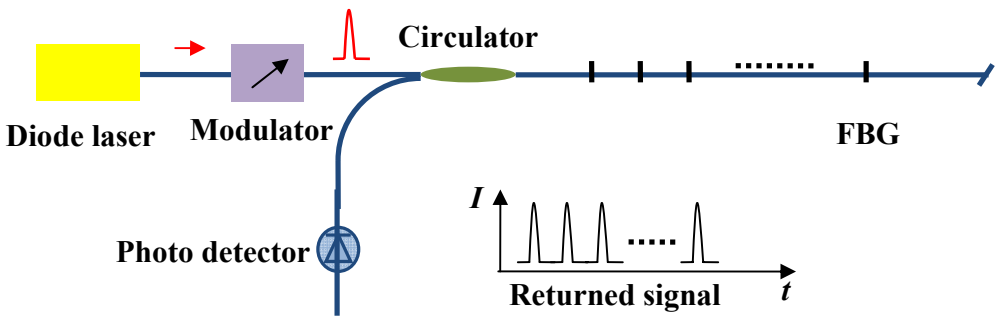

Figure 2.4 Configuration of a TDM FBG sensor network

According to the topology of the sensor link, the TDM technique can be classified into parallel TDM networks and serial TDM networks. Since a parallel TDM network employs couplers or beam splitters to separate the FBGs into different optical channels, it suffers from the complicated structure and the high power splitting loss. The multiplexing capability of the traditional serial TDM network based on normal FBGs (reflectivity=20dB) is limited by the intrinsic crosstalk [57]. Based on this TDM method, around 100 FBGs along a fiber can be interrogated.

2.3.2 Wavelength division multiplexing

WDM is another attractive multiplexing method as it uses optical power efficiently. In a WDM system, a broadband light is used to interrogate the FBG sensors along a single fiber line. A number of FBG sensors are serially connected, and the sensors are designed to reflect at different resonant wavelengths. A dispersive element, such as a grating or prism, is used to separate the returned signals from the sensors into separate detectors. For each FBG, the wavelength shift is monitored to determine the change of a measurand. A WDM system is illustrated in figure 2.5. For the WDM method, the maximum number of sensors is limited by the ratio of the system bandwidth, usually less than 100 nm, over the dynamic wavelength range of an individual FBG sensor, typically a few nanometers. Thus, this method is often limited to tens of FBGs.

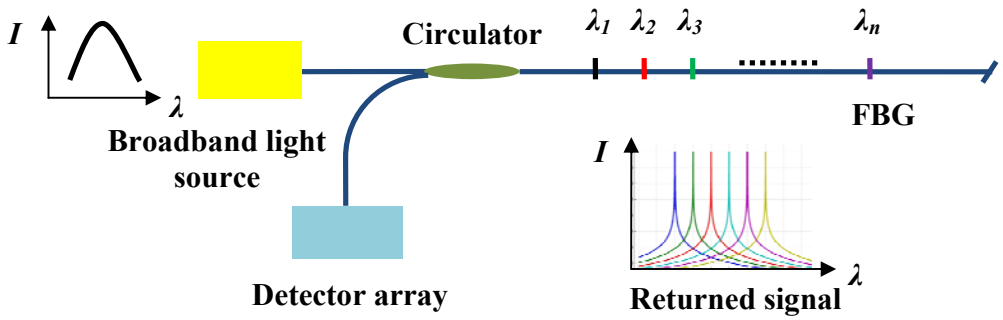

Figure 2.5 Schematic of a WDM FBG sensor network

2.3.3 Frequency division multiplexing

For the FDM technique, the laser source is frequency modulated by an external modulator or directly modulated by a driving current. The returned signal from the sensors will have different frequencies due to the modulation of the light source. The returned signal will beat with a reference signal and result in a frequency difference, which is used to retrieve the sensor information, like the positions or optical path unbalance of the sensors. One of the best FDM methods is called optical frequency domain reflectometry (OFDR). A basic schematic for the OFDR is given in figure 2.6. In the OFDR technique, a continuously tunable laser is used as a light source. The reflected signal from the FBG sensors along a fiber interfere with the returned signal

from a reference arm. The beating signal is detected to obtain the information of each sensor. One advantage of the OFDR is that the multiplexed gratings can have overlapping spectra.

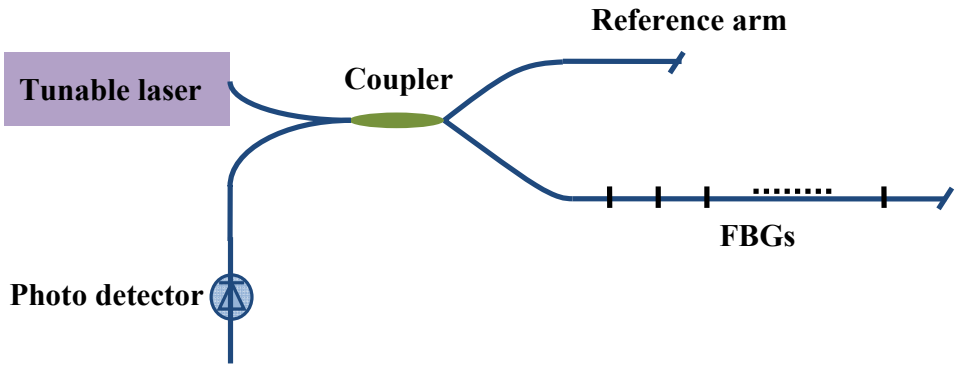

Figure 2.6 Illustration of an OFDR system

To the author's best knowledge, the current maximum multiplexing number is 800 identical FBG sensors in a single array using OFDR [9]. Although this method in principle is capable of multiplexing even more weak FBGs in one fiber, it is limited in its maximum sensing span by the coherence length of the tunable laser source, and also suffers from polarization fading.

2.3.4 Other multiplexing schemes.

There are some least-commonly used multiplexing techniques, including polarization division multiplexing (PDM), coherent division multiplexing (CDM) and spatial division multiplexing (SDM) [58-60]. The PDM scheme launches the light with different polarization states into different channels and extracts each state. There is a recent interest in using polarization maintaining fiber in combination with time domain techniques to form polarization-based distributed sensors [37, 61]. In a CDM system, the light source has coherent lengths that are shorter than the length difference between the reference and signal channels in a Mach-Zehnder interferometer configuration. The signal is extracted by putting a rebalancing interferometer in front of each detector. The CDM is not used as commonly as the TDM, WDM and FDM because of the optical power budgets and additional complexities in the configuration. The SDM scheme splits the light into different fiber links, and the sensors are distinguished by their locations.

The advantages of the SDM method include the balanced power budget for each sensor link and free crosstalk between sensors. Other combination multiplexing techniques usually with better performance but more complexity have been investigated. A combination of WDM and SDM has been reported to support over 100 FBGs [62]. Dense WDM of FBG sensors using code division multiple access (CDMA) was reported to give a better signal-to-noise ratio by averaging the sensor output power[63].

2.4 Wavelength-scanning time division multiplexing scheme

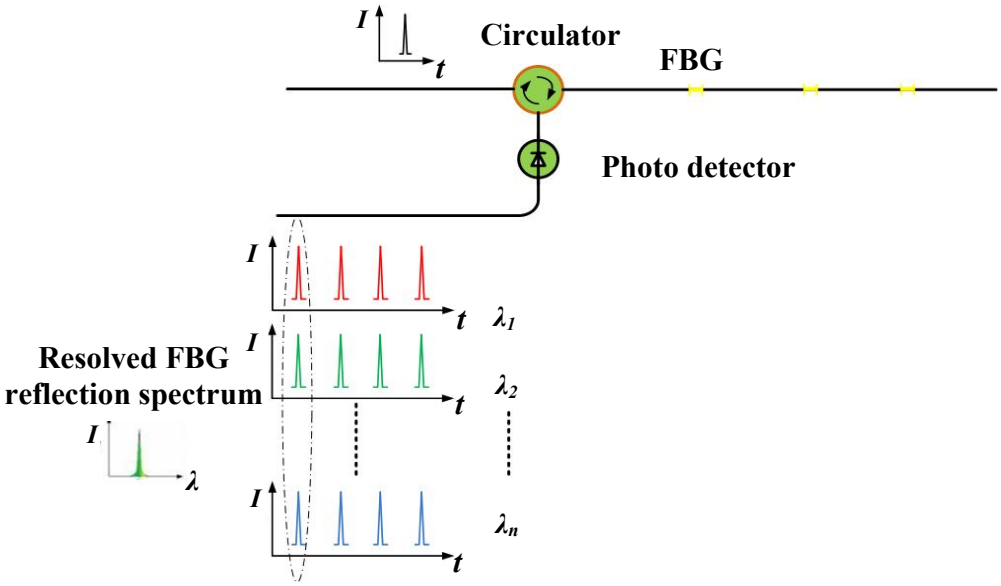

Figure 2.7 Schematic of WSTDM network

In this work, a wavelength-scanning time division multiplexing (WSTDM) network based on identical ultra-weak FBGs is proposed and experimentally demonstrated. The schematic is illustrated in figure 2.7. Assume N identical FBGs are serially connected in a single fiber with the same space separation d. At a single wavelength, a single light pulse is launched into the sensor array and successive reflected pulses return. The delay time between two neighboring sensors is

$$t = \frac{2nd}{c} \tag{2.17}$$

where n is the refractive index of fiber, and c is the speed of light in vacuum. The input pulse width is selected to be less than the time delay between two adjacent sensors to

eliminate the signal overlap in time, and thus different FBGs can be identified by different time delays. If we scan the source wavelength, the reflection spectrum of each sensor in the link can be resolved base on the intensities of the returned pulses at the corresponding time.

Compared with the previous methods, the WSTDM has several advantages: The tiny crosstalk between the ultra-weak FBGs allows over one thousand FBGs multiplexed in series; The TDM structure enables the simultaneous measurement of all the sensors; The identity of the FBGs simplifies the sensing link and makes the mass production of the sensing array possible. In addition, in contrast with the OFDR, this method is not limited in its sensing span by the source coherence and further eliminates the polarization fading problem.

The multiplexing capability of a serial TDM FBG network is mainly affected by two factors: the insertion loss of the upstream FBGs and the crosstalk between the FBGs. If we assume all the FBGs are identical, these two factors are related to the peak reflectivity of each FBG. To understand the relationship between the multiplexing capability and the peak reflectivity, theoretical analysis and simulation aiming to maximize the FBG multiplexing number in a single fiber are conducted.

2.4.1 Multiplexing capacity

The maximum multiplexing number of FBGs is mainly limited by the total power of a system and the insertion loss of each sensor. Usually the total power of a system is fixed; thus a lower insertion loss of each FBG is preferred, which corresponds to the lower reflectivity of each FBG. Assuming N identical FBGs are serially written on a fiber, and their reflectivities are small enough that the multiple reflections among the gratings can be neglected, the returned power from the i^{th} (i=1, 2, … N) FBG at wavelength λ can be approximated as [64, 65]:

$$I_{ri}(\lambda) = (1 - R(\lambda))^{2(i-1)} R(\lambda) I_0(\lambda) \tag{2.18}$$

where $I_0(\lambda)$ is the source power and $R(\lambda)$ is the spectral reflectivity of each FBG. When $R(\lambda)$ changes from -20dB to -40dB, the simulated returned power of each FBG in a 1000-FBG array is shown in figure 2.8. If $R(\lambda)$ is relatively high, the returned signal from

the i^{th} FBG decreases dramatically with i, which limits the multiplexing number to a few tens only. But when $R(\lambda)$ is less than -30dB, the difference between the returned signals from all the 1000 FBGs is less than 10 dB.

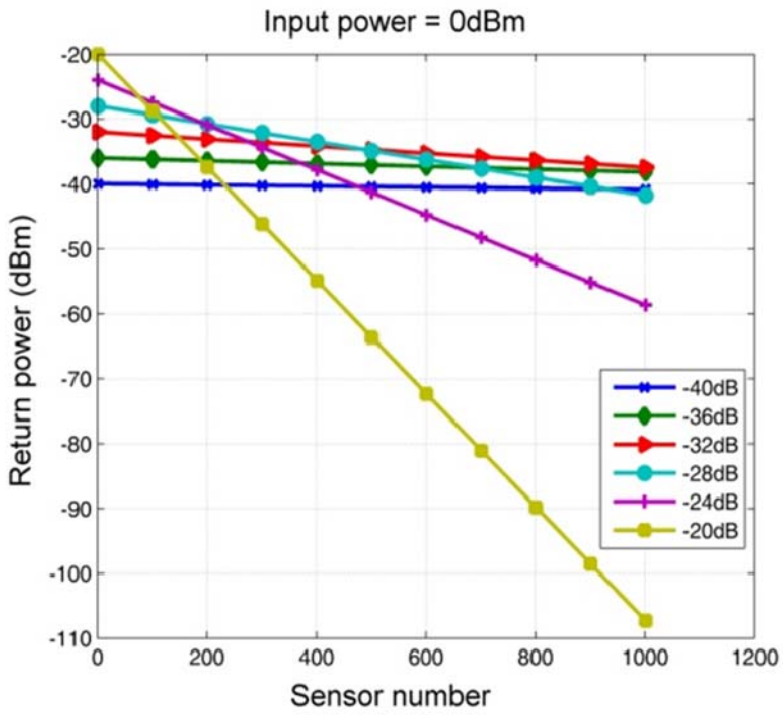

Figure 2.8 Returning power of a 1000-sensor array with different reflectivities

2.4.2 Crosstalk analysis

The multiplexing capacity of the serial TDM sensor network is also limited by two kinds of crosstalk: spectral shadowing and multiple-reflection crosstalk. Spectral shadowing describes the spectrum distortion of the downstream FBGs caused by the insertion loss of the upstream FBGs. Multiple-reflection crosstalk refers to the spectrum distortion induced by the false signal, which undergoes multiple reflections between the upstream FBGs and arrives at the detector at the same time with the real signal of the downstream FBGs. In this section, the crosstalk of the ultra-weak FBGs will be investigated from these two aspects.

Spectral shadowing

The typical reflection spectrum $R(\lambda)$ of an FBG approximates a Gaussian function of wavelength, which indicates that the transmission loss is wavelength-dependent. The FBGs at the far end of the sensor network will suffer the spectrum distortion caused by this accumulated wavelength-dependent insertion loss. If we approximate the spectral reflectivity $R(\lambda)$ of an FBG as [66, 67]:

$$R(\lambda) = R_g \exp(-4\ln 2\left(\frac{\lambda - \lambda_B}{B_g}\right)^2) \tag{2.19}$$

where R_g, λ_B and B_g are the peak reflectivity, Bragg wavelength, and bandwidth of the FBG respectively. Substitute equation 2.19 into equation 2.18, the reflection spectrum of the i^{th} FBG in the N identical sensor network can be simulated, and the results are shown in figure 2.9. In figure 2.9(a), the high peak reflectivity of each FBG (-20dB) makes the reflection spectra of the first sensor and the 50th sensor quite different: the spectrum of the 50th sensor is broadened and the returned power is 4 dB lower. In figure 2.9(b), the reflectivity of each FBG is lower (-40dB); and there is no much difference even between the reflection spectra of the first FBG and the 500th FBG.

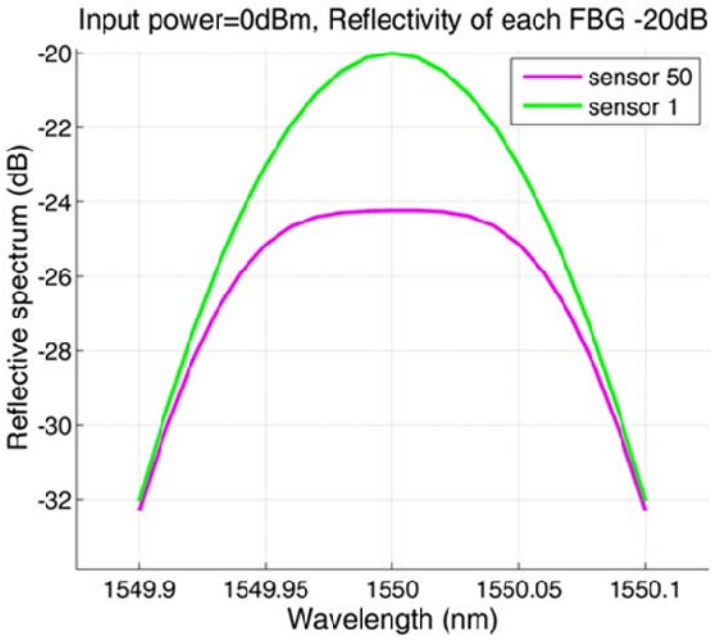

(a)

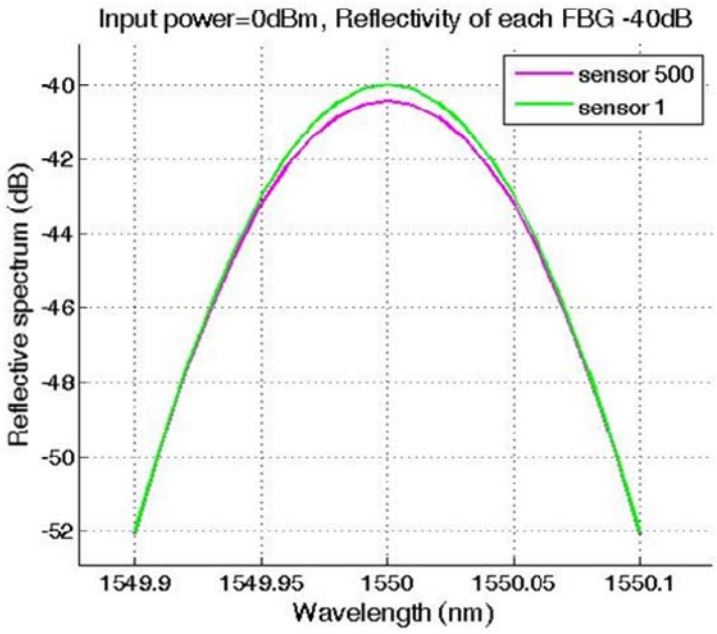

(b)

Figure 2.9 Spectral shading of the FBGs with different peak reflectivity Rg

Multiple-reflection crosstalk

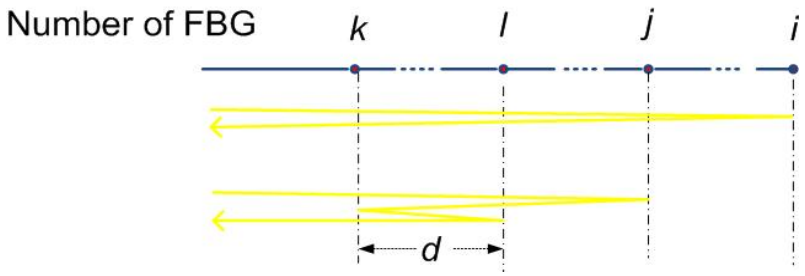

Figure 2.10 Illustration of first order crosstalk

Multiple reflections among the FBGs may induce an inevitable crosstalk error in a serial FBG array [57, 66]. In a serial TDM system, if the separation distance between any two neighboring sensors is identical, the real signal from the i^{th} sensor returns to the detector at the same time with the false signal which undergoes multiple reflections among the upstream sensors. In this analysis, only the first order crosstalk, which undergoes 3-time reflection, is considered. Higher order crosstalk undergoes more than three times of reflection and the corresponding signals are much weaker and negligible. The illustration of the i^{th} FBG first order crosstalk is shown in figure 2.10. The real signal is reflected by the i^{th} FBG, and the false signal encounters three times of reflection at the j^{th}, k^{th} and l^{th} FBGs successively. If we assume the distance between two neighboring FBGs is d, the total travelling distance of the real signal and that of the false signal should be equal and can be described as:

$$2di = d(j + (j-k) + (l-k) + l) \qquad 1 \le k < l, j < i \tag{2.20}$$

This can be simplified as:

$$i + k = j + l \qquad 1 \le k < l, j < i \tag{2.21}$$

All the three upstream FBGs are in front of the i^{th} FBG. We assume that the k^{th} FBG is the closest one to the detector and its value can begin from 1. The reasonable ranges of j, l, and i are

$$1 \le k \le i-2 \tag{2.22}$$

$$k < l, j \le i-1 \tag{2.23}$$

Once i and k are selected, l and j pair has a fixed one-to-one relationship to meet the requirement of equation 2.21. For a given k value, l can be chosen from $k+1$ to $i-1$. Thus, the number of l and j pair is

$$(i-1)-(k+1)+1=(i-k-1) \tag{2.24}$$

For the i^{th} FBG, the number of the false signal induced by the upstream FBGs can be calculated by counting the combinations of k, l, and j pair.

$$S(i)=\sum_{k=1}^{i-2}(i-k-1)=\frac{(i-1)(i-2)}{2} \tag{2.25}$$

A special case of i=4 is used to verify the validity of equation (2.25). According to equation (2.25), the number of possible crosstalk channels should be 3. Figure 2.11 illustrates all the possible crosstalk channels for the case of i=4 and the number is 3, the same as calculated by equation (2.25). As the number of the false signal $S(i)$ increases with i, the last FBG in the sensor network suffers the crosstalk error most.

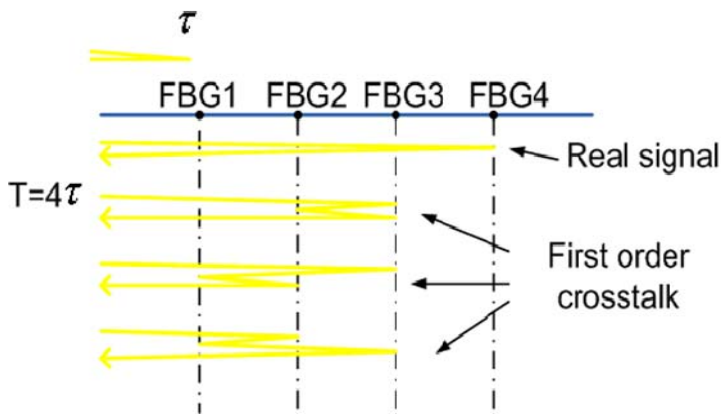

Figure 2.11 Illustration of the crosstalk of the 4th FBG

If we assume all the FBGs in the array are identical with the reflective spectrum $R(\lambda)$, the first-order crosstalk of the i^{th} FBG can be simplified as:

$$C_i(\lambda)=\frac{(i-1)(i-2)}{2}R^3(\lambda)(1-R(\lambda))^{(2i-4)}I_0(\lambda), i\geq 3 \tag{2.26}$$

where $I_0(\lambda)$ is the source power. The first-order crosstalk noise power of the FBGs with the reflectivity from -20dB to -40dB in a 1000-sensor serial array are shown in figure 2.12. For the FBGs with a relatively high reflectivity, the real signal which is reflected from the desired FBG can be buried in the first-order crosstalk. For example, in an array of -20dB FBGs, the first-order crosstalk to the 600th sensor (-60dBm) is even higher than its real returned signal (-72dBm). However, for the ultra-weak FBGs, e.g. peak reflectivity R_g=-36dB, the error signal of the furthest FBG (i=1000), which suffers the crosstalk most severely in the array, is at least -10 dB weaker than the real signal, and the induced distortion is acceptable.

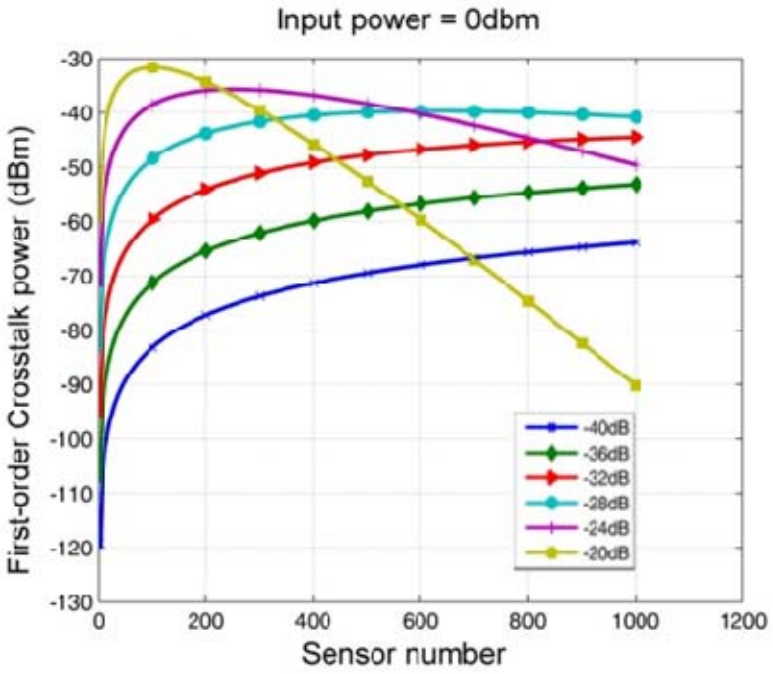

Figure 2.12 First-order crosstalk error of a 1000-sensor array with different reflectivity

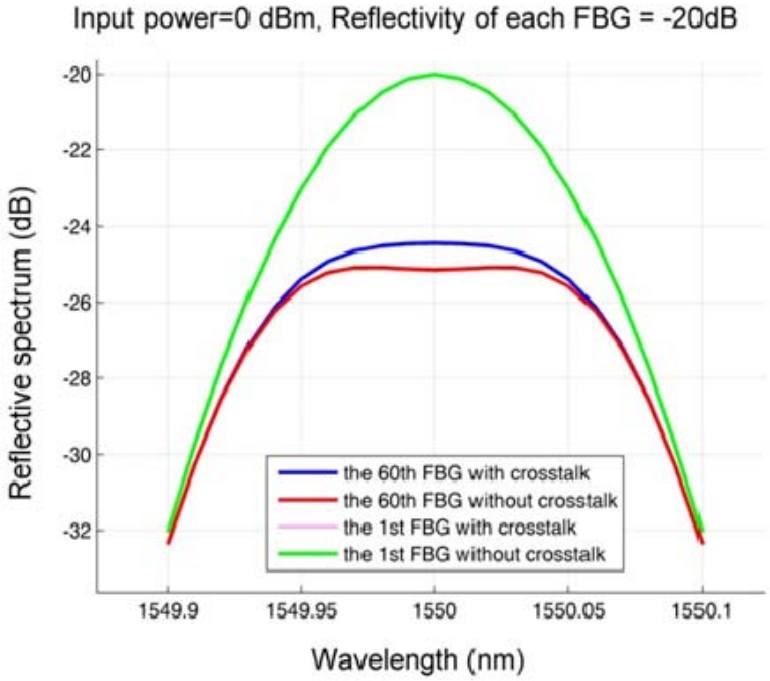

(a)

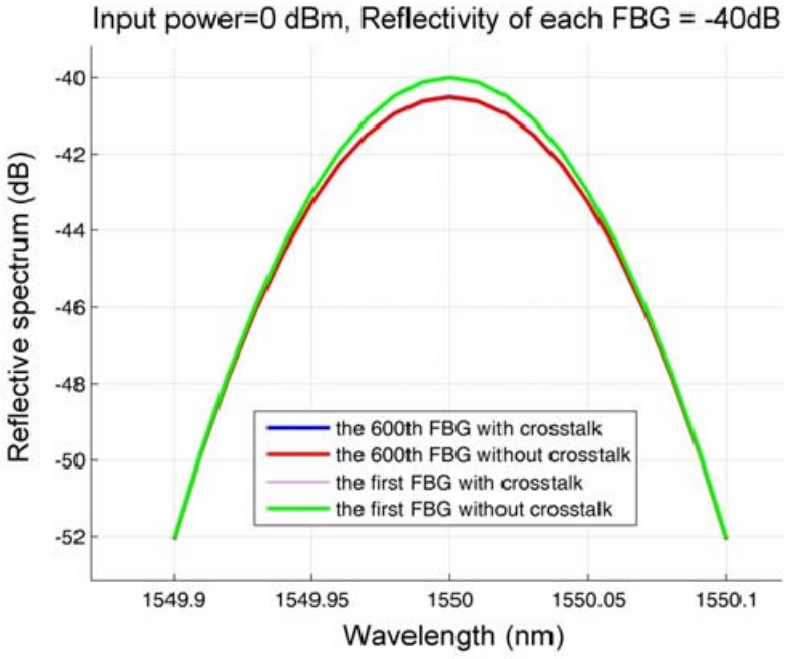

(b)

Figure 2.13 Simulation of reflective spectra of the FBGs with different peak reflectivity R_g including the crosstalk

The real returned power of the i^{th} FBG can be considered as the sum of the returned

power I_i and the crosstalk error C_i, and it can be calculated by substituting equation 2.19 into equations 2.18 and 2.26. In a large-scale sensor network, the real reflection spectra of the normal FBG (-20dB) and the ultra-weak FBG (-40dB) are simulated and shown in Figure 2.13. If the reflectivity of each FBG is relatively high (-20dB), the crosstalk error will further deteriorate the spectrum and make it impossible to use the FBG as a sensor. Whereas for the ultra-weak FBGs (-40dB), the shape of the 1st FBG and that of the 600th FBG have little difference. We tried different R_g values in the simulation, and found that if R_g is less than -35dB, the detection error of Bragg wavelength caused by the spectral distortion in a 1000-FBG network is less than 20 pm and this detection error are acceptable.

Based on the above analysis, we can easily conclude that the peak reflectivity of the identical FBGs plays an important role in determining the multiplexing capacity of the dense TDM system. If the peak reflectivity is larger than -20 dB, the insertion loss and the crosstalk among the FBGs limit the max multiplexing capacity to a few tens only. In order to multiplex over 1000 identical FBGs, the peak reflectivity of each FBG should be less than -35 dB. The further experiments and analysis are based on this ultra-weak FBG conclusion.

Chapter 3 Construction of an automated fiber Bragg grating fabrication system

The large multiplexing number of ultra-weak FBGs imposes a requirement for an efficient and repeatable FBG fabrication method. An automated FBG fabrication system was developed to meet this requirement of mass production. There are primarily two methods to fabricate a fiber Bragg grating (FBG) [68, 69]:

1. Exposure of a germanium-doped (Ge-doped) fiber to periodical ultraviolet (UV) field; the UV photosensitivity allows the refractive index along the fiber to be modulated at the same period. A fiber grating is thus produced [70]. To enhance the photosensitivity, the Ge-doped fiber is often preloaded with hydrogen [71].

2. Exposure of almost any type of fiber to femtosecond laser beam whose spatial profile is also periodical [72]. The ultra-high power of the laser pulses will modify the structure of the fiber, and periodically modulates the refractive index along the fiber, producing a fiber grating.

The FBG made with the second method is more stable, however, the introduced loss is much higher than that of the FBG made with the first method [72]. In this system, the number of FBGs may exceed one thousand, and minimizing the loss for a single FBG is essential. So the first method was selected for our FBG production.

3.1 Hydrogen loading of optical fibers

In order to decrease the cost of FBGs, Corning regular single mode fiber SMF-28, was used and its photosensitivity was dramatically enhanced by preloading the fiber with high pressure hydrogen. Since hydrogen is highly inflammable with lower flammable limit of 4% and upper flammable limit of 75% [73], and pressure up to 1800psi is required to get decent photosensitivity, a specific hydrogen loading vessel, fiber winding spool and aluminum fillings were thus designed to minimize the quantity of hydrogen used in the loading process.

For simplicity, the fiber loading bobbin and the fiber collection bobbin were designed to be the same. By considering both the size of the FBG fabrication system and bended fiber attenuation, the diameter of the spool was designed to be just less than four inches. A general purpose vessel was used as the loading vessel (Model 4601, Parr Instrument Co.). The vessel is made from stainless steel with inner diameter of 4 inches and outer diameter of 5.32 inches. The vessel can work properly at a pressure up to 1900psi and at 350°C.

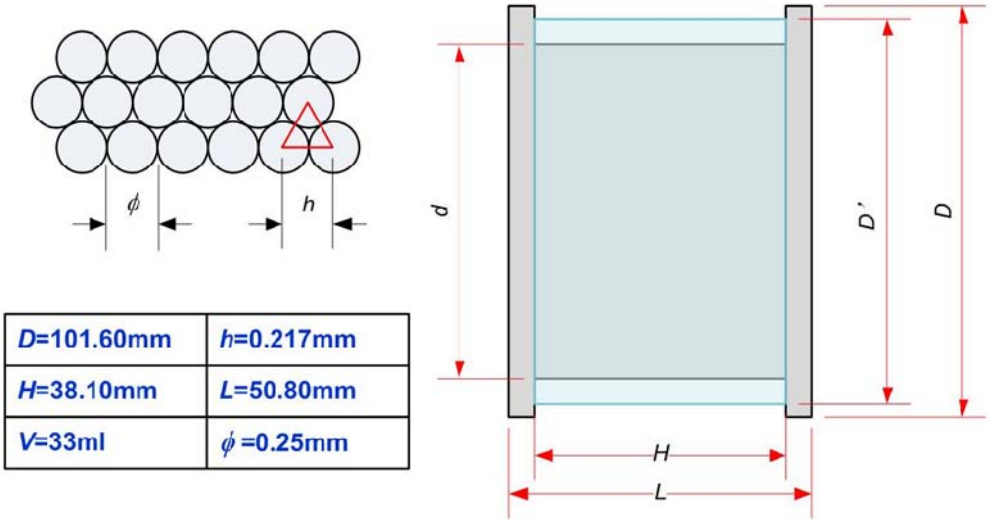

D=101.60mm	h=0.217mm
H=38.10mm	L=50.80mm
V=33ml	ϕ=0.25mm

Figure 3.1 Calculation of Bobbin Dimensions

Since the previous hydrogen loading tubing in our lab has been operated safely at 1800psi for many years, the empty volume, V, inside the new vessel was designed to be the same, which was around 33ml. Dimensions of the loading bobbin were schematically shown in Figure . The diameter, d, of the bobbin is calculated as

$$d = \sqrt{D^2 - \frac{4V}{\pi H}} = 96\text{mm}. \tag{301}$$

Since the maximum number of layers of fiber that can be winded on to the bobbin, is given by

$$N = \frac{(D-d)/2 - \phi}{h} = 11.8 \approx 11, \tag{02}$$

The maximum fiber length for each loading is

$$S = 11\pi\left(d + 2h\right) \times H \times 4 = 508\text{m}. \tag{03}$$

The remnant volume of the vessel was filled by an aluminum filling, which sat right beneath the bobbin inside the vessel.

The schematic of the hydrogen loading system is shown in Figure . The hydrogen loading procedures are:

1) Screw the guiding shaft (a 2 inches ½ inch diameter stainless steel post) into the center hole of the aluminum filling;

2) Put the wound fiber bobbin upon the filling through the guiding shaft;

3) Screw another ½ inch post to the guiding shaft to extend it;

4) Grasp the extruded post and lower the whole assembly into the vessel slowly and then remove the upper post;

5) Put on the vessel cover and tight all the bolts evenly with torque of 25lbs·inch;

6) Connect the vessel to the loading system as shown in Figure ;

7) Vacuum all the pipes, valves, vessel, and regulators for 10 minutes and then shut valve V_2;

8) Open the valve of the hydrogen cylinder and pressurize 1800psi hydrogen into the vessel and then shut all the valves.

Be aware that never use the vacuum pump to depressurize the vessel. Instead, switch V_{TEE} to the exhaust side, which should lead to a fume hood, and then open V_2 slowly to release hydrogen from the vessel.

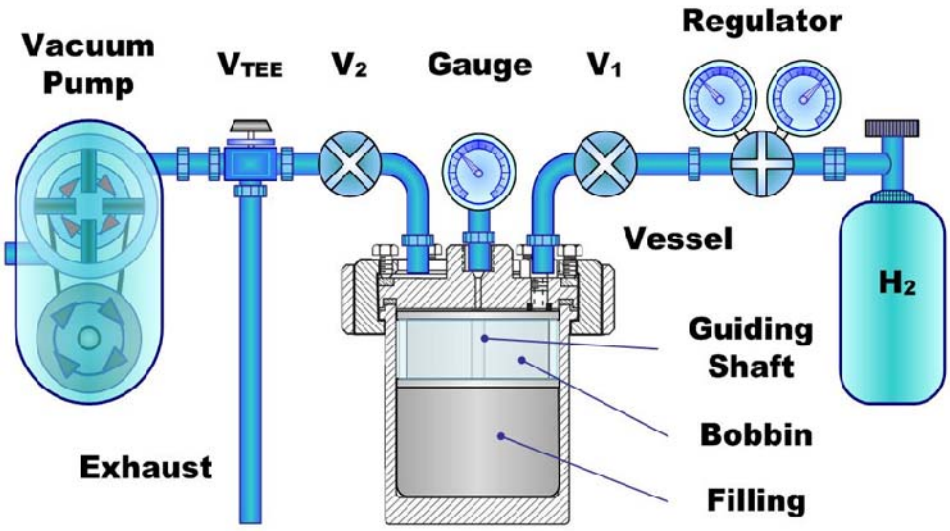

Figure 3.2 Hydrogen Loading System Diagram

3.2 Coating removal

FBG is made by illuminating the hydrogen-loaded Ge-doped fiber with 248-nm UV irradiation. Unfortunately, the epoxy-acrylate protective polymer outside the cladding of the standard single-mode optical fiber has a strong UV absorption and block the UV light from the fiber cladding and core [74]. Therefore, an essential step of the FBG fabrication is the removal of the protective polymer coating from the optical fiber. In general, three methods can be used to remove the coating from the optical fiber:

(1) First, a mechanical stripper can be used to peel the coating off. This method needs manual operation and thus is not suitable for an automated fabrication system. Besides, the surface flaws on the optical fiber induced by the mechanical stripping can degrade the strength and lifetime of the optical fiber [74].

(2) The second method is based on the chemical etching of the polymer coating with some chemical solutions such as acetone or sulfuric acid. This method has an attractive advantage that the strength and lifetime of the optical fiber are well preserved. The drawbacks of this method are the long operation time and the additional requirement of the rinsing step after the removal [75, 76].

(3) In the third method, CO_2 laser beam is used to evaporate the optical fiber coating. The fiber coating absorbs the laser energy and is heated to a temperature exceeding the thermal decomposition and vaporization point. The coating material is thus decomposed and vaporized. This non-contact method is quick and repeatable, and no surface flaws on the fiber will be created [77].

After comparison of these methods, the third method was adopted in this work as a part of the FBG automated fabrication system. To ensure that desired FBGs can be formed inside the fiber, where fiber coating is removed with CO_2 laser beam, three conditions should be satisfied:

1. The outer surface should be smooth after the coating removal, and no damage or birefringence in the fiber is introduced.
2. No significant photosensitivity degradation is introduced to the H_2-loaded fiber.
3. The length of each coating removal area should be long enough for the FBG inscription, and short enough to keep adequate fiber strength.

3.2.1 Determining the power of CO_2 laser

In order to remove the fiber coating without damaging the core and cladding structure of the fiber, the CO_2 laser induced temperature of the fiber, namely $T_{s,}$ should meet:

$$T_1 < T_s < T_2 \tag{3.4}$$

where T_1 is the temperature of the coating polymer gasification, and T_2 is the softening point of the fiber cladding and the fiber core. For commercially available optical fibers, typical T_1 and T_2 values are 200℃ and 1610℃, respectively [78, 79]. By setting an appropriate power level and adjusting the intensity field distribution of the CO_2 laser beam, the fiber coating can be removed without damaging the fiber core and cladding. To investigate the detailed configuration for the CO_2 laser, several experiments were conducted.

The initial experiment setup consisted of one CW CO_2 laser and a spherical lens. The laser beam was focused by the lens to an optical fiber. The fiber might be shifted off-focus to increase the exposure area. The average power and the duration of the CO_2 laser

pulses were controlled by a computer. With this setup, the optical fiber was heated from one side. Because a portion of the laser energy was absorbed by the optical fiber, the absorbed laser energy and hence the laser induced temperature was higher on the side facing the laser than that of the opposite side. When the temperature in the front area was slightly above T_1, the temperature in the back area was usually lower than the threshold temperature T_1. As a result, only the coating on the front side could be removed, as illustrated in figure 3.3(a). If the power of CO_2 laser was increased such that the temperature on the both sides were heated to be above T_1, and the coating of the whole segment of the fiber could be removed, as shown in figure 3.3(b).

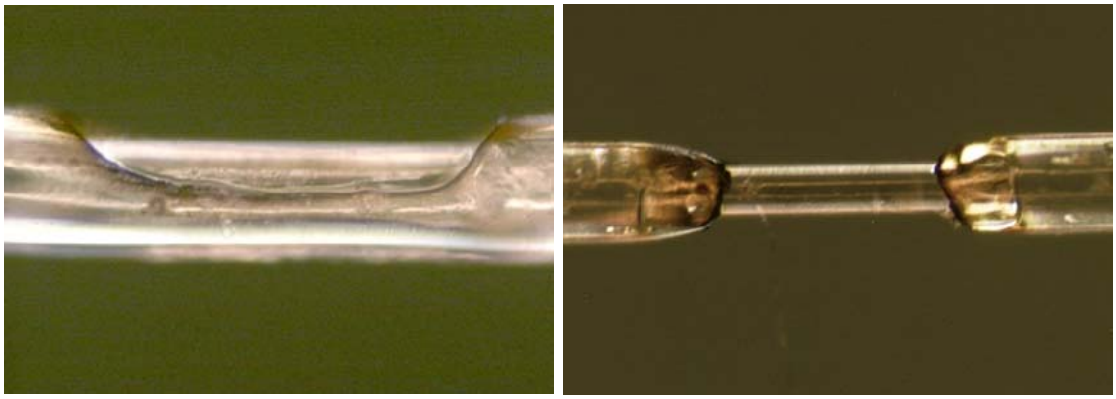

(a) **(b)**

Figure 3.3 an optical fiber with (a) partially, (b) fully, removed coating

In order to investigate the possible damage to the fiber core/cladding, FBGs were written into a fiber whose coating had been removed with the above method, and into a fiber whose coating had been removed with a mechanical stripper. All the FBG formation conditions except for the coating removal methods were the same; however, as illustrated in figure 3.4, the resulted reflection spectra of the FBGs were quite different. For the CO_2 laser ablation method, the spectrum of the FBG was not as smooth as usual, which exhibits multiple spikes near the Bragg wavelength. Since the two FBGs were fabricated with the same parameters, the difference in the spectra could only be caused by the coating removal process. At high laser power, the absorbed energy of the optical fiber was high enough to melt and diffuse the fiber core and cladding partially, which in turn made the formed FBG irregular. According to the above experiments, we concluded that

coating removal at high laser power was not appropriate as the fiber core/cladding might be damaged.

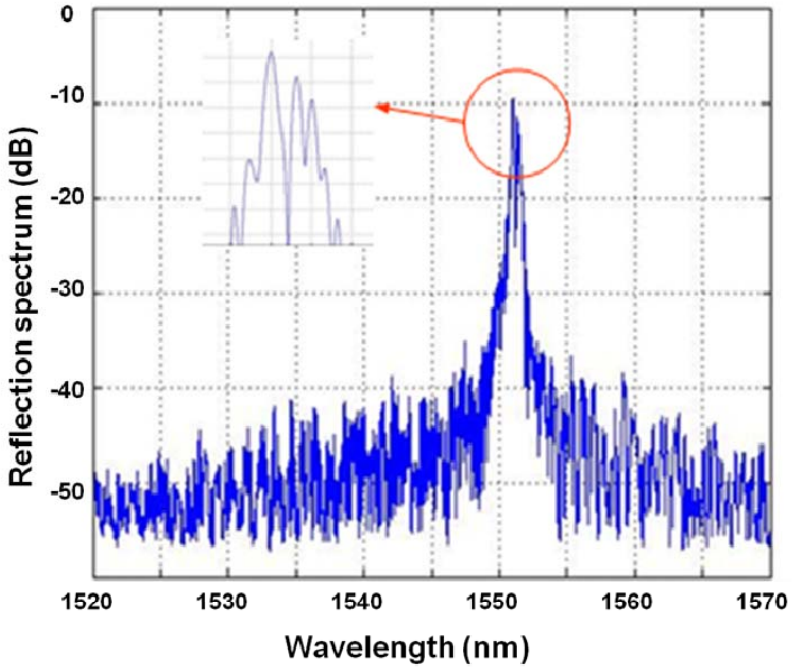

(a)

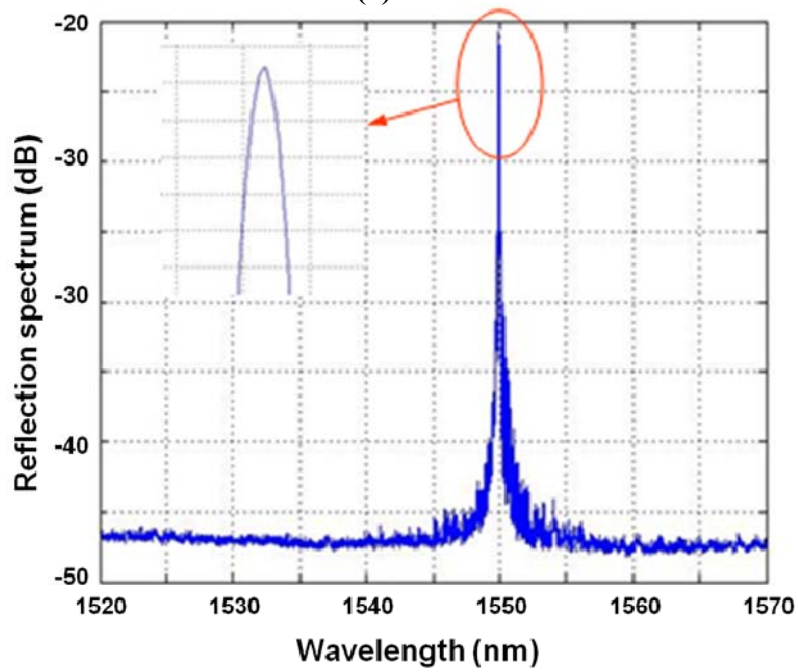

(b)

Figure 3.4 The reflection spectra of the FBGs whose fiber coating was removed with (a) CO2 ablation method and (b) mechanical stripping method

In the modified setup, as shown in figure 3.5, a 120 degree copper mirror was placed next to the optical fiber to make the laser exposure onto the fiber more uniformly by reflecting the side laser beams to the back sides of the fiber. With this setup, the optical fiber was heated from three directions, which not only improved the heating efficiency for a contant laser power output but also reduced the local temperature variance. This improvement enabled the complete de-coating at low CO_2 power level, without any noticeable change to the optical properties of the fiber.

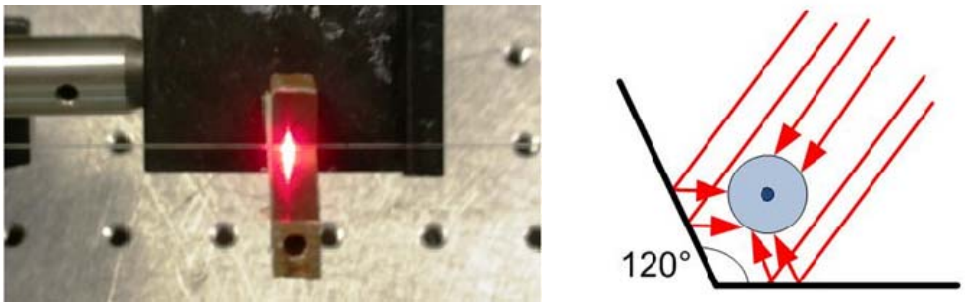

Figure 3.5 Configuration of a 120 copper mirror

Since hydrogen loading was used in this work to increase the photosensitivity of the fiber, another concern is whether the photosensitivity of the hydrogen-loaded fiber is affected by the coating removal process. To test this property, the FBG writing efficiencies were compared between the CO_2 ablation de-coated fiber and mechanically de-coated fiber. The experiment results demonstrated that the CO_2 ablation de-coating had negligible influence on the photosensitivity of the hydrogen-loaded fiber. The experiment results also indicated that, for the same de-coating length, the hydrogen-loaded fiber needed less power than the normal SMF. For example, to remove a 1.2mm-long coating, the hydrogen-loaded fiber needed 2.8W power while the normal SMF needed 3W.

3.2.2 Determining the de-coating length

As discussed before, the length of each coating removal area should be long enough for FBG formation, and short enough to keep adequate fiber strength, especially in the absence of fiber recoating. Two experiments were conducted to investigate the appropriate de-coating length.

(a) **(b)**

Figure 3.6 (a) The bare fibers wound around a pulley and (b) The fibers with different de-coating length as compared to a dime.

Table 3.1 FBGs with different de-coating lengths

De-coating length (mm)	10	5	3	1.5
Bandwidth (nm)	**0.08**	**0.13**	**0.38**	**NA**
Reflectivity (dB)	**-26**	**-39**	**-47**	**NA**

A pair of glass pieces was used to form a slit with a 5mm opening width and was placed between the phase mask and the optical fiber, to protect the phase mask from possible contamination by the coating material melted by the incident UV light. The refractive index of the de-coated fiber was modulated by the UV exposure. As for the fiber segments whose coating was not removed, almost all the UV exposure was absorbed by the coating layer, and no FBG would be formed. So for this configuration, the length of the FBG equaled the length of the de-coating area. As the de-coated fiber was away from the best position, the FBG writing efficiency was low. Typically 1 minute was needed to get a weak FBG. We compared the reflection spectrum bandwidth and peak reflectivity of the FBGs with different de-coating lengths, after exposure to UV light for 1 minute. The experiments results are summarized in table 3.1. In order to make the peak reflection close to the ideal value of -30 dB, the de-coating length should be 3-5 mm. In the whole fabrication system, some pulleys were used to guide the optical fiber in the translation stages. The major concern on the FBG strength came from the bending stress on the

pulleys. To test the strength of the bare optical fiber, several optical fibers with different de-coating lengths were wound around a dime and a pulley respectively, as shown in figure3.6. The longest length of the bare fiber that could endure the bending stress on a dime without breakage in 3 days was 5mm. Based on the results, we concluded that the appropriate de-coating length was 3-5mm.

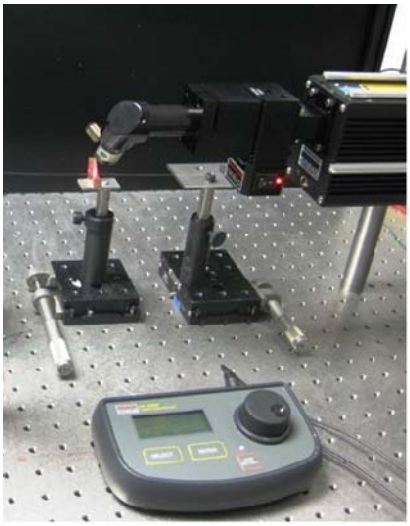

(a)

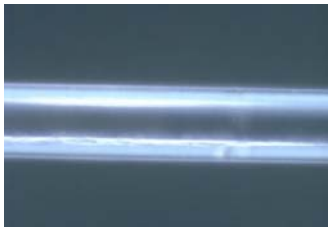

(b)

Figure 3.7 (a) Experiment setup of the coating removal system (b) Surface of a de-coated fiber

The actual coating removal system involved a CO_2 laser, a spherical lens and a 120°copper mirror as shown in figure 3.7. The focal length of the spherical lens was 4cm. The de-coating length was mainly determined by the size of the laser spot, which could be changed by adjusting the distance between the lens and the fiber. The decoated fiber surface quality depended on the power density and the distance from the fiber to the copper mirror. The optimal parameters, including 5W CO_2 laser power and 10.5cm distance between the lens and the fiber, were used to remove 3.2mm long coating of the optical fiber.

3.3 UV exposure

UV written FBGs are generally fabricated by two techniques: point-by-point writing, or phase mask modulation [68, 69]. In this research, only uniform FBGs were needed. The phase mask approach is more reliable for forming uniform FBGs, and was selected here. The principle of operation of this method is based on the diffraction and interference of

an incident UV beam onto a phase mask [69, 80]. The incident and diffracted orders satisfy the general diffraction equation, with the period Λ_{pm} of the phase mask,

$$\Lambda_{pm} = \frac{m\lambda_{uv}}{(\sin\frac{\theta_m}{2} - \sin\theta_i)} \tag{3.5}$$

where $\theta_m/2$ is the angle of the mth order diffraction, λ_{uv} is the wavelength of the UV light, and θ_i is the angle of the incident UV beam. With the UV radiation at normal incidence (θ_i=0) as shown in figure 3.8, the diffracted radiation is mainly split into m=0 and m=±1 orders. The period Λ_g of the fringe pattern created by the interference of the +1 and -1 beams is exactly one half of the period of the phase mask Λ_{pm}:

$$\Lambda_g = \frac{\lambda_{uv}}{2\sin(\theta_m/2)} = \frac{\Lambda_{pm}}{2} \tag{3.6}$$

If a photosensitive fiber is placed in such a field, the refractive index of the fiber core will be altered by the UV field with the same period, forming a fiber Bragg grating. The Bragg wavelength λ_{Bragg} relates to the period Λ_g of the interference pattern as:

$$\lambda_{Bragg} = \frac{2n_{eff}\Lambda_g}{N} \tag{3.7}$$

where n_{eff} is the effective mode index in the fiber and N is an integer indicating the order of the grating period. According to equation 3.6 and 3.7, the period Λ_{pm} of the phase mask can be determined by the desired Bragg wavelength:

$$\Lambda_g = \frac{N\lambda_{Bragg}}{2n_{eff}} = \frac{\Lambda_{pm}}{2} \tag{3.8}$$

For a first-order (N=1) grating at a Bragg wavelength of 1550 nm and a mode effective index n_{eff} of 1.45, the period Λ_{pm} of the phase mask is 1068 nm.

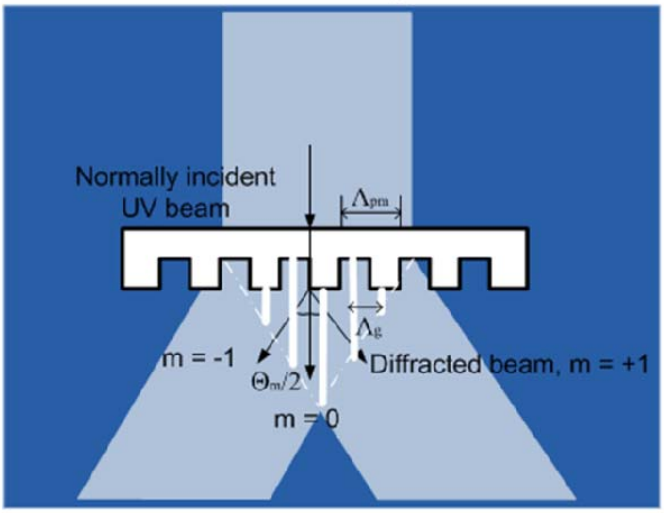

Figure 3.8 Diffraction of an incident beam by a phase mask

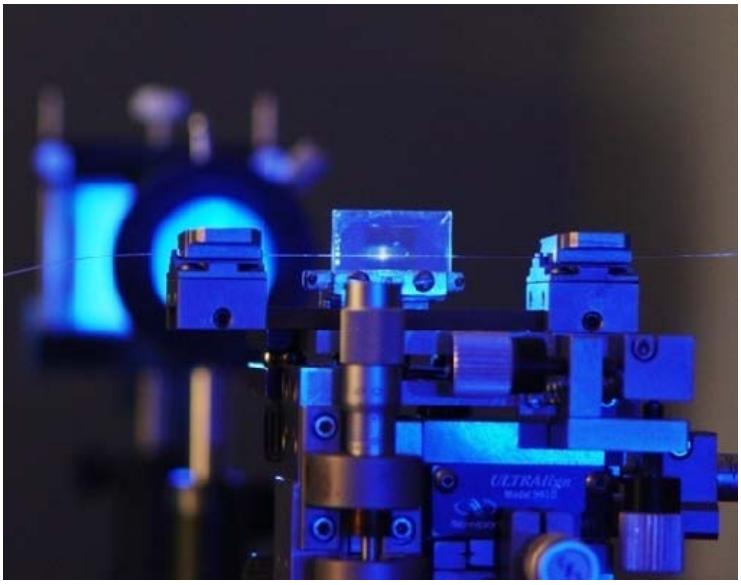

Figure 3.9 UV exposure on the optical fiber through a phase mask

Figure 3.9 shows the experiment setup for the FBG fabrication. A pulsed 248 nm KrF excimer laser was used as the UV source. The energy of a single pulse was about 35 mJ and the pulse duration was about 20 ns. The output beam size was about 6×12mm. A cylindrical lens with a focal length of 75mm was used to squeeze the input light beam into a 2x12mm light spot. The hydrogen loaded Corning SMF28 single mode fiber was placed in the focal plane. In front of the fiber, a phase mask (StockerYale Canada Inc.) was used to generate a UV light interference pattern within the fiber core. The period of the phase mask surface-relief structure was 1070.03 ± 0.02nm which results in a Bragg

wavelength of about 1550nm. The material of the phase mask substrate was UV-grade fused silica and was optimized at wavelength 248nm. The substrate size was 17.17×25.4mm with an active area 10×10mm. The diffraction efficiencies were 36.1% in the +1 order beam, 35.2% in the -1 order beam and 2.2% in the zero order beam.

3.4 Translation system

3.4.1 System overview

The most efficient way to fabricate hundreds or even thousands of high quality FBGs with moderate tolerance is to build an automated FBG writing system. In table3.2, all the actuation modules and requirements are listed, and figure 3.10 gives an overview of the system structure.

Before the FBG fabrication, the hydrogen loaded fiber was winded on the feeding bobbin. The steps listed below were followed to get the fiber prepared for the FBG writing:

1) Loaded the fiber into the system through all of the guide wheels, pre-wound the fiber onto the collecting bobbin for three turns;

2) Put fiber end through the channel of the rotary shaft;

3) Cleaved the fiber end, put it into the input ferrule of fiber rotary joint, and adjusted the position of the rotary joint to get the maximum light coupling efficiency;

4) Turned on the power switches of the control box and the fiber collecting mechanism;

5) Turned on the switches of the CO_2 laser and Excimer laser;

6) Run the control software on a computer.

Table 3.2 List of actuation modules of FBG automation system

Module/Part	Function Description	Adjustable Parameters
Feeding bobbin	Works as a fiber feeder as well as the hydrogen loading bobbin.	N/A.
Guiding Wheel	Guides the position or translation direction of fiber between modules.	N/A.
Forward Mechanism	Precisely controls the fiber translation in the system. Powered by a computer controlled stepper motor.	Rotation of the forward wheel. Driver roller press. Fiber position (3D).
Coating Remover	Removes a segment of fiber coating by CO_2 laser. The length of the segment is controlled by a computer, and the position is controlled by the fiber forward mechanism.	Laser pause power and duration.
UV Exposure	Writes FBG onto fiber by UV laser exposure. The UV pulses intensity, pause width, and exposure duration are controlled by a computer. The writing position is controlled by the fiber forward mechanism.	UV pause power, pause width and exposure duration. Slit opening width. Fiber position (5D).
Electric Magnet Clamps	Fixes the fiber position on the UV exposure stage before UV exposure. The operating timing of the two clamps is separately controlled by a computer.	Timing of close or open.
Fiber Collecting Mechanism	Collects the fed fiber and wind it on to the collecting bobbin. It is powered by a DC motor.	Tensing of the winded fiber.
Optical Rotary Joint	Provides an optical path between the fiber spectrum analyzer and the fiber on the rotary bobbin, which enables monitoring of FBG spectra during grating writing.	N/A.

At the beginning, the control software applied an electric break on the stepper motor which drove the forward wheel and turned on the DC motor. Because of the friction pad design in the collection mechanism, the fiber remained still with certain tension. The stepper motor moved the fiber segment for the first FBG to the focusing spot of the

CO_2 laser. The software then turned on the CO_2 laser to decoat about 3mm length of fiber coating. After this, the stepper motor drove the ablated fiber segment to the UV exposure area right behind the slit, then the two electric magnet clamps fell to fix the fiber during exposure. During the exposure, the DC motor in the collection mechanism was turned off to minimize possible vibration. After several pulses of UV exposure, the UV laser stopped; the DC motor started to rotate; the two clippers were lifted up, and the stepper motor drove the next expected FBG position to the CO_2 focus area for the second grating. A movable fiber winding guide, which was synchronized to the rotation of the collecting bobbin, secured the evenly winding of the fiber on to the bobbin.

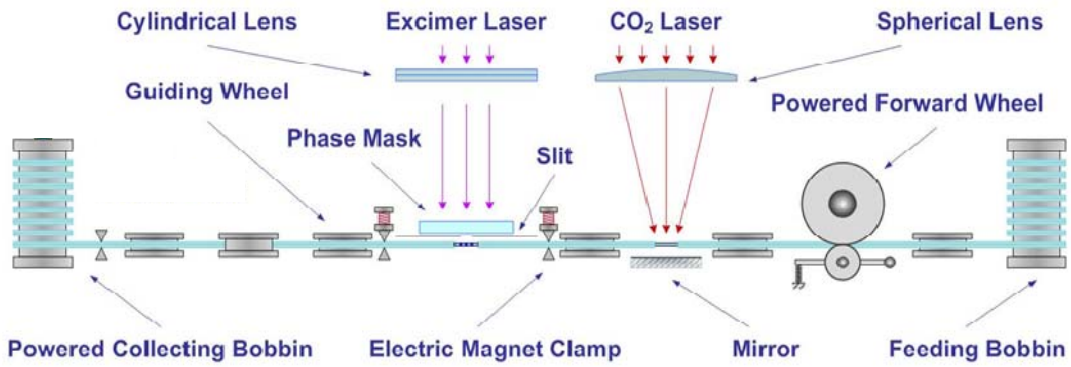

Figure 3.10 FBG writing system diagram

3.4.2 Fiber forward mechanism

In order to drive the fiber movement precisely, the forward-moving mechanism was put before the coating ablation. An aluminum drum with a V-groove on the circumference was machined. The depth of the groove was designed to enable only half of the coated SMF-28 set into the groove. A precision urethane fiber press roller was mounted on the middle of a lever. A pulling spring at the end of the leaver was used to generate adequate friction between the fiber and the drum. Since there was no sliding movement between the fiber and the drum, by controlling the rotation of the drum through the stepper motor, the translation of the fiber was precisely determined. The whole mechanism was mounted on a 3D translation stage, which enabled the precise control of the fiber position relative to the CO_2 laser ablation mirror to optimize the ablation quality. A picture of the fiber forward mechanism is given in Figure 3.11.

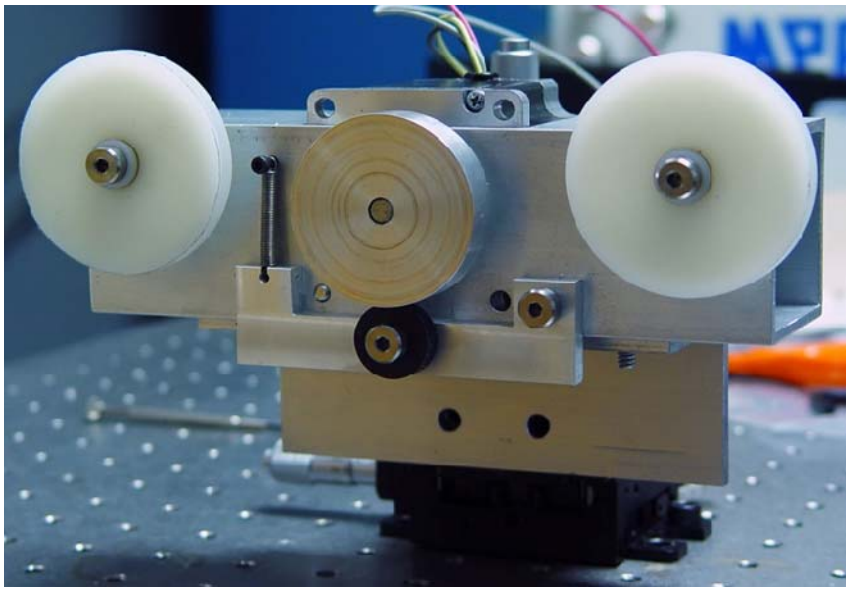

Figure 3.11 Fiber feeding system

A 4-wire Bi-Polar stepper motor (Portescap 23H118D10B) was selected for rotating the drum and translating the fiber. Its main specifications are:

Voltage: 6.8VDC; Driving Current: 1A; Step Angle1.8°; Body Diameter: 2.25" (57.15mm); Shaft Diameter: 0.250" (6.35mm); Mounting Hole Spacing: 1.86" (47.14mm); Lead Length: 12.00" (304.80mm)

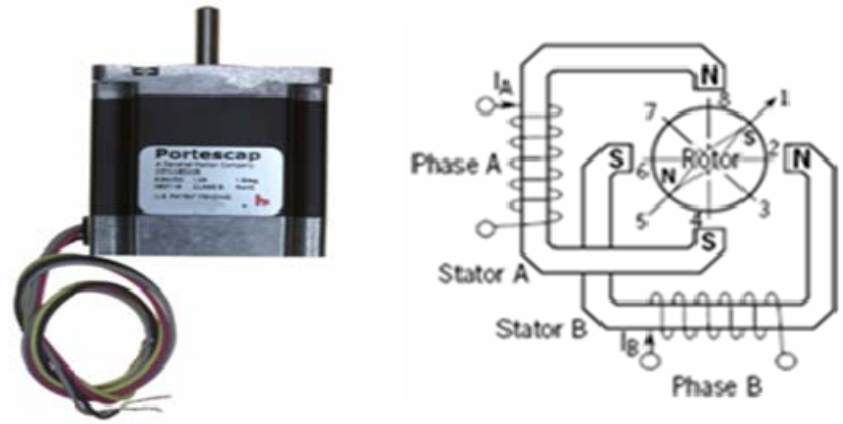

Figure 3.12 (a) Stepper motor (b) Schematic of the stepper motor

The exterior appearance and internal structure of the stepper motor are shown in figure 3.12. Such a stepper motor operates with the principle that magnetic attraction and

repulsion convert digital pulses into mechanical shaft rotation. The amount of rotation achieved is directly proportional to the number of input pulses generated, and the speed is proportional to the frequency of these pulses. The stepper motor has a permanent magnet and an iron rotor, together with a stator. The torque required to rotate the stepper motor is generated by switching (commutation) the current in the stator coils as illustrated in figure 3.12. Although only 4 stator poles are shown in figure 3.12, in reality there are numerous tooth-like poles on both the rotor and stator. A positional increments (steps), here 1.8 degrees, can be achieved by switching the coils.

There are four most common drive modes for a stepper motor [81]: Wave Drive (1 phase on), Full Step Drive (2 phases on), Half Step Drive (1 & 2 phases on), and Microstepping (Continuously varying motor currents).

In Wave Drive mode, only one winding is energized at any given time. The stator is energized according to the sequence $A \to B \to \overline{A} \to \overline{B}$ and the rotor steps from position 8→2→4→6. The disadvantage of this drive mode is that only 50% of the total motor winding is used at any given time, and thus the maximum torque output from the motor cannot be obtained.

In Full Step Drive mode, two phases are energized at any given time. The stator is energized according to the sequence $AB \to \overline{A}B \to \overline{A}\overline{B} \to A\overline{B}$ and the rotor steps from position 1→3→5→7. Full step mode results in the same angular movement as 1 phase on a drive but the mechanical position is offset by one half of a full step. The torque output of the unipolar wound motor is lower than the bipolar motor (for motors with the same winding parameters) since the unipolar motor uses only 50% of the available winding while the bipolar motor uses the entire winding.

Half Step Drive combines both wave and full step (1&2 phases on) drive modes. Every second step only one phase is energized and during the other steps one phase on each stator. The stator is energized according to the sequence $AB \to B \to \overline{A}B \to \overline{A} \to \overline{A}\overline{B} \to \overline{B} \to A\overline{B} \to A$ and the rotor steps from position 1→2→3→4→5→6→7→8. This sequence results in angular movements that are half of

those in 1- or 2-phases-on drive modes. Half stepping can reduce a phenomena referred to as resonance which can be experienced in 1- or 2-phases-on drive modes.

In Micro-stepping Drive mode, the currents in the windings are continuously varying to be able to break up one full step into many small discrete steps. We are not going to give more details here since it is complicated and is not adopted in this system.

According to the preliminary experiments, a large and constant torque is essential to drive the fiber smoothly and to hold the position of the fiber firmly. Full step mode met the requirement the best and was adopted. The first version of the stepper motor driver is given as figure 3.13. Table 3.3 gives the output current at different combination of control signal. Provide appropriate control signals D0-D3 such that the current flow with the sequence $AB \to \overline{A}B \to \overline{A}\overline{B} \to A\overline{B}$, the motor will then rotate with Full Step Drive mode.

Table 3.3 Current output with different control voltage

D0	D1	Current	D2	D3	Current
0	0	no	0	0	no
1	0	$A \to \overline{A}$	1	0	$B \to \overline{B}$
0	1	$\overline{A} \to A$	0	1	$\overline{B} \to B$
1	1	forbidden	1	1	forbidden

When a proper current is applied to the stepper motor, the motor as well as the connected gear turn to the corresponding position. When the current is turned off, if the load to the stepper motor is not large (e.g. less than 0.1N), the friction of the motor/gear system will hold the position. However, the load in the system is relatively large, and once the current is turned off, the fiber will be drawn back and cause uncertainty to the whole system. In order to hold the position of the fiber firmly, the driving current needs always to be applied to the motor during the operation of the system. In the circuit shown by figure 3.13, the four transistors T1, T3, T5 and T7, had Vce values of about 1 volt when 1A current was flowing through the collector and emitter. About 1 watt heat dissipated out of the transistors and heated the transistors to a high temperature quickly. The transistors might even be damaged if the high temperature lasts for over a few minutes.

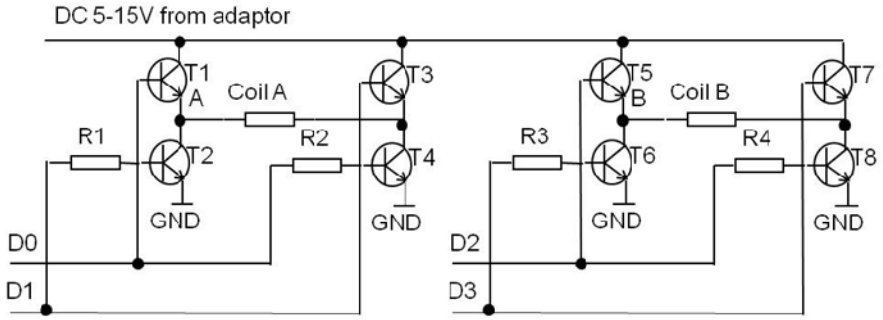

Figure 3.13 Schematic of rotary stage driving circuit

The stepper motor driver was modified to reduce the heat dissipation. The final version is given as figure 3.14. Four pairs of PNP and NPN transistors, whose saturation Vce values were less than 0.1 volt were used to replace the eight NPN transistors in the previous version. Given the same current of 1A, the power dissipation was reduced to 0.1V*1A=0.1 Watt only. An electric fan was used to chill down the heat sinks, so the transistors were able to work continuously. In the new version of circuit, a variable voltage regulator LM317 was used to reduce the working voltage of the stepper motor to Vcc (about 4 volts). As a result, the power dissipation could be further decreased, and an operational amplifier LM324 was adopted to convert the logic 0 and 1 to the adequate analog voltage levels of 0 and Vcc. Only two control inputs were needed: D0 and D1. They were used to control two motor coils independently. When D0/D1 was zero, 1A current flew from the left end of the coil 1/2 to the right end of the coil 1/2. When D0/D1 was 1, 1A current flew from the right end of the coil 1/2 to the left end of the coil 1/2. Thus, by providing a control sequence of D0D1=00→10→11→01, a current sequence of $AB \to \overline{A}B \to \overline{A}\overline{B} \to A\overline{B}$ could be achieved, and the motor then rotated with Full Step Drive mode.

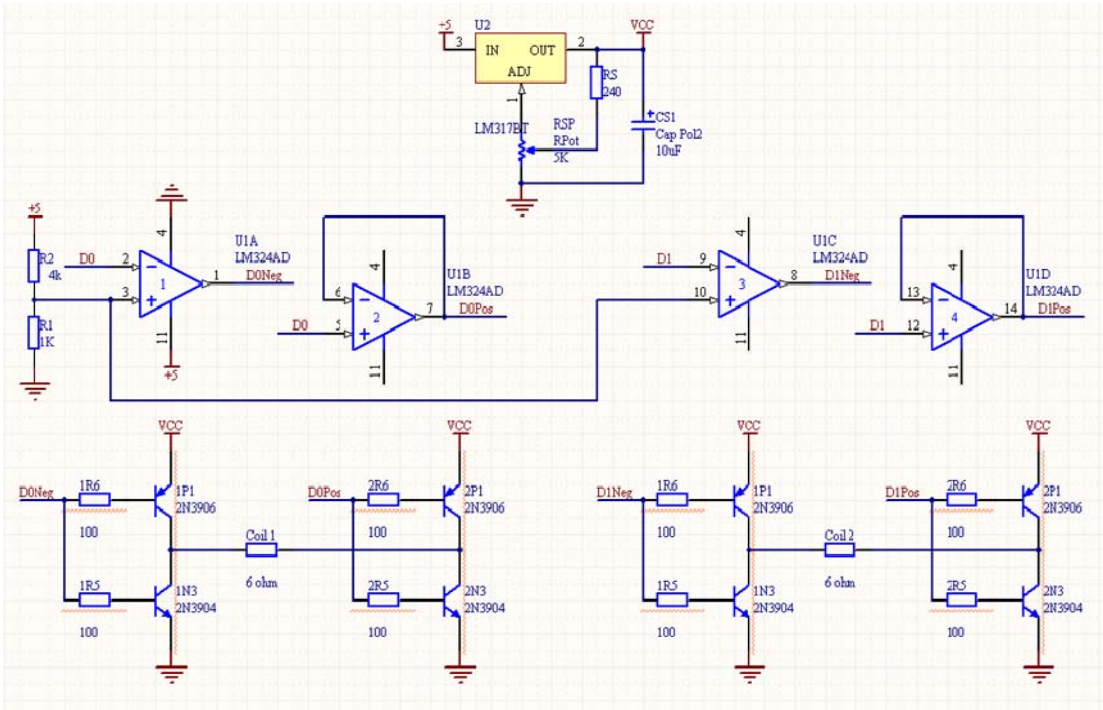

Figure 3.14 Final version of the stepper motor driver circuit

3.4.3 Electric magnet clamps

Any vibration during the FBG writing is harmful or even fatal; so two fiber holders (Newport 561-FH) controlled by two electric magnets were used to hold the fiber firmly during the UV exposure. The two magnets were modified from two 12V 5A relays. Two leavers made from copper sheet were used to pump up the holder clamps when current was applied on to the electric magnets. Since when the clamp was closed, a magnet on the holder prevented it from opening, a fairly strong force was needed to open it. When the clamp was open, only a little force could keep it from falling closed. To avoid overheating the electric magnets, pulse-width modulated (PWM) solenoid drivers (DRV102, Texas Instrument) were used. The DRV102could be set to provide a strong initial closure, automatically switching to a soft hold mode for power savings. The schematic of the circuit is shown in figure 3.15. With the parameters shown in the figure, the initial DC output duration was around 90ms, and the duty cycle for the PWM mode was about 25%. A picture of the mounted electric magnet clamps is also given in figure 3.16

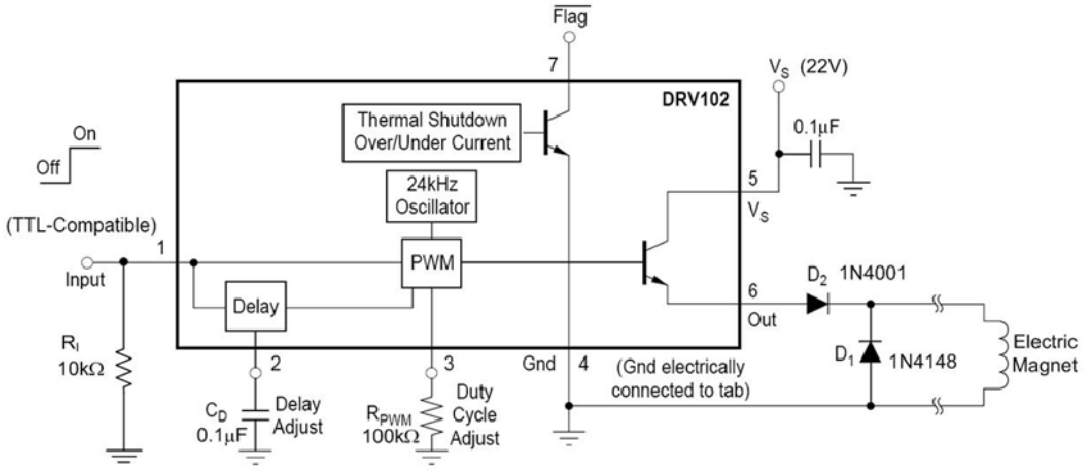

Figure 3.15 Schematic of electric magnet driver

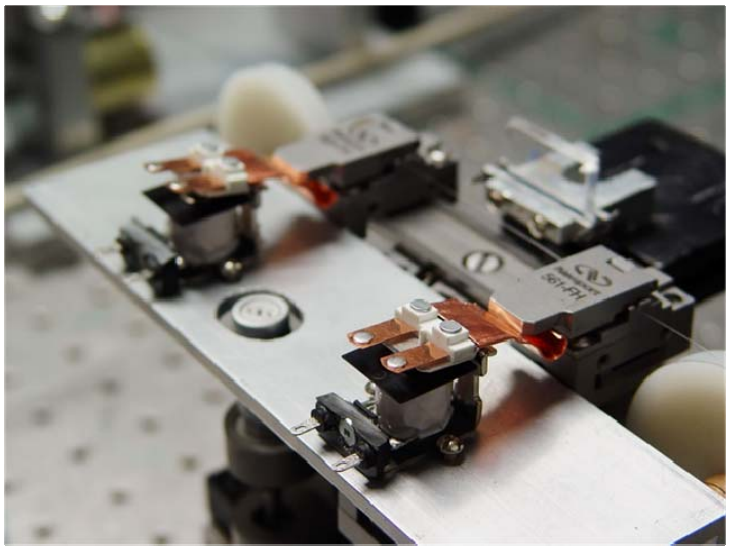

Figure 3.16 Electric magnet clamps

3.4.4 Fiber collection mechanism

Although only 3mm of coating was removed at each FBG spot, special care was still required when rewinding this fiber into the collecting bobbin. Therefore, an automated fiber wind guide was designed and it was synchronized to the rotation of the collecting bobbin, which helped wind the fiber evenly. The schematic of the fiber collection mechanism is shown in **Error! Reference source not found.**. A coding wheel was attached on the right end of the bobbin. Two position sensors, PS1 and PS2, could pick up the motion of the bobbin and then a controller calculated the required translation of

winding-guide and moved the guide by a stepper motor (Portescap, 42M048C1U) and a lead screw. Because the pitch of the lead screw was 1mm and the coated fiber diameter was 0.25mm, the lead screw needed to rotate one turn for each of four turns of the bobbin. Two other position sensors, PS3 and PS4, were used to flip the moving direction of the winding guide when it reached the edges of the collecting bobbin. A DC motor was used to drive the bobbin. Because of the adoption of the friction pads, the bobbin could be stopped by certain amount of fiber tension, which could be adjusted by a screw knob. For simplicity, the controller was made with analog and logic chips, so no computer was needed to control the synchronization of the bobbin and winding-guide, which made this mechanism a standalone module. The only control was to turn on or off the power of the DC motor. The real experimental setup is given in figure 3.18.

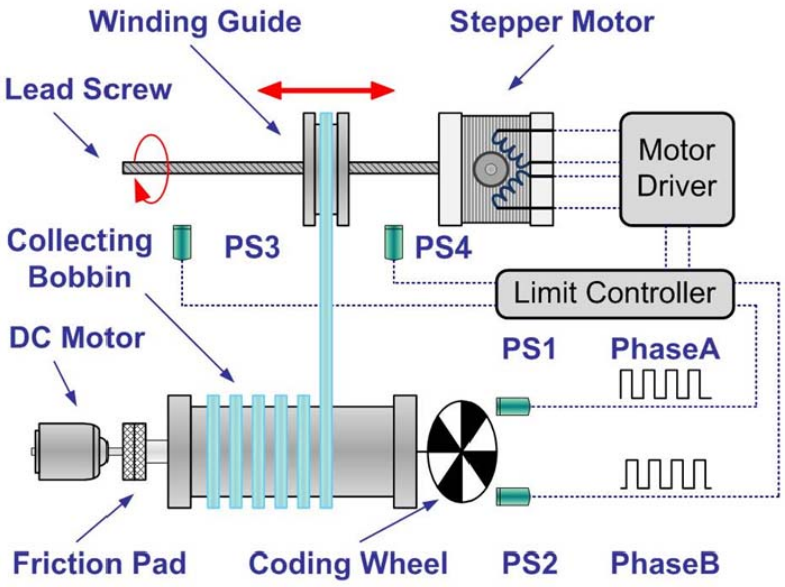

Figure 3.17 Schematic of the fiber collecting mechanism

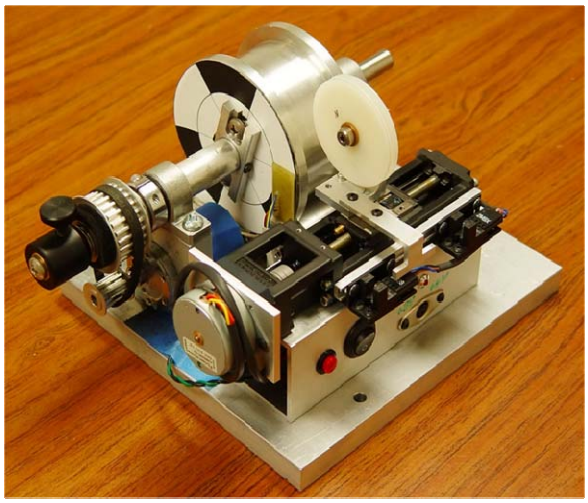

Figure 3.18 Real fiber collection mechanism

3.5 FBG mass production system

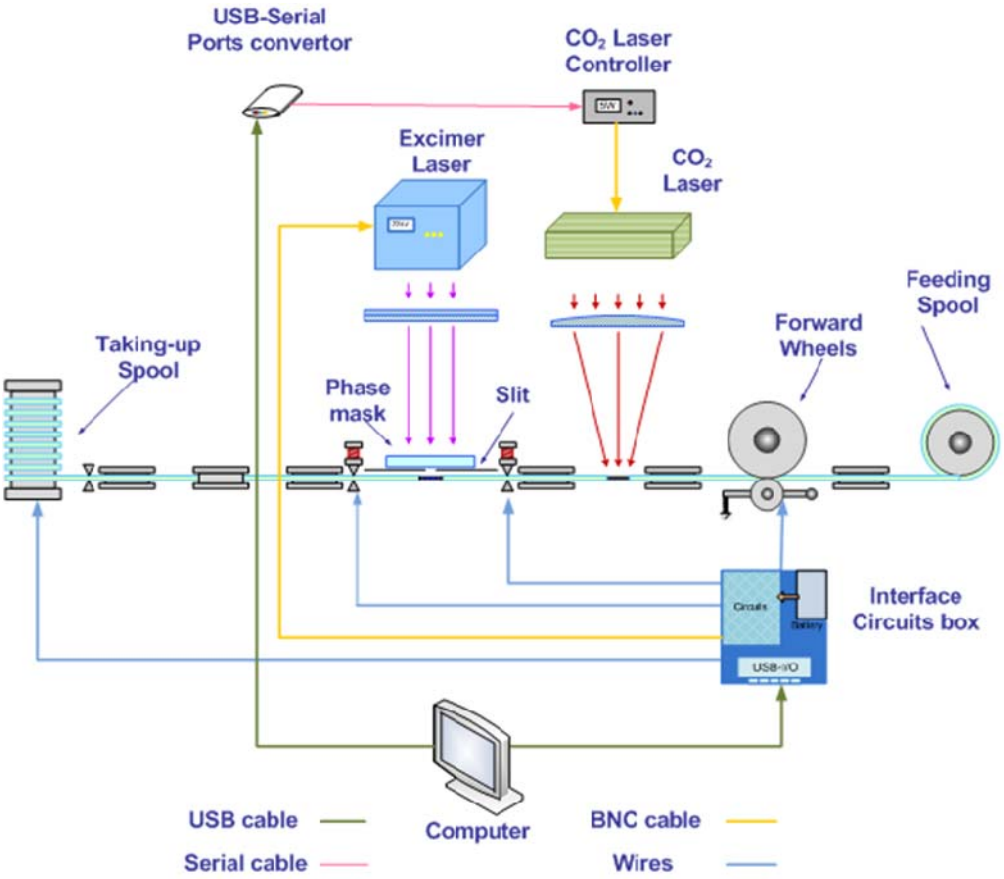

Figure 3.19 Schematic of the automated FBG fabrication system

The overall FBG mass production system is shown in figure 3.19. As discussed earlier,

there were four major functional parts in the automatic FBG fabrication system: the CO_2 laser coating removal system, FBG writing system, fiber feeding system, and fiber collecting system. A computer was used to control some of the devices in these subsystems such that the whole system could be synchronized for automatic FBG fabrication. The controllable devices include: the stepper motors, the CO_2 laser in the coating removal system, the excimer laser in the FBG writing system, and two latches in the fiber feeding system and a linear motor in the fiber collecting system. Some home-made circuits were used to produce adequate control voltage and current to the devices, and a Graphical User Interface (GUI) program was designed to generate the control signal from a computer.

3.5.1 Interface circuits box

As illustrated in figure 3.20, an interface circuit box was built to realize the communication between the computer and the fiber feeding system, the FBG writing system and the fiber collecting system. The interface circuit box consisted of a switch, a transformer, a DC power supply, a cooling fan, a circuit board, and an USB-digital I/O convertor. The transformer (Hammond 164J16) with the maximum 36VA output power provided 16V AC voltage to a bridge circuit, which offered the adjustable DC power supply to the control circuit of the two relays as introduced earlier. The DC power supply had 12V and 5V output and served as the power supply to the control circuits of the stepper motor and the linear motor. A cooling fan was installed towards the stepper motor driver to cool down the power transistors. The control circuits of the stepper motor, the linear motor and the relays were mounted on the same circuit board. The National Instruments USB-6501 with 24 digital I/O lines was used to provide the input signal of each control circuit. Each line could be configured by the computer via the USB port. For each digital line, the high output corresponded to 3.5-5V and the low output corresponded to 0-0.2V. In this work, lines p0.0 and p0.1 were used to control the direction and speed of the stepper motor; line P0.2 was used to control the on/off of the linear motor; line p0.3 and p0.4 were used to control the on/off of the two relays, respectively, and line p0.5 was used to control the on/off of the excimer laser.

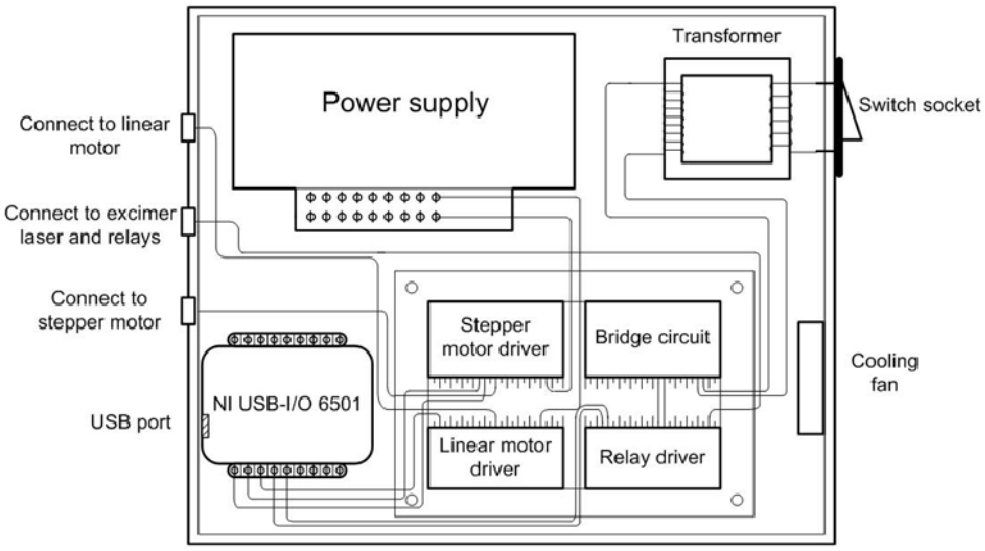

Figure 3.20 Schematic of the interface circuit box

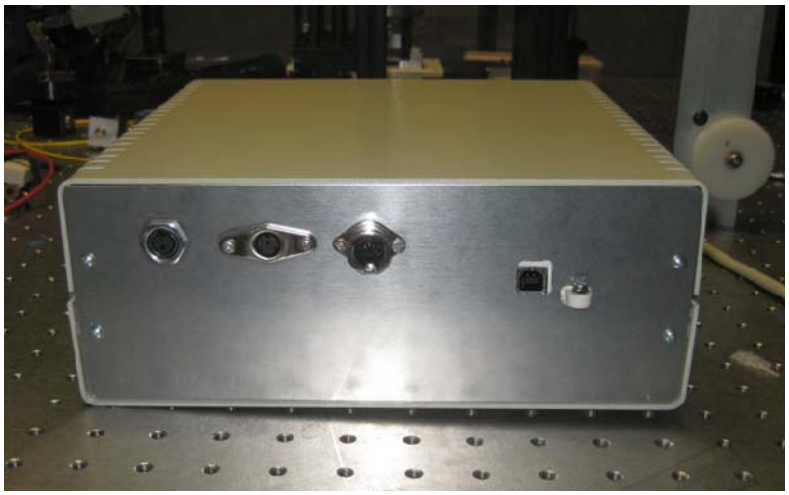

Figure 3.21 Front panel of interface circuit box

Stepper motor:

When the lines p0.0 and p0.1 output the sequence {1,0},{1,1},{0,1},{0,0}, the stepper motor would rotate 1.8° clockwise for each step. The diameter of the pulley driven by the stepper motor was 47.2mm, so the optical fiber would move 1.48mm at each step. Thus the frequency and the number of the output sequence were used to adjust the speed and the distance of the fiber movement.

Linear motor:

When the output of line p0.2 was high, the linear motor would be powered and a torsional force was produced to wind the fiber around the spool, and prevented the fiber from tangling. When the output of line p0.2 was low, the linear motor stoppd, and the fiber could be operated manually.

Relays:

Line p0.3 and p0.4 were used to control the on/off of the two relays respectively. When the output of the line was high, the corresponding relay would be on and the fiber would be clamped on the optical stage firmly. When the output of each line was low, the relay would be off and the fiber could move smoothly along the translation stage. These relay pairs were used to release the strain of the fiber during UV exposure, so the Bragg wavelengths of the resulted FBGs would not be differ too much.

Excimer laser:

Excimer laser (MPB MSX-250) worked in the remote control mode. The output of line p0.5 served as the external trigger signal of the laser. The pulse power level was usually pre-set from the front panel of the laser. The pulse number and the repetition rate could be controlled by the computer and the trigger signal. Figure 3.22 shows the waveform of a 2Hz trigger signal.

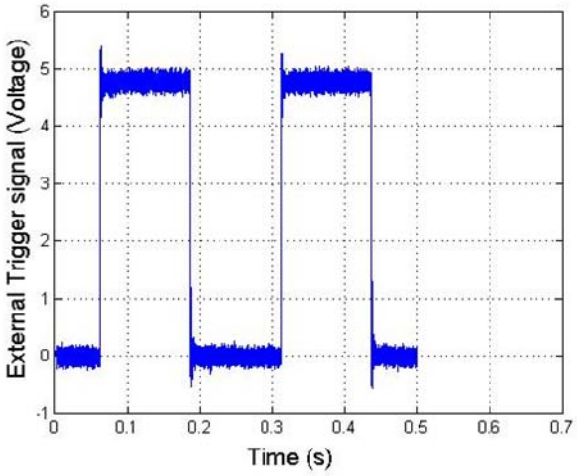

Figure 3.22 The external trigger signal of the Excimer laser

Figure 3.23 Picture of the Excimer laser

CO_2 laser

The CO_2 laser used in the system is made by SYNRAD, Inc (Model 48-1). The wavelength emitted by the laser is 10.6 μm, and the maximum output optical power under continuous mode operation is 10 W. The control of the CO_2 laser output involved two parts: the power level control and the lasing duration control. The power level control could be accessed by the laser controller and the pulse duration could be controlled by setting the laser enable and disable time from the controller. The computer communicated with the CO_2 laser controller through a USB-serial port convertor (NI) and a serial port.

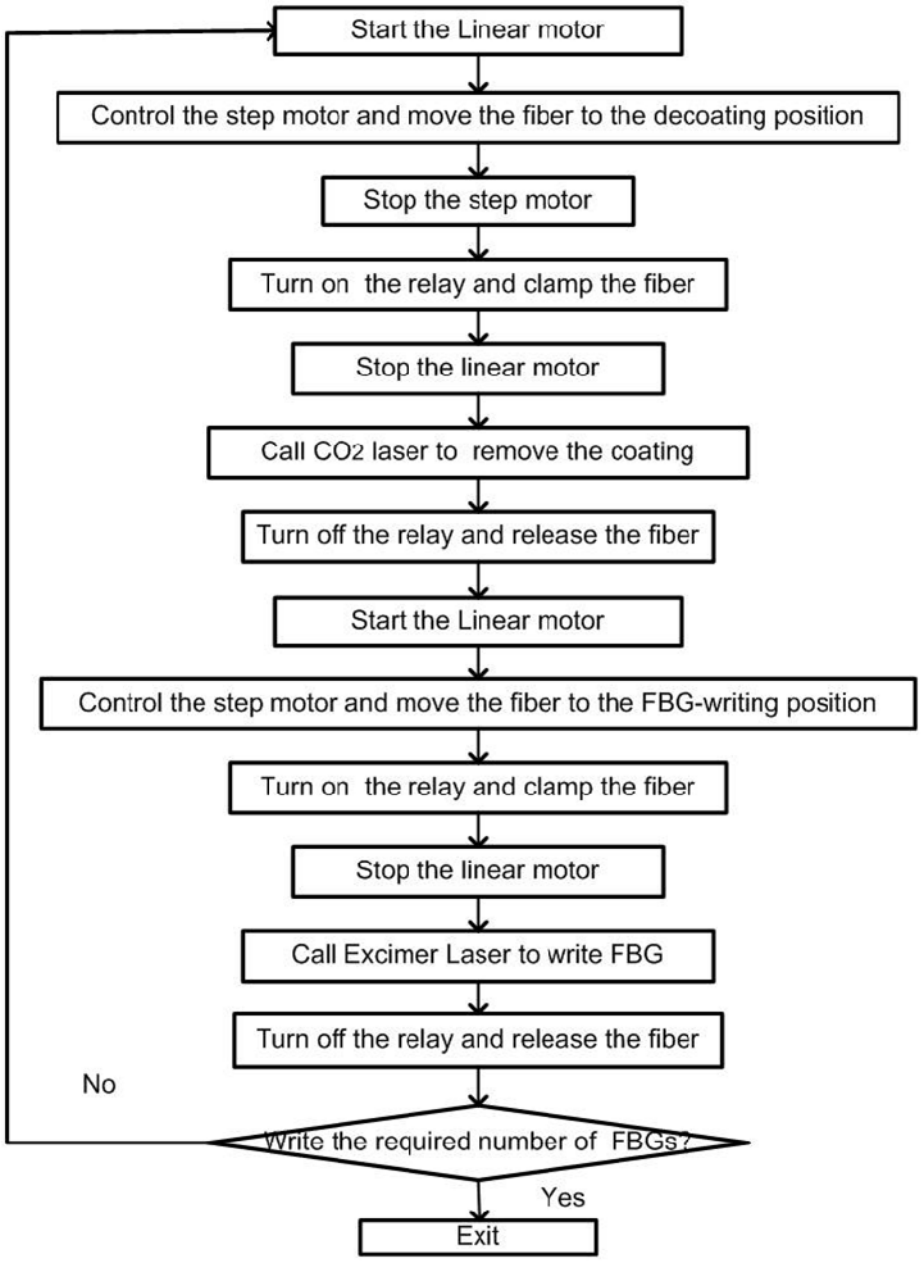

Figure 3.24 Block diagram of the automated FBG fabrication program

3.5.2 Software design and program development

Special computer software was developed to synchronize the whole automated FBG fabrication system. The program was implemented in C++ language so that both graphic interfaces and high computational speed were achieved. A block diagram of the program

is shown in figure 3.24. There were five devices that needed to be controlled in the whole system: the stepper motor in the fiber feeding system, the linear motor, the excimer laser, the relays and the CO_2 laser. In order to debug the system conveniently, the software was designed to support two modes: manual control mode, in which each device was controlled manually and separately; and automatic mode, in which all the devices were controlled automatically.

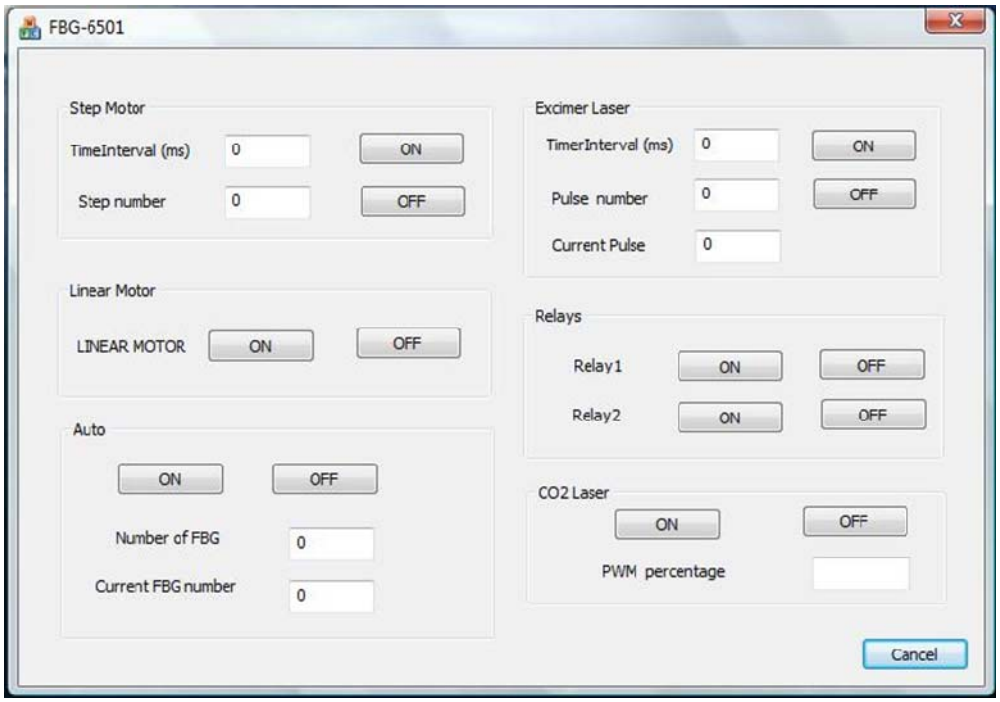

Figure 3.25 Graphic user interfaces (GUI) of the automatic FBG fabrication program

Manual mode

For the stepper motor, two TTL control signals were required to generate the appropriate control sequence, which further defined the rotation direction, rotation speed and rotation angle of the stepper motor. Practically only one rotation direction was allowed in the system, so in the software control interface, there were two parameters to be specified: “Time Interval”, which defined the rotation speed, and “Step number” which defined the angle of rotation. If we clicked the “On” button on the right of the stepper motor control

interface, the code would generate the control sequence such that the stepper motor rotated at the specified speed and to the desired angle.

The linear motor and the two relays simply switched between ON or OFF mode and were controlled by the TTL signals, respectively. In the software control interface, there were one ON button and one OFF button for each of the above three devices. Clicking ON would enable the device to work, and OFF would stop the device.

As for the excimer laser, two parameters could be specified: “Time Interval” defined the repetition rate of the excimer laser pulses, “pulse number” defined number of the laser pulses generated for fabricating a single FBG which determined the strength of the FBG under the constant pulse power condition. “Current pulse” showed the number of pulses generated in the current sequence already.

The CO_2 laser worked under the pulse width modulation (PWM) mode, and the parameter of PWM percentage could be altered from 0 to 100%, corresponding to an average output power of 0 W and 10 W, respectively.

Automatic mode

Under the automatic mode, the whole system was synchronized by a software timer, and different devices would be activated and deactivated at predetermined timer phases. The fabrication process of multiple FBGs could be summarized as following:

1. Move the optical fiber to a certain position and remove the coating of the fiber with the CO_2 laser;

2. Move the de-coated fiber to the FBG-writing position. Enable the two relays to fix the optical fiber, and then start the UV exposure;

3, Stop the UV exposure when a desired FBG is produced;

4. Release the two relays, move the fiber for about one meter, and then repeat steps 1-3 until the desired number of FBGs are produced. With the parameters listed in table 3.4, it took only 48 seconds to write one FBG. This mass production line not only improved the

fabrication efficiency but also contributed to the system power budget by reducing the splice loss.

Table 3.4 The fabrication time of one FBG with different parameters

Travel steps	Interval time of steps (ms)	Pulse number of Excimer laser	Interval time of pulses (Hz)	Total time/ FBG
676 (1m)	200	15	500 (2Hz)	1 min 30s
676 (1m)	100	15	200 (5Hz)	48s

3.6 Calibration procedures

The output power from the UV light usually decreased after a few weeks, due to the gas leakage. The photosensitivity of the H_2-loaded fiber also decreased after a few days due to the escape of the hydrogen molecules. Since the feedback control part has not been included in the current FBG fabrication system, the FBG writing process should be calibrated to ensure the reflectivity of the fabricated FBG fall into the acceptable range (-30 ~ -45dB). Practically the calibration was taken for production of every 50 FBGs. Figure 3.26 shows the setup for the calibration system. As introduced earlier, the UV exposure method was adapted to write FBG onto the photosensitive fiber. A glass slit with a 5mm opening was placed between the phase mask and the optical fiber, to protect the phase mask from the possible surface contamination by the spills of the coating melted by the incident UV light. Only a small portion of the UV light that passed the opening could reach the optical fiber, and the remaining light would be blocked by the glass slit. Thus during the fabrication, the section of the fiber without coating should be moved accurately to the opening area. The end reflection was cancelled by twisting the far end of the fiber at a small angle. A 3dB circulator was used to connect the fiber to a high resolution swept laser interrogator (Micron Optics, Inc). The wavelength range of the embedded swept laser was from 1520nm to 1570nm with 2pm resolution. The spectrum acquired by the interrogator could be sent to a personal computer through an Ethernet cable.

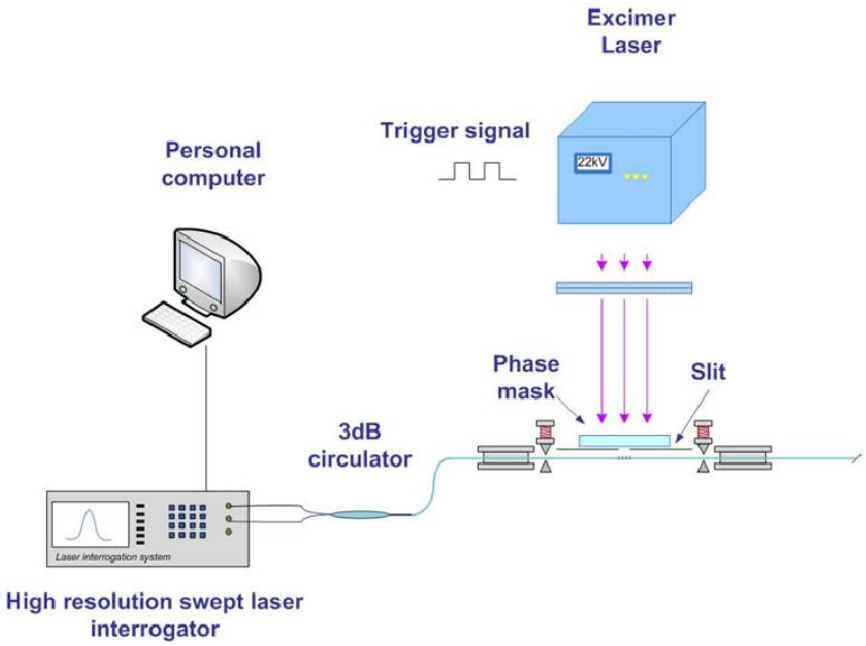

Figure 3.26 FBG spectrum calibration system

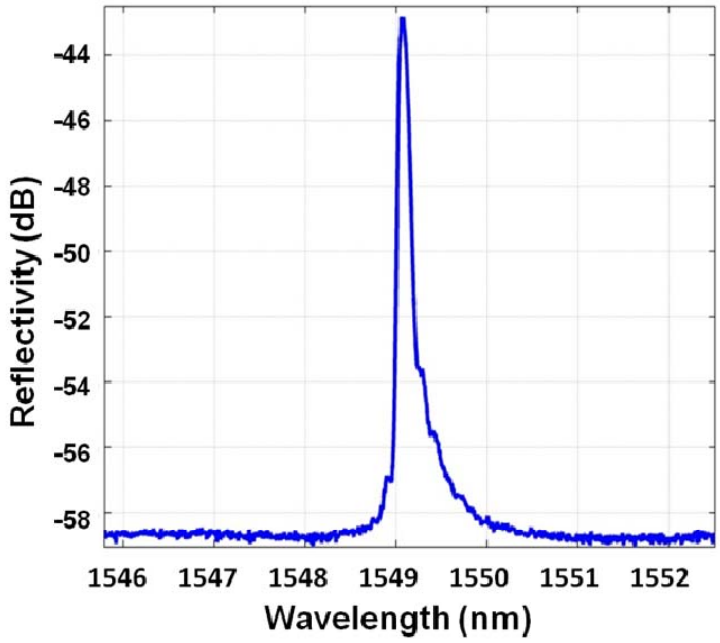

Figure 3.27 The typical spectrum of an ultra-weak FBG (-43.6 dB)

The strength of an FBG is mainly affected by the refractive index modulation Δn [69], which is determined by the photosensitivity of the fiber, the pulse power of the UV light and the number of laser pulses. To increase the photosensitivity, the optical fiber was

placed in the hydrogen chamber under 1500 psi for 3 days and then stored in a freezer (-20°C) before the use. The peak power of the UV pulse is 35mJ, and the repetition rate is 5Hz. If the laser is operated at pulse repetition rate greater than 10Hz, the laser must be connected to a source of cooling water. Thus, the repetition rate was controlled under 10Hz in this work. During the calibration, the number of pulses was counted until the reflectivity of the FBG reached around -40dB. With the same number of pulses, the FBG writing process was repeated 3 times to ensure the number of pulses was proper. The typical spectrum of an ultra-weak FBG is shown in figure 3.27. Taking into account the loss induced by the circulator and the connectors, the peak reflectivity of this FBG was estimated to be 3dB higher than that shown in figure 3.27, which was approximately -40 dB.

3.7 Performance of fabricated sensors

To test the performance of the FBG fabrication system, 100 FBGs were fabricated on an optical fiber with 1m separation distance. 50 FBGs were written at one time. When the wavelength of the tunable laser was set to a certain wavelength, the intensity of the returned pulses from each FBG was detected and shown in figure 3.28, and different FBGs were distinguished by different time delays. The wavelength of the tunable laser was scanned over 3 nm with a step of 0.05 nm; the reflectivity of each FBG at the scanned wavelength could be derived from the returned signal at the corresponding time delay. The reflection spectra of all the FBGs were thus obtained. In figure 3.28, different colors represent the pulses at the different wavelengths and the readout voltage from the photo detector represents the pulse intensity. The peak reflectivity of these 100 FBGs varies from -37dB to -50dB. Figure 3.29 shows the spectra of the FBGs with peak reflectivities of -37dB and -50dB, respectively. It is clear that the weaker FBGs (-50dB) have a lower signal-to-noise ratio. Figure 3.30 illustrates the reflection spectra of the 100 FBGs. The Bragg wavelengths of the 100 FBGs vary from 1546n to 1547.5nm.

Given the FBGs were written with the same phase mask and same parameters, the difference of their reflectivity and Bragg wavelengths can be explained from several aspects:

(1) Although two relays were used to fix the position of the fiber, there was still some strain remained in the fiber during the UV exposure. However, after all the FBGs were written in the whole fiber, the fiber was placed freely and the strain in the fiber was released. The Bragg wavelengths of those FBGs would thus shift to different values.

(2) The reflectivity of FBG is mainly determined by the photosensitivity of the fiber, the pulse power of the UV light and the number of pulses. The pulse power of the excimer laser changed from time to time, and thus the resulted FBGs had different reflectivities.

(3) There was a DC component in the UV field, which would shift the Bragg wavelength during the formation of FBG. The level of the DC component varied with the relative position of the fiber to the phase mask. So the uncertainty of the fiber position would cause the disparity of the Bragg wavelengths.

A spectrum correlation technique was used to demodulate the Bragg wavelength shift. According to the result of the data processing, the 13 dB fluctuation of peak reflectivity and 1.5 nm shift of Bragg wavelength are acceptable for the demodulation scheme, with a little sacrifice of the demodulation accuracy in the cases of even a poor signal-to-noise ratio.

In conclusion, this fabrication system provided an efficient method to fabricate a large number of weak FBGs with satisfactory quality.

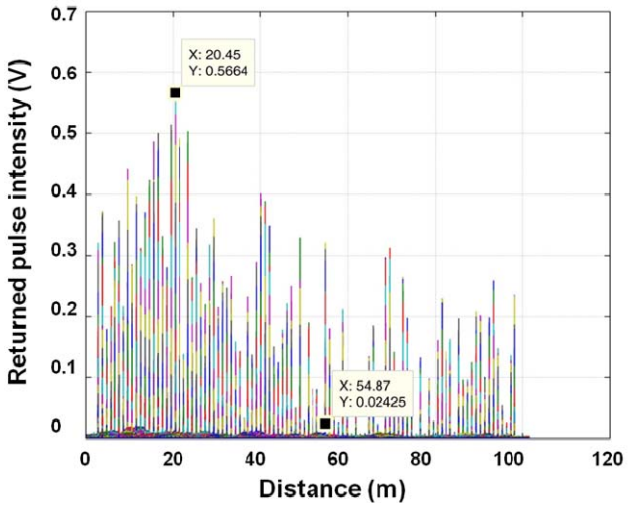

Figure 3.28 Returned pulses from the 100 FBGs

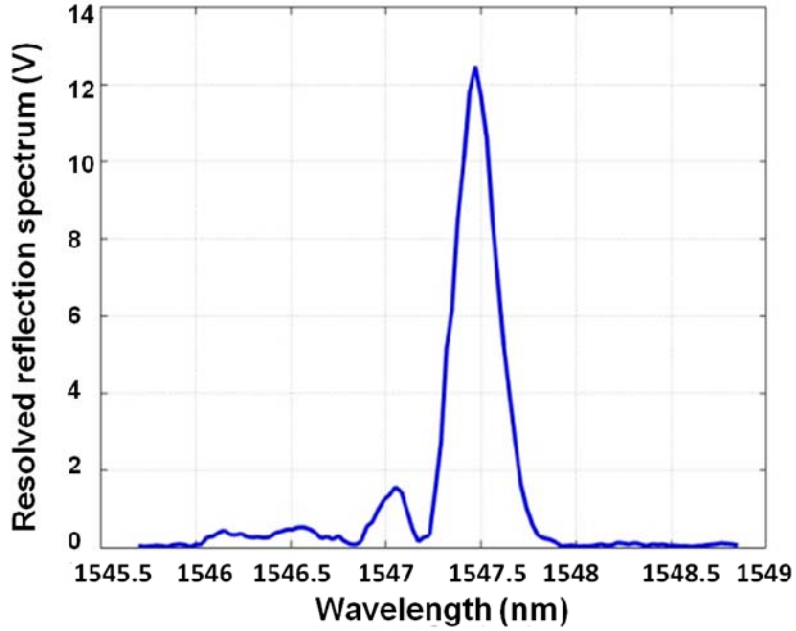

(a) R=-37dB

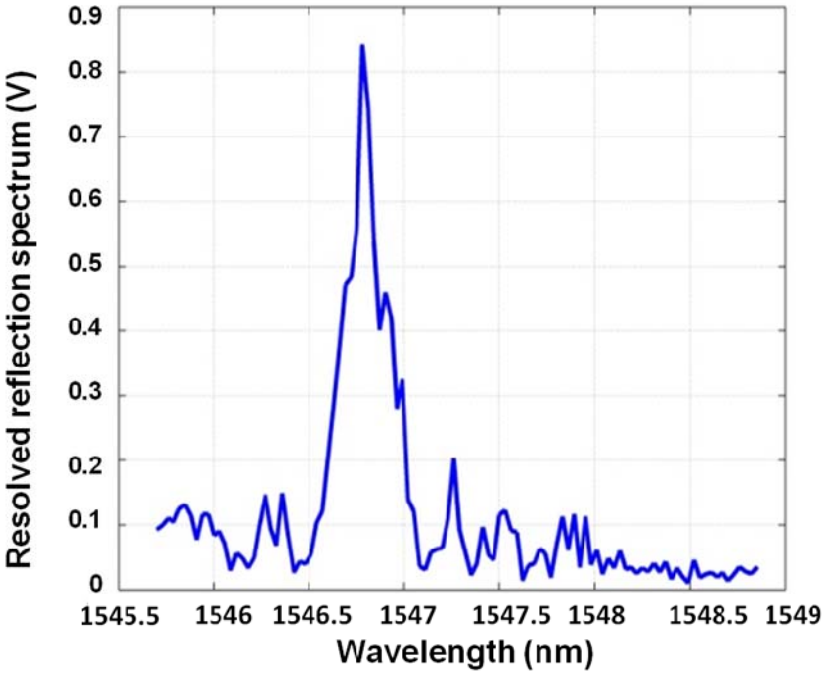

(b) R= -50dB

Figure 3.29 Resolved spectra of the FBGs with different peak reflectivities

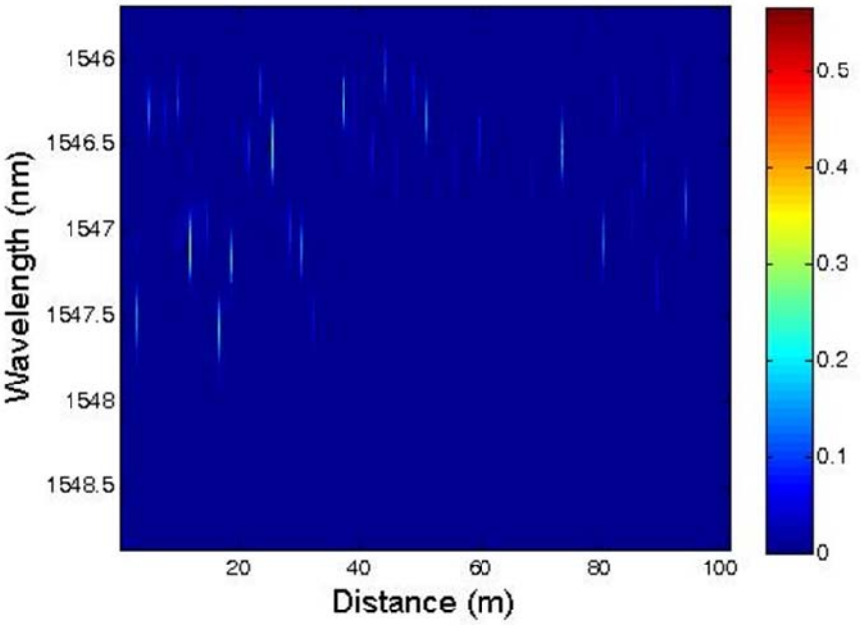

Figure 3.30 Pulse intensities at different wavelength of the 100 FBGs

Chapter 4 WSTDM interrogation system

In this chapter, a wave-scanning time-division multiplexed (TDM) interrogation system is presented. Different FBGs were resolved with different time delay, and the reflection spectrum of each FBG was obtained by scanning the wavelength of the source laser. Besides the demodulation of the ultra-weak FBGs network, this interrogation method could possibly be applied to dense multiplexing of some other types of sensors. The resolved spectra of the ultra-weak FBGs with different reflectivities were investigated, and the spectrum correlation algorithm was used to calculate the wavelength shift of the FBGs. With this method, the spectra of one thousand ultra-weak FBGs with 0.2m spatial resolution were successfully resolved and were further applied for demonstration of distributed temperature measurement.

4.1 System overview

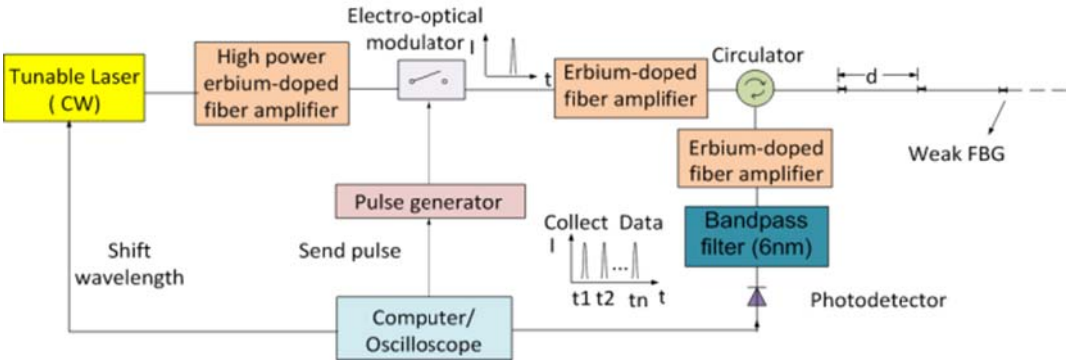

Figure 4.1 Interrogation system of a WSTDM sensor array

The interrogation system is illustrated in Figure 4.1. A tunable laser was pulsed modulated, and the reflected signals from the serially connected FBGs were detected with a high-speed photo detector. The locations of these FBGs were resolved by their different time delays, and the reflection spectrum of each FBG was obtained by scanning the wavelength of the laser. In the system, the CW light from the tunable laser (New Focus 6328) with a tuning range of 1510-1580 nm was first amplified and then modulated into nanosecond pulses by an electro-optic modulator (EOM). The pulses were launched into

the serial FBG array, and the reflected pulses from the FBGs were converted into an electrical signal by a high-speed photodetector (Thorlabs FPD310 1.8 GHz, 5×10^4V/W). Three Erbium-doped fiber amplifiers (EDFAs) were used to amplify the light power. A bandpass filter was placed in front of the photodetector to suppress the amplified spontaneous emission (ASE) noise introduced by the EDFAs. The serial data from the photodetector were collected by a high speed oscilloscope (LeCroy Wavepro7Zi) with an embedded computer, which also synchronously controlled the tunable laser and the pulse generator. The details of the system will be introduced in the following sections.

4.1.1 Pulse modulation

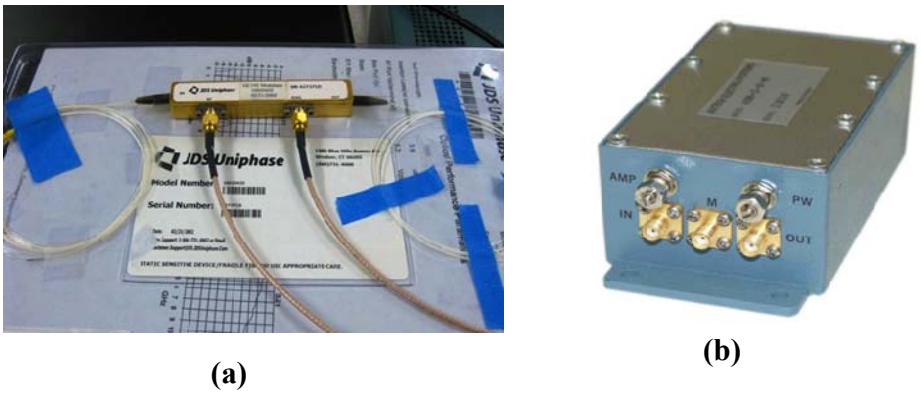

(a) (b)

Figure 4.2 (a) The Electro-optical modulator (b) The electrical pulse generator

The CW light from the tunable laser was modulated into nanosecond pulses by an EOM (JDS Uniphase Inc). The EOM was a Mach-Zehnder interferometer whose optical path difference (OPD) and hence transmission could be modulated via the linear electro-optic effect, or the Pockels effect by an applied electric field. The EOM was biased at 3.5v, and an external nanosecond pulse generator provided the RF modulation signal. The pulse width (Full width at half maximum) could be adjusted from 0.2-4ns and the output amplitude could be adjusted from 0-10V. The pulse repetition rate could be tuned from 0Hz to 1MHz by an external trigger signal, which was further controlled by a computer. Figure 4.3 shows the detected temporal profile of a 0.5ns pulsed light.

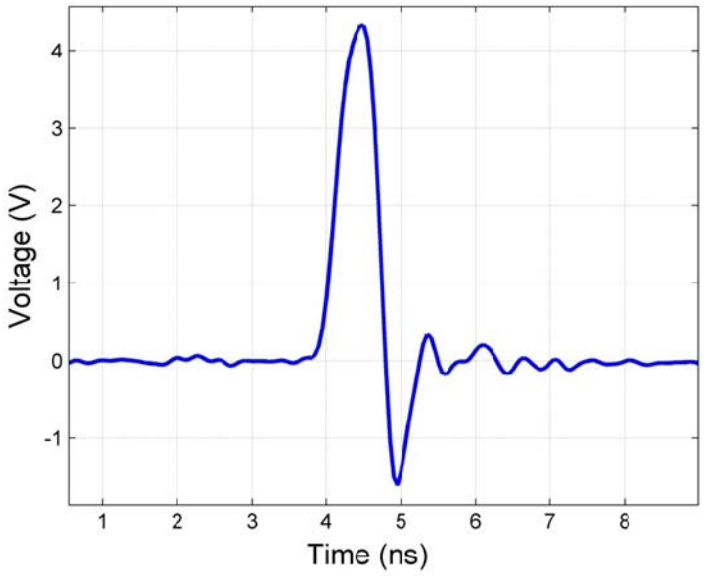

Figure 4.3 Temporal profile of a modulated 0.5ns pulsed light

4.1.2 Signal amplification

Three EDFAs were used in this system to improve the signal quality. A high power EDFA amplified the power out of the CW tunable laser, from 1 mW to about 200 mW; a low-noise EDFA compensated the 10dB insertion loss of the EOM and another low-noise EDFA amplified the weak light reflected back from the FBGs.

As shown in figure 4.4, if the combined gain of the EDFAs was too high, the returned light signal could saturate the photo detector, broaden the detected pulse and degrade the spatial resolution. So the gains of the EDFAs were carefully selected to be about 23 dB, 10 dB and 13 dB, respectively.

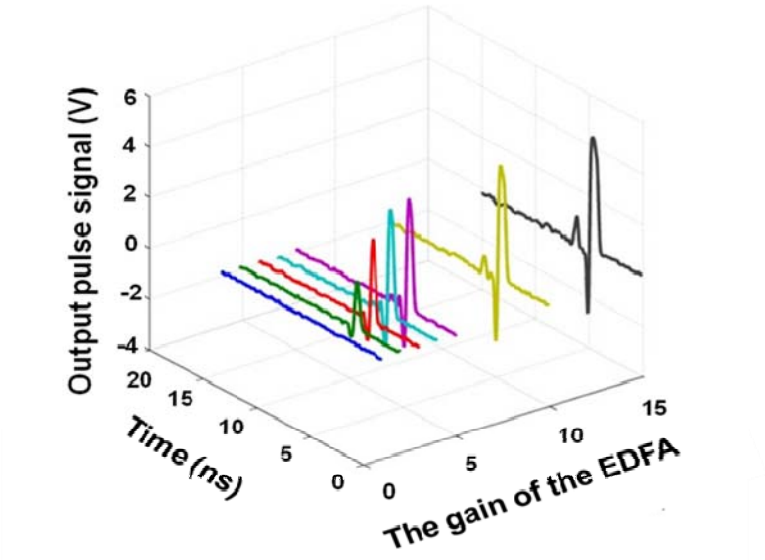

Figure 4.4 Saturation of photo detector when optical gain is too high

The peak reflectivity of the ultra-weak FBGs in the sensor array was around -40dB; if only considering the -3d loss induced by the circulator, the optical power of the returned pulses could be around -30dBm. For 1GHz signal, the minimum detectable power of the photodetector was -33dBm. In practice, the optical connectors in the interrogation system and the splicing points in the sensor network could induce extra optical losses. Therefore, the returned signal was possible to be buried in the noise. To increase the signal-to-noise ratio (SNR), another normal EDFA with 23dB maximum gain was used before the photodetector to amplify the weak optical signal from the sensor array. The EDFA will generate some noise while amplifying the input signal. The dominant noise is the amplified spontaneous emission (ASE). The origin of this is the spontaneous recombination of electrons and holes in the amplifier medium [82]. This recombination gives rise to a broad spectral background of photons that get amplified along with the input optical signal. The output signal with the ASE noise is given in figure 4.5 a. To suppress the ASE noise, one tunable bandpass filter was applied after the second EDFA. Considering the dynamic wavelength range for the temperature measurement, the bandwidth of the filter was set to 6nm centered at the Bragg wavelength of the FBGs. The output signal with the suppressed ASE signal is given in figure 4.5.b. For the EDFAs placed before the FBG sensor array, no bandpass filters were used because the FBG

sensors, which only reflected the light at a specific wavelength, can automatically filter the ASE noise.

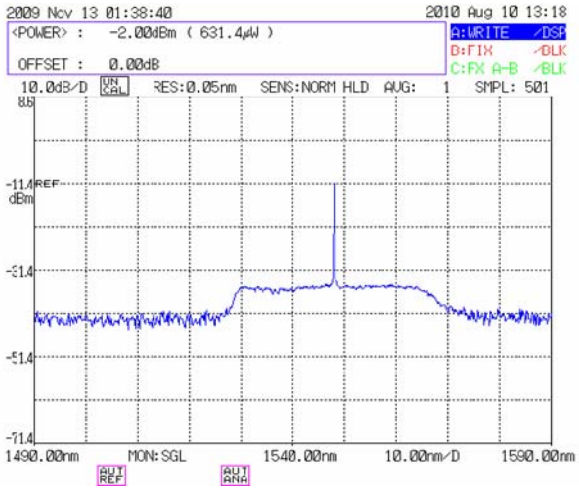

(a)

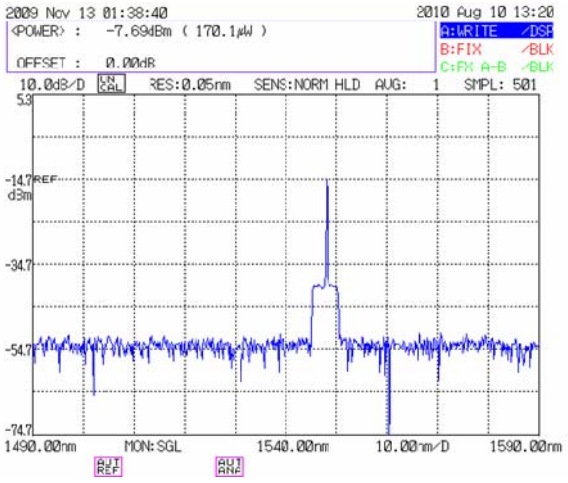

(b)

Figure 4.5 (a) The output signal with the associated amplified-spontaneous – emission (ASE) noise (b) The output signal with the suppressed ASE noise

4.1.3 System timing and trigger signals

The interrogation system employed the wave-scanning TMD method to realize the dense sensor multiplexing. Figure 4.6 illustrates the relationship of the input signal and the output signal in the time domain. First, the output light of the tunable laser was set at a single wavelength. After the modulation by the EOM, a pulse with a period of w was

generated and launched into the sensor array. In response to one input pulse, a train of pulses returned from the different FBGs in the sensor array. At each wavelength, 100 input pulses were serially launched to the sensor array and the 100 corresponding trains of returned signals were averaged to enhance the system SNR. The period of the input pulse (10*w* μs, w is an integer and defines the pulse width as shown in figure 4.6) was twice of the time (5*w* μs) for collecting a train of returned signals. So there was no overlap between the returned signals from the two neighboring input signals. After the 100 periods (1000*w* μs), the tunable laser was shifted to the next wavelength, and the whole process would be repeated until the wavelength scanning was finished. The returned pulses were converted into electric signals by the photodetector and collected by the oscilloscope.

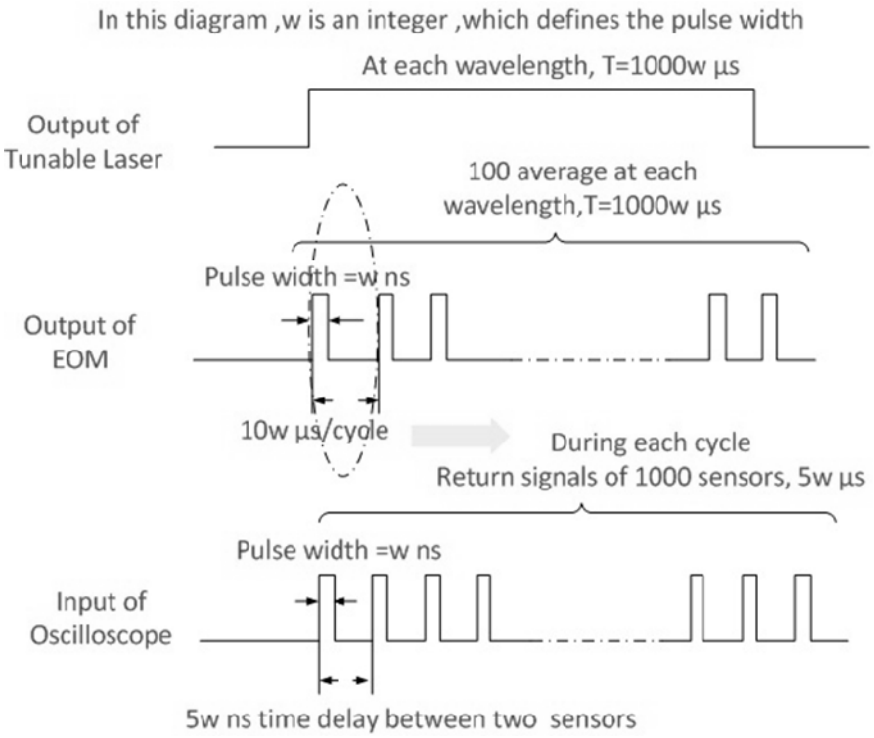

Figure 4.6 Timing of the system

The trigger signal was produced by a built-in computer in the oscilloscope. The trigger determined when to sample the reflected light signal, and should be extremely stable for high spatial resolution. Otherwise, the averaged waveform would be distorted as shown

in figure 4.7. In the interrogation system, two signals were considered to serve as the trigger signal: the output signal from the oscilloscope, which also served as the driven signal of the pulse generator; and the pulse signal from the pulse generator as shown in figure 4.8. Both the signals had the same repetition rate, which determined the period of the input pulse and was adjustable through the oscilloscope. The output signal from the oscilloscope was a square wave with the multiple interference noise on the top of the signal, which was caused by the impedance mismatch of the T-connector used to split the output signal into the trigger signal and the driven signal. Because of the noise, the jitter of this signal could delay the position of the trigger level by several nanoseconds, on the same order of the returning pulse signal (1ns pulse width). Thus, the returning signal would be wrongly determined and miscalculated in the signal average. The pulse signal from the pulse generator was narrow and clear. For the edge triggering, the jitter of this signal was much smaller than the returning pulse signal. Thus, the pulse signal from the pulse generator was used as the trigger signal in the interrogation system.

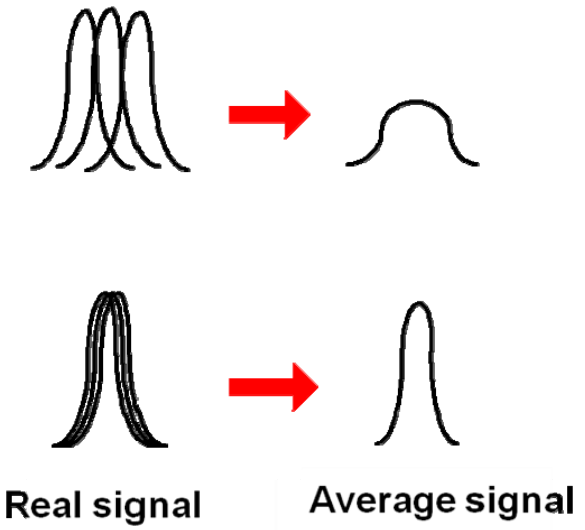

Figure 4.7 Distortion of averaged signal induced by the unstable trigger

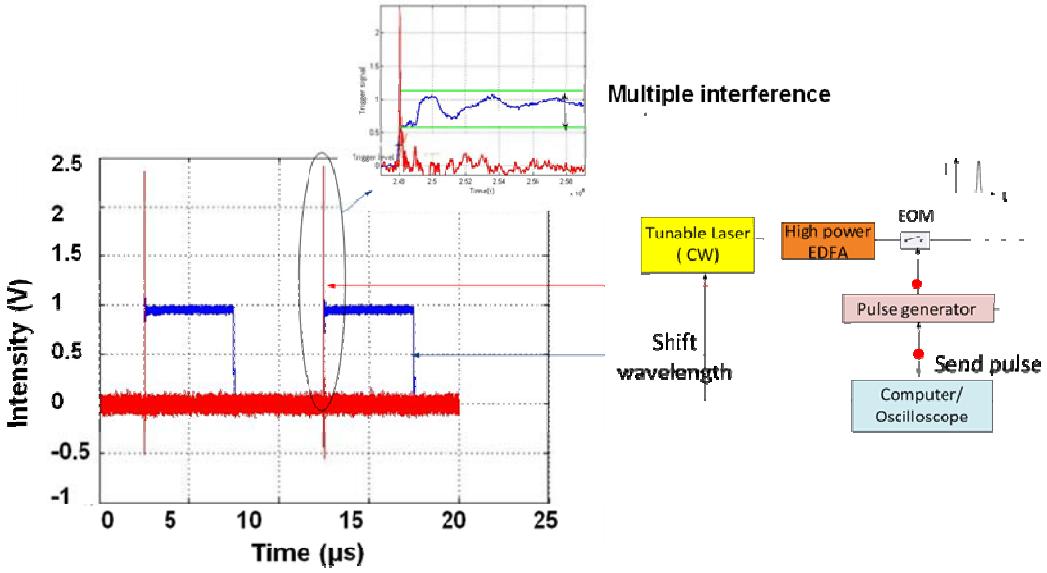

Figure 4.8 Two possible trigger signals of the interrogation system

4.1.4 Software implementation

Advanced computer software was developed to synchronize the whole interrogation system. The program was implemented in MATLAB on the embedded computer of the high speed oscilloscope. A block diagram of the program is shown in figure 4.9. The tunable laser communicated with the embedded computer through a USB-GPIB cable. The trigger signal was controlled by the output signal of the oscilloscope and monitored by input channel 3. The returning signals from the sensor array were collected by input channel 2 and calculated by the math channels. The program details were introduced in the following sections:

Initialization

The hardware initialization included the initialization of the tunable laser and the oscilloscope. The important parameters of the tunable laser, which were stored in the program, would be transferred to the tunable laser in the initialization process, including the wavelength scanning range, the step of scanning and the output power of the laser. Matlab installed in the embedded computer interacted with the oscilloscope by X-stream

COM object programming. In the initiation step, the parameters of the oscilloscope would be configured, including the repetition rate of the output signal, the sampling resolution of the input channels, the average times of the input channel, the trigger level and the trigger mode.

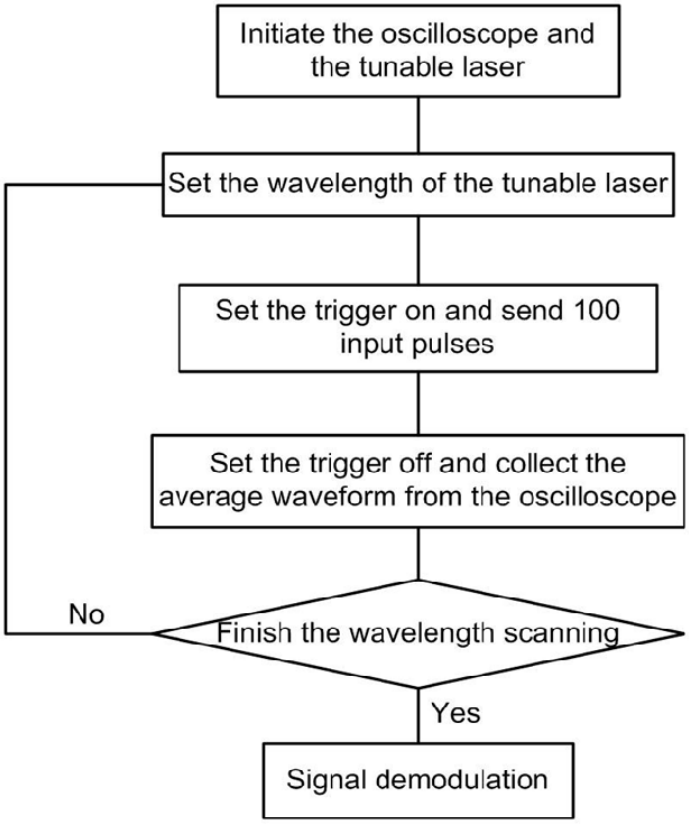

Figure 4.9 The program diagram of interrogation system

Trigger control and data collection

At a single wavelength, the output signal of the oscilloscope, which was a square wave with the preset repetition rate, was turned on to drive the pulse generator. The pulse signal from the pulse generator served as not only the RF signal to the EOM but also the trigger signal of the whole interrogation system. The real-time returned signals from the sensor array were collected by channel 2 and displayed on the screen of the oscilloscope. After 100 periods, the output signal of the oscilloscope was turned off and the return signals were averaged and saved in memory of the math channel. Subsequently the embedded computer cleared the memory of the math and transferred the data in memory

to the workshop of the Matlab for further demodulation. At each wavelength, the whole process was repeated until the wavelength scanning was finished.

Wavelength tuning

The tunable laser worked in the remote control mode and could be accessed by the GPIB interface. The linewidth of the tunable laser output light was less than 300 kHz, and the tuning range was 1510-1580 nm. The command from the embedded computer asked the laser to tune the output wavelength at the preconfigured wavelength step.

FBG decoding

To test the performance of the interrogation system, the reflection spectrum of a single FBG with different reflectivities was reconstructed and investigated with the setup illustrated in figure 4.10. An FBG with -35dB peak reflectivity was connected to the interrogation system by a circulator, and a variable optical attenuator (VOA) was placed before the FBG. The FBG with different reflectivities could be simulated by changing the attenuation value. It should be noted that the attenuation value set by the VOA corresponded to twice loss to the reflectivity of the FBG because the pulse traveled roundtrip. Figure 4.11 (a) shows a resolved spectrum of the FBG with this interrogation system. Gradually decreasing the strength of the FBG also reduces the SNR of the resolved spectra. The minimum resolvable reflectivity is -57dB as shown in figure 4.11 (b).

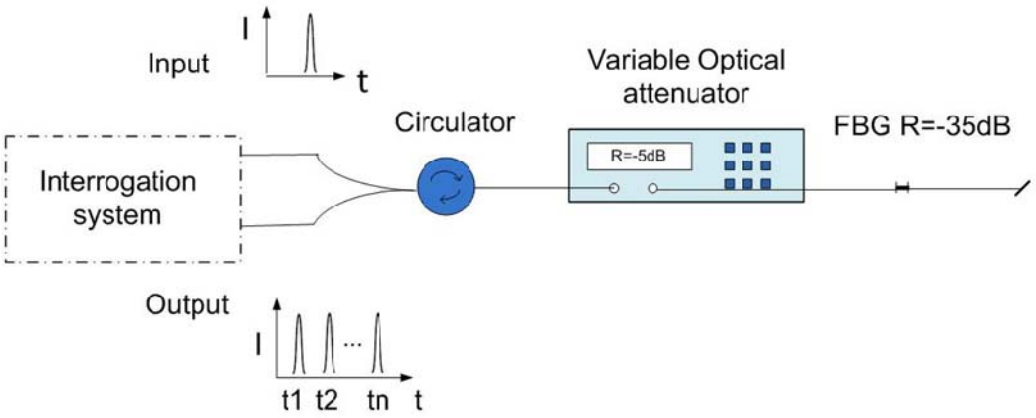

Figure 4.10 Decoding a single FBG with the interrogation system

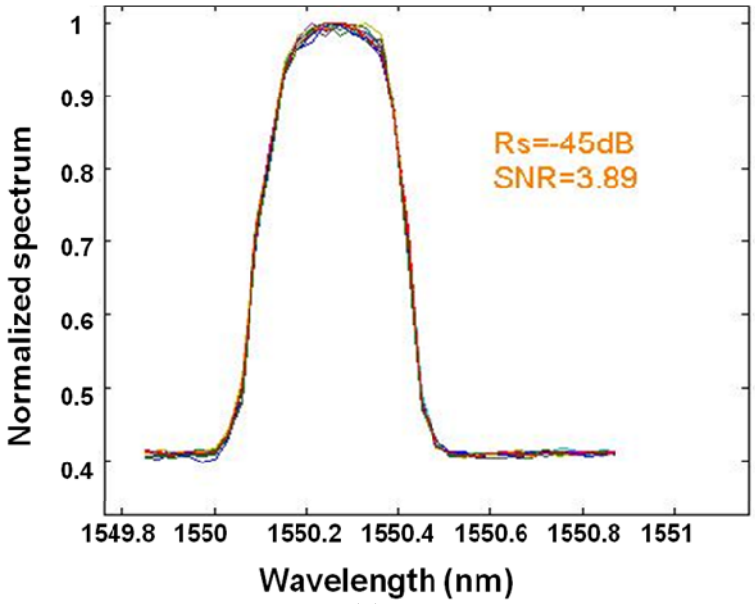

(a)

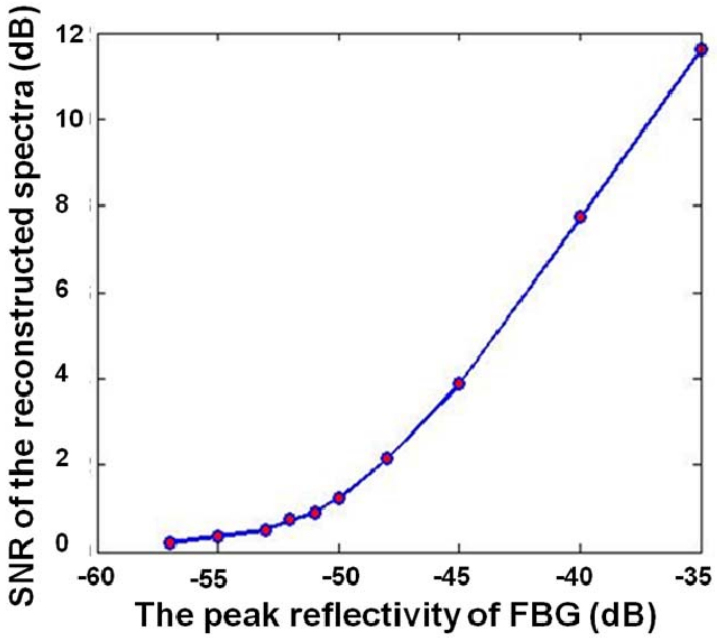

(b)

Figure 4.11 (a) The resolved spectrum of an FBG (b) The SNR of the resolved spectra as a function of the reflectivity of the FBGs

4.2 Signal demodulation

4.2.1 Pulse location and pulse measurement

The returned waveform was stored in a *m*x*n* two-dimensional matrix *A* as shown in figure 4.12 (a): one dimension is the wavelength domain (row) with ***m*** different wavelengths and the other dimension is the time domain (column) with *n* different time delays. In the time domain, the returned waveform was a train of pulses corresponding to the strength of the different FBGs in the sensor array. The time delay between the pulses was determined by the distance between two neighboring FBGs as described in equation 2.17. The separation distance was designed and fabricated to be around 1 meter. However in practice, the actual separation distance would be affected by several factors such as the fiber displacement accuracy in the fabrication, the splicing point between the fibers, and the excluded FBGs, which could not be used due to low SNR. As a result, the actual pulse delays in the system did not match the estimated time domain values. An algorithm was developed to find the pulse position automatically as described.

1. Simplify the A matrix to a *1*x*n* one-dimensional matrix *B* in the time domain by summing the values in the wavelength domain.

$$B_i = \sum_{j=1}^{m} A_{ji} \quad 1 \le i \le n,\ 1 \le j \le m \qquad (4.1)$$

2. Find the peak positions of matrix *B*. To distinguish the peaks of the pulse signals from the noise, some parameters are carefully defined, including the minimum peak value and the minimum delay time between the two neighboring peaks. The peak positions will be saved in matrix *C,* and the number of peaks defines the number of useful FBGs in the sensor network.

3. For 40GS/s sampling rate, a 1 ns pulse corresponds to 40 sampling points in the time domain. Assuming the peak is approximately at the center of the pulse, 80 data points near the peak are sufficient to capture the entire returning pulse signal.

With this method, the minimum peak value was used to exclude the FBGs with poor SNR and the returned pulses from different FBGs could be accurately located.

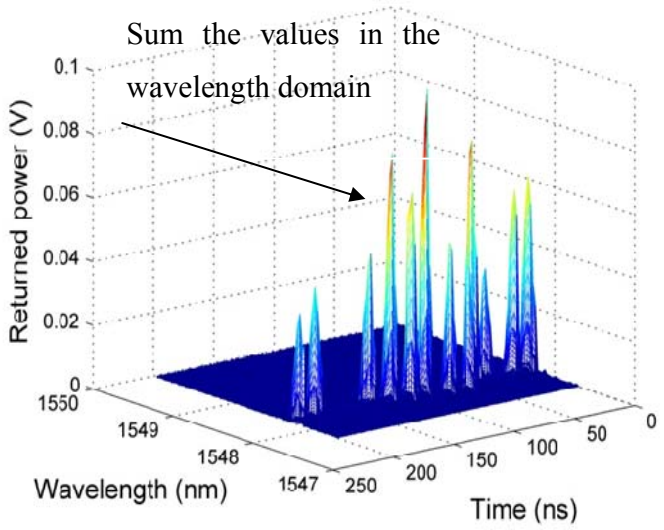

(a) The returned waveform in two dimensions

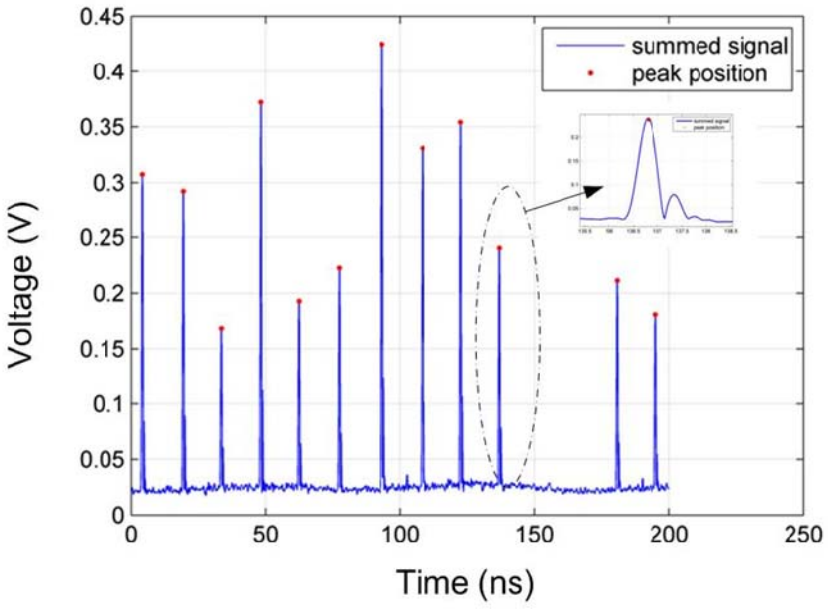

(b) The summed signal in the time domain

Figure 4.12 Illustration of the peak location method

In this measurement, the details of a pulse shape were important. Pulses became distorted after the EOM modulation and EDFA amplification. To eliminate the effects of pulse

distortion, the pulse area was used to measure the returning power of the FBGs. At the j^{th} wavelength, the pulse area of the pulse returned from the k^{th} FBG is defined as

$$P_{j,k} = \sum_{i=C_k-\frac{l}{2}}^{C_k+\frac{l}{2}} \left| A_{j,i} \right| \qquad 1 \le j \le m, 1 \le k \le n \tag{4.2}$$

where l is the sampling length of one pulse, C_k is the position of the k^{th} pulse, and n is the number of the useful FBGs. Figure 4.13 shows the pulse area of a single pulse.

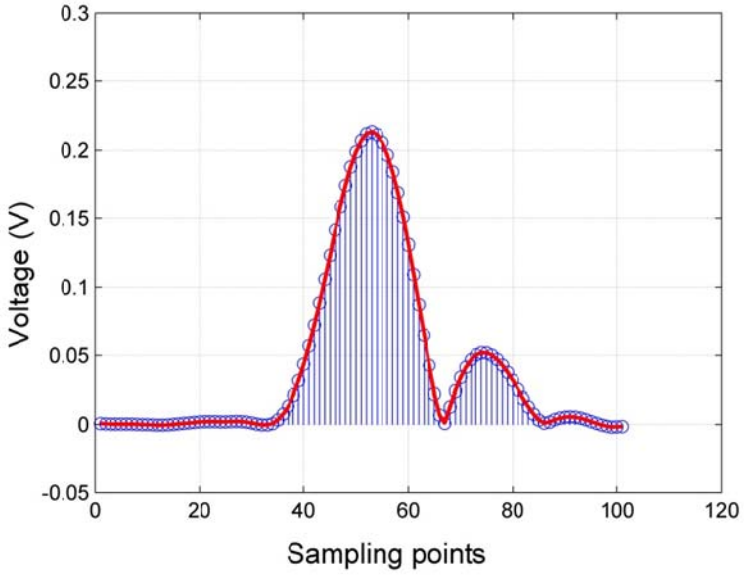

Figure 4.13 Pulse area measurement

4.2 .2 Spectrum reconstruction

The reflective spectrum R_k of the k^{th} FBG can be reconstructed based on the returning power at the different wavelengths $P_{j,k.}$

$$R_k = [P_{1k}, P_{2k}, P_{3k} \cdots P_{mk}] \tag{4.3}$$

where m is the sampling number in the wavelength domain. Figure 4.14 shows the resolved spectra of 12 FBGs. This figure indicates that the spectra of the FBGs in the sensor array can be successfully resolved with this demodulation method.

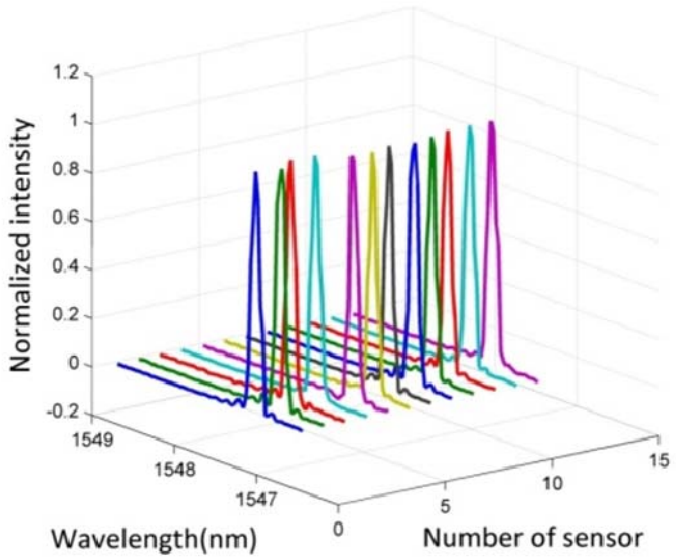

Figure 4.14 Normalized spectra of 12 FBGs

Spectrum correlation

When a strain or temperature variation is applied to an FBG, the effective refractive index n and the grating period Λ is changed, which results in a shift of the Bragg wavelength. Therefore FBGs can be used as a sensor to measure temperature or strain. The wavelength shift detection scheme directly affects the accuracy of the measurement. In practice, when a measurand is applied, not only the wavelength of the FBG will shift but also the peak intensity may change as well. However, the spectra shape remains approximately the same. Based on this characteristic, spectrum correlation technique was adopted to calculate the wavelength shift by calculating the cross correlation between the original and shifted spectra.

Consider two spectra $S_1(j)$ and $S_2(j)$, where $j=1,2\ ....N$, represent the sampling number in the wavelength domain. Their correlation is defined as [83]:

$$R_{s1,s2}(l) = \frac{\sum_{j=1}^{N}[S_1(j-l)-\overline{S_1}][S_2(j)-\overline{S_2}]}{\sqrt{\sum_{j=1}^{N}[S_1(j-l)-\overline{S_1}]^2}\sqrt{\sum_{j=1}^{N}[S_2(j)-\overline{S_2}]^2}} \tag{4.4}$$

where l represents a wavelength shift to spectrum S_1, $\overline{S_1}$ and $\overline{S_2}$ are the means of the spectra $S_1(j)$ and $S_2(j)$. When the wavelength index $(j-l)$ exceeds the range [1, N], we round shift the spectra by setting

$$S_1(j-l) = \begin{cases} S_1(j-l+N) & (j-l) < 1 \\ S_1(j-l-N) & (j-l) > N \end{cases} \tag{4.5}$$

In the ideal case, if S_1 and S_2 have exactly the same spectra shape with a relative wavelength shift M, the correlation between S_1 an S_2 will have a maximum value when $l=M$. Here S_2 and S_1 are assumed to be the spectra of a particular FBG with and without the applied measurand. We calculate the cross correlation $R_{s1,s2}(l)$ with l scanning from -N to N, then the shift value $l=l_{max}$, which results in the maximum $R_{s1,s2,}$ is regarded as the wavelength shift between the two spectra. The accuracy of spectrum correlation technique mainly depends on the sampling number (N) in the wavelength domain and the SNR of the spectrum [83].

In practice, the resolved spectrum needs the normalization and the interpolation before the spectrum correlation. The normalized spectrum is obtained by dividing the resolved spectrum of each FBG by its peak value.

$$R_{nor}(\lambda) = \frac{R_{resolved}(\lambda)}{R_{\max}} \tag{4.6}$$

The normalized spectra of all the FBGs were rescaled to the same value range from 0 to 1, which minimized the effect of intensity instability. Subsequently linear interpolation was applied to increase the sampling number in the wavelength domain. The sampling wavelength of the original spectrum was limited by the wavelength scanning step of the tunable laser. Assume (R_1,λ_1) and (R_2,λ_2) represent the two data points of the original spectrum, the linear interpolation is given by

$$R = R_1 + (R_2 - R_1)\frac{(\lambda - \lambda_a)}{(\lambda_b - \lambda_a)} \tag{4.7}$$

where *(R,λ)* is the data point of the interpolated spectrum. The preset wavelength resolution of the tunable laser was 0.03nm. After the linear interpolation, the wavelength resolution can be improved to 1pm, which is sufficient for the temperature measurement.

With the same sampling number in the wavelength domain, the accuracy of the calculated wavelength shift is determined by the SNR of the resolved spectrum. The accuracy can be represented by the average wavelength shift of many time measurements. The spectra of the FBGs with different SNR were measured 50 times under the same environment. Figure 4.15 shows the average wavelength shift of the resolved spectra with the different SNR. According to the figure, the spectrum with a lower SNR corresponds to a larger measurement error.

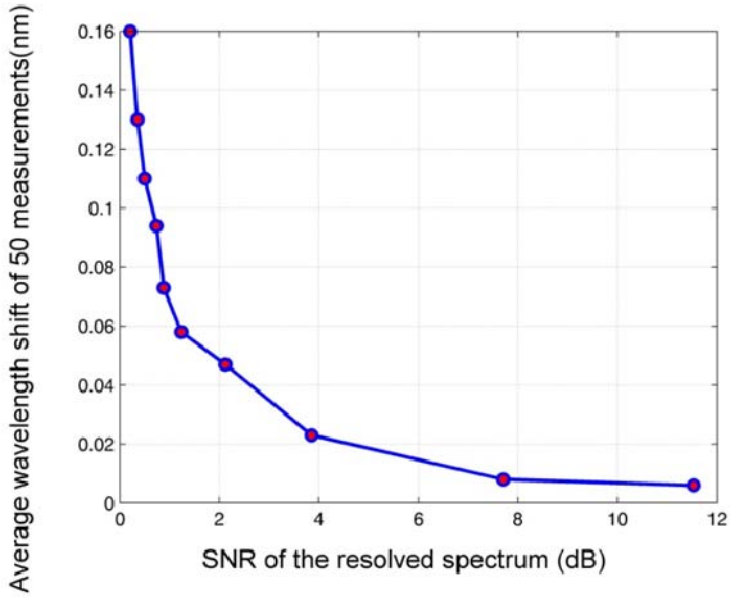

Figure 4.15 The average wavelength shifts of the resolved spectra with different SNR

4.3 Experimental Results

The FBG sensor network can be used to measure temperature and strain after calibration. This section provides the lab experiment results of the sensor system for temperature measurement.

4.3.1 Performance of the 1000-FBG sensor network

One thousand ultra-weak FBGs were written on a single optical fiber successfully with approximately 1 meter separation distance. The peak reflectivities of the FBGs ranged from -37 dB to -50 dB. For the glass fiber used, 1ns pulse width corresponded to a spatial resolution of 0.2 m. The source wavelength was scanned from 1545.70 nm to 1548.9 nm with a 0.03 nm resolution and the reflection spectrum of each sensor was reconstructed from the returned pulses trains.

The measurement accuracy is the difference between the wavelength shift measured by the FBG and the actual wavelength shift. The measurement was repeated 20 times under the same condition. For the same condition, the actual wavelength shift is 0nm, so the average measured wavelength shift can be used to represent the accuracy of the measurement. Figure 4.16 shows the average wavelength shift of the 1000 FBGs. The result shows 0.5% sensors have more than 0.05nm wavelength shifts; 18% sensors have 0.02~0.05nm wavelength shift; and 81.5% sensors have less than 0.02nm wavelength shifts. The different accuracies of the sensors in the network are mainly caused by the different peak reflectivities and hence different signal-to-noise ratios.

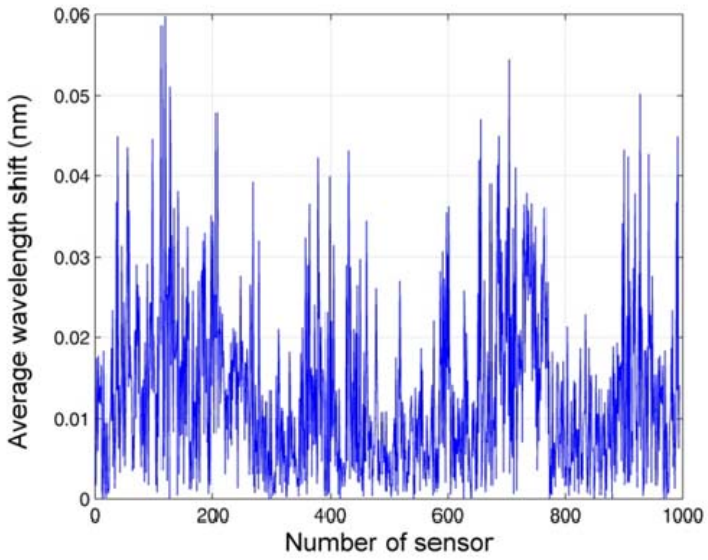

Figure 4.16 The average wavelength shifts of the 1000 FBGs

The precision of the measurement, also called repeatability, is the difference between the different measurements when the experiment process is repeated under the same condition. Based on the results of 20 measurements, the standard deviation (STD) of the wavelength shift was calculated to obtain the precision. Figure 4.17 shows the STD of the wavelength shift: 2% sensors have more than 0.05nm STD; 40.8% sensors have 0.02~0.05nm STD; and 57.2% sensors have less than 0.02nm STD. The precision of the measurement is mainly affected by the average times of the measurement.

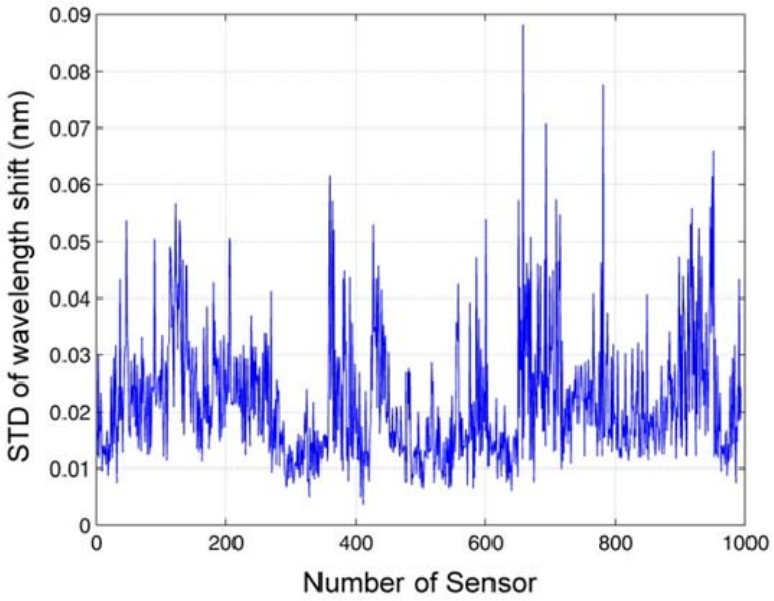

Figure 4.17 The standard deviation (STD) of wavelength shift

To estimate the real transmission loss of the sensors, we launched pulses from the two ends of the same sensor array and compared the returned power from the sensors. For a 500-sensor array, the roundtrip loss was -0.96dB, slightly larger than the simulation result for the -40dB FBGs (-0.88dB), which was mainly caused by the splicing loss. Figure 4.18 gives the actual returned pulses from the two ends of the same sensor array. The different colors represent the pulses at the different wavelength.

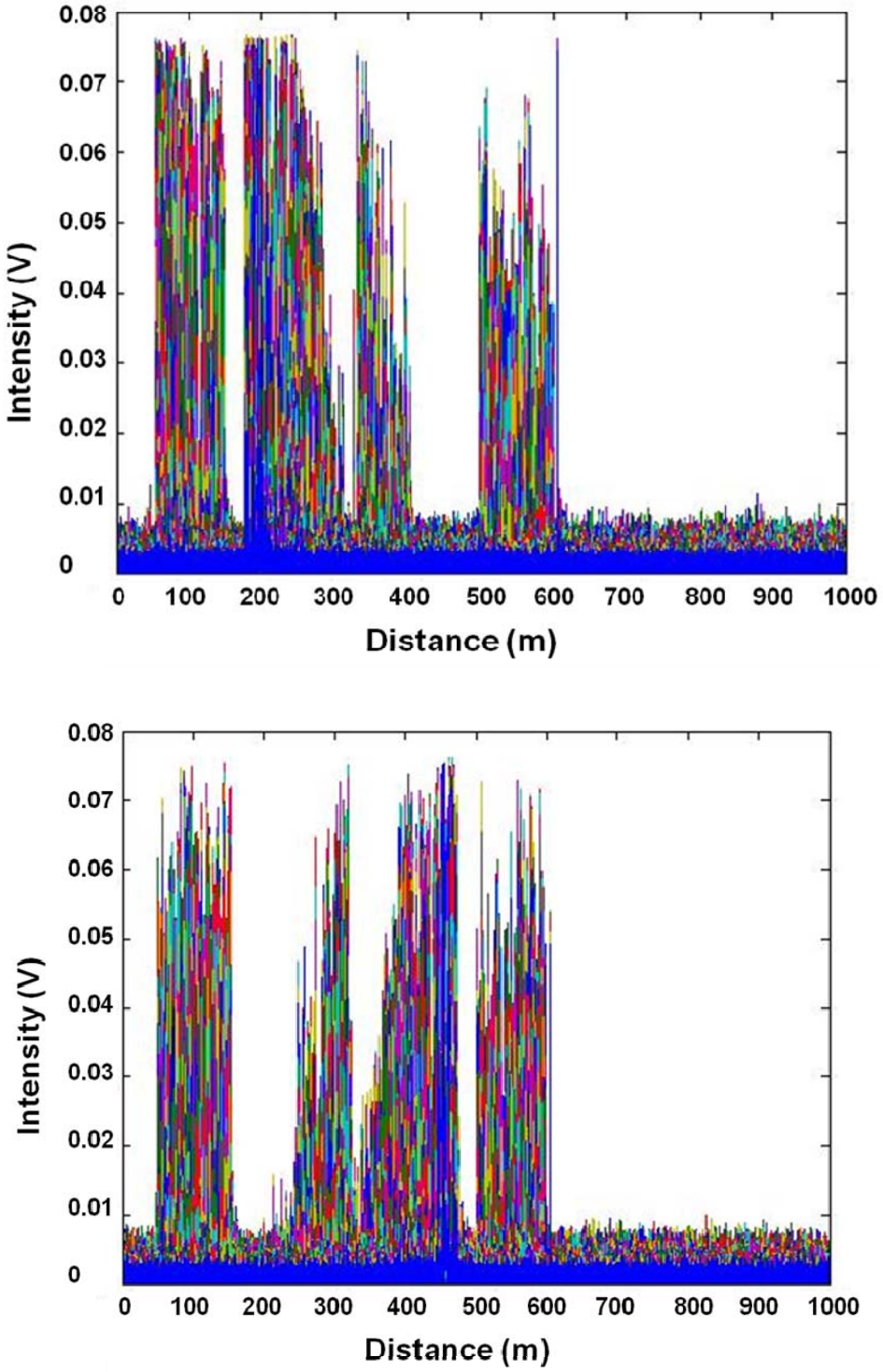

Figure 4.18 The returned pulses from the two ends of the same sensor array

As introduced earlier, the crosstalk and the transmission loss can cause the spectra

distortion of the FBGs at the far end of the sensor array, including the returned power decrease and the bandwidth broadening. According to the simulation results in chapter 4, the ultra-weak FBGs as used this experiment should have negligible distortion. Because the strengths of the fabricated FBGs are not exactly identical as assumed in the simulation, it is difficult to estimate the distortion effects by comparing the returned power. Thus, to confirm the simulation results, the bandwidths were investigated by comparing the resolved spectra of the FBGs at different locations. The normalized spectra of the 10^{th} FBG and the 870^{th} FBGs are given in Figure 4.19. It is seen that there is no observable bandwidth broadening effect. The experiment results confirm the previous analysis about the transmission loss and the crosstalk of the ultra-weak FBGs.

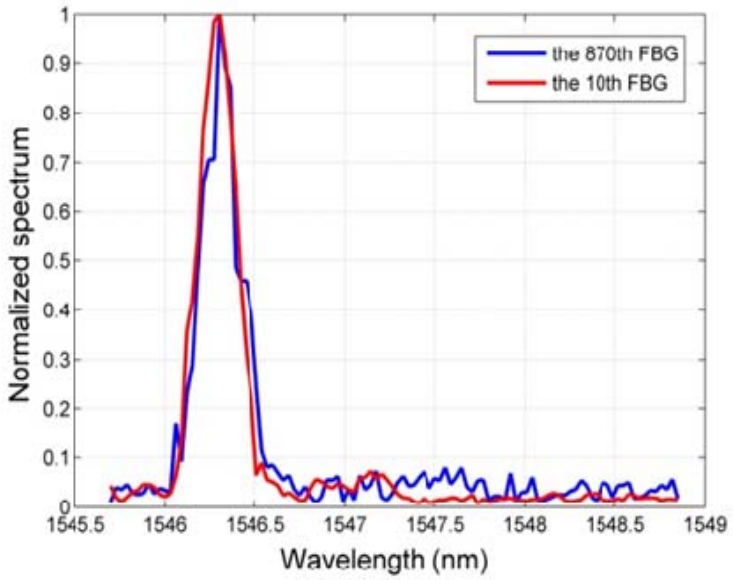

Figure 4.19 The reconstructed spectra of the 10th and the 870th FBGs

4.3.2 Temperature sensing test

The principle of temperature measurement is based on the thermal-optic effect and the thermal expansion of optical fiber. The thermal-optic effect describes the change in refractive index; the thermal expansion describes the physical length expansion of the grating period. The change of the Bragg wavelength of an FBG due to temperature variation can be approximately described by [69]

$$\frac{\Delta\lambda}{\lambda_0} = \alpha * \Delta T = (\alpha_n + \alpha_\Lambda) * \Delta T \tag{4.8}$$

where $\Delta\lambda$ is the wavelength shift, λ_0 is the initial wavelength, α_n is the thermo-optic coefficient and α_Λ is the thermal expansion coefficient. The wavelength shift has a linear relationship with the temperature change, which can be derived from equation 4.8 as

$$\frac{\Delta\lambda}{\Delta T} = \lambda_0 * (\alpha_n + \alpha_\Lambda) = \alpha \tag{4.9}$$

where α defines the temperature sensitivity of the FBG.

In the experiment, four sections of the sensor array, which contain 17 FBGs total, were heated in a temperature chamber (TestEquity 1000) as shown in figure 4.20. The chamber had a temperature range from -35°C to 175°C with the typical 0.2 °C control tolerance. The actual temperature inside the chamber could be read from the front panel with 0.1°C display resolution. The temperature was increased from 35°C to 135°C at a step of 10°C. At each step, the temperature was held 1 hour to reach a stable condition, and the measurement was repeated 3 times at each temperature. Figure 4.21 shows the temperature measurement results of the 1000-FBG array. In the heated region, the Bragg wavelengths of the FBGs shifted; in the unheated region, no significant wavelength shift took place.

Figure 4.20 The experiment setup of the temperature measurement

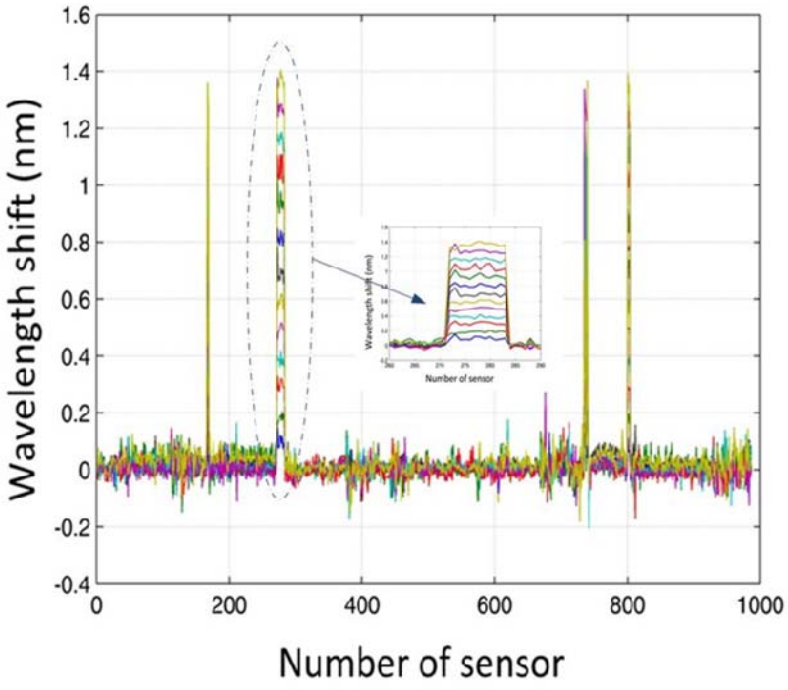

Figure 4.21 Temperature measurement results of the 1000-FBG sensor array

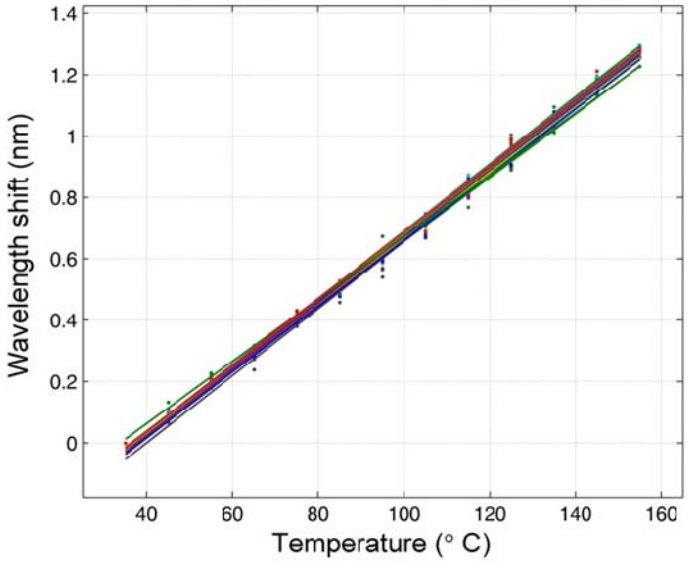

Figure 4.22 the wavelength shift versus the temperature change

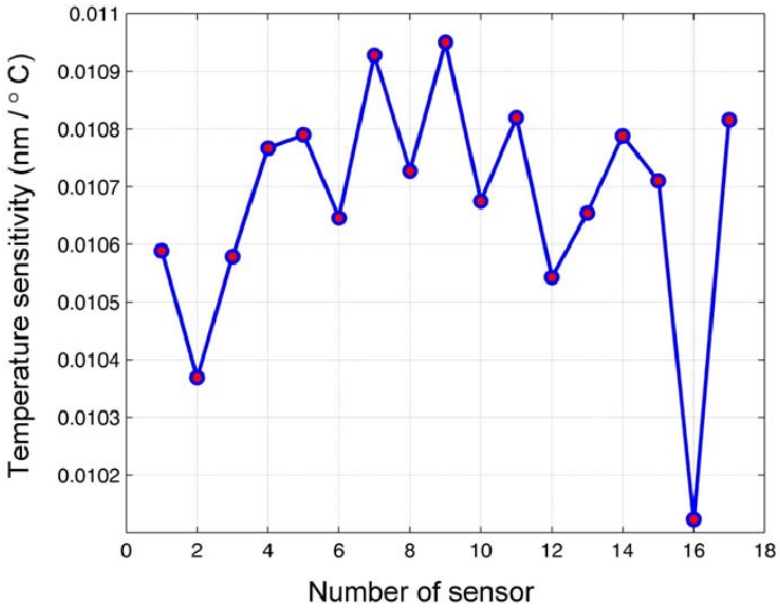

Figure 4.23 The temperature sensitivity of 17 FBGs

Figure 4.22 shows the wavelength shifts of the 17 FBGs versus temperature. They show a linear relationship as described in equation 4.9. The temperature sensitivity α of each FBG was calculated by linear curve-fitting. The fitted coefficient varies from 10.1 to

10.9pm/°C as shown in figure 4.23. To measure the differences between the fitted values and the actual values, the root mean square deviation (*Rmsd*) is defined as

$$Rmsd(A_1, A_2) = \sqrt{\frac{\sum_{i=1}^{n} (a_{1,i} - a_{2,i})^2}{n}} \tag{4.10}$$

Where A_1 and A_2 represent the actual value and the fitted value respectively, n is the number of values. The *Rmsd* can be considered as a measure of the accuracy of the sensor: the sensor with a high accuracy leads to a good linearity between the wavelength shift and the temperature, which corresponds to a small *Rmsd.* Form the figure, the 6^{th} FBG has a high accuracy, and the 7^{th} FBG has a low accuracy. As discussed earlier, the accuracy of the FBG relates to the SNR of the resolved spectra. The fitting curves and the resolved spectra of the 6^{th} and 7^{th} FBGs are given in figure 4.25 and figure 4.26. These figures indicate that the experiment results show an agreement with the previous analysis.

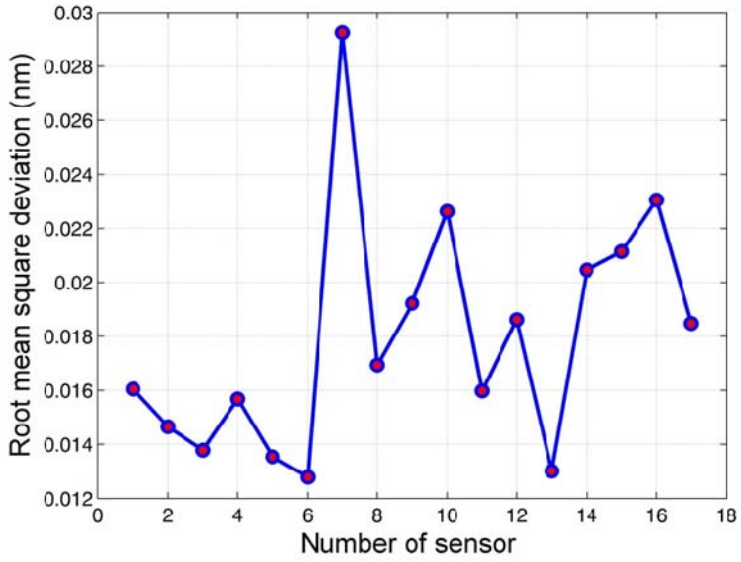

Figure 4.24 The Rmsd of the 17 FBGs

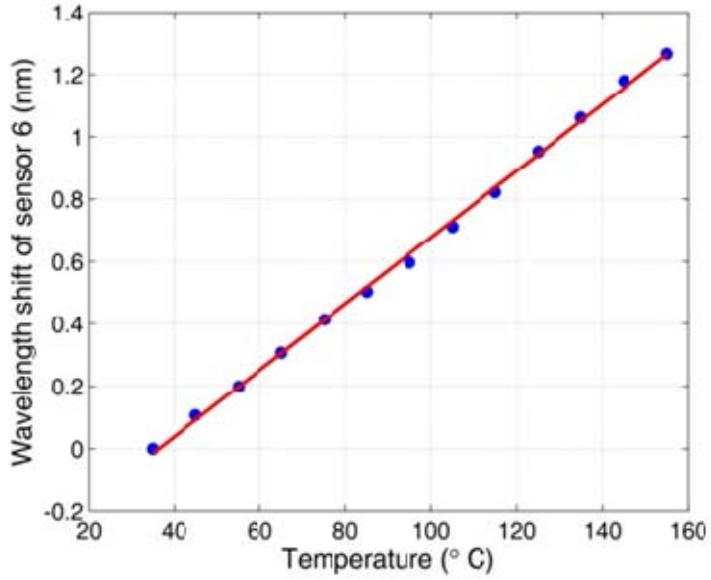

(a)

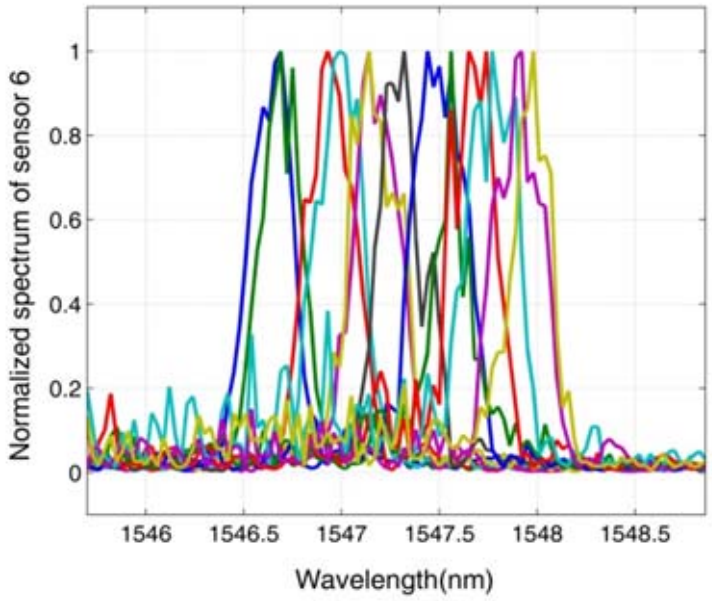

(b)

Figure 4.25 Information of 6th FBG (a) Fitted curve of shift wavelength (b) Reconstructed spectra

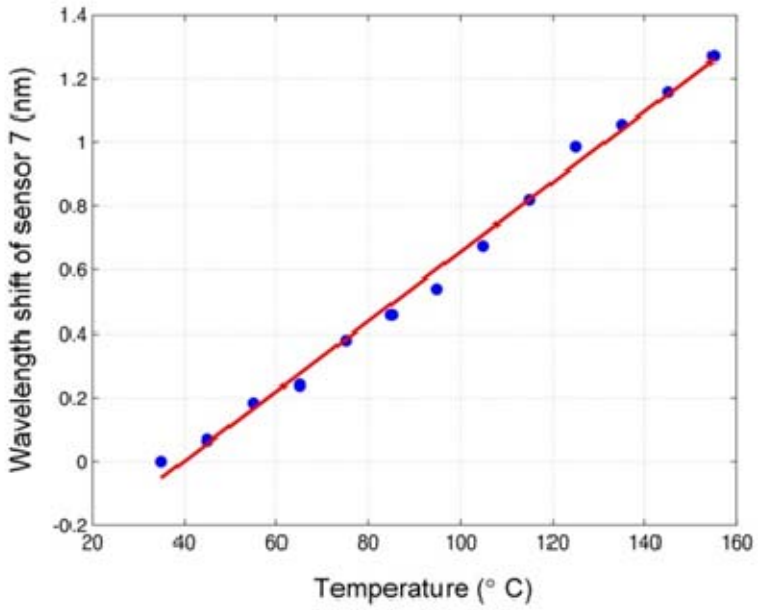

(a)

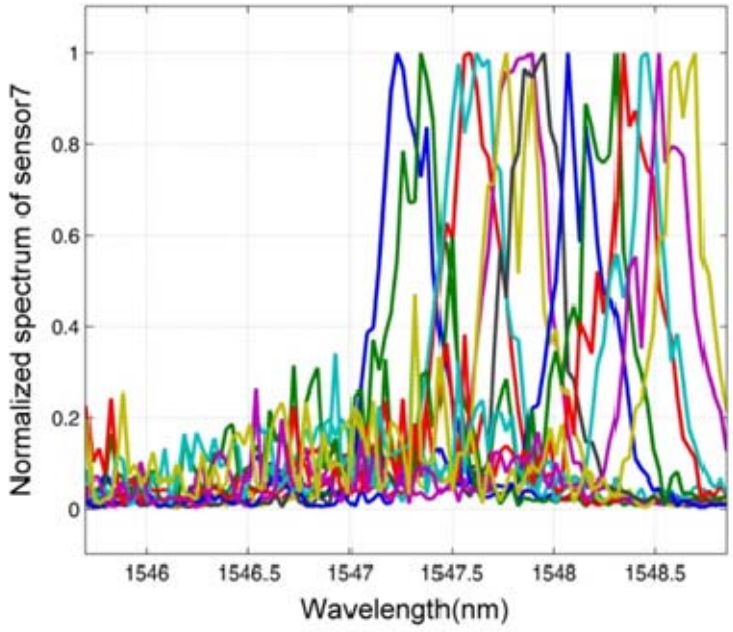

(b)

Figure 4.26 Information of 7th FBG (a) Fitted curve of shift wavelength (b) Reconstructed spectra

Chapter 5 Conclusion

5.1 Conclusion

In this work, a wavelength-scanning time division multiplexing (WSTDM) sensor network based on ultra-weak FBGs was proposed and experimentally demonstrated. The low insertion loss and the negligible crosstalk enable more than one thousand FBGs to be multiplexed serially. The sensing principle was based on the detection of Bragg wavelength shift, and the sensors in the array were distinguished by different time delays. With this approach, a 1000-sensor network was constructed and demonstrated with temperature measurement. The innovation and contribution of this work is summarized below:

Theoretical analysis of multiplexing capability: The multiplexing capability of a serial TDM FBG network is mainly affected by two factors: the insertion loss of the upstream FBGs and the crosstalk between FBGs. If we assume all the FBGs are identical, these two factors are related to the peak reflectivity of each FBG. To understand the relationship between the multiplexing capability and the peak reflectivity, detailed theoretical analysis and simulation aiming to maximize the FBG multiplexing number in a single fiber was performed.

Automatic FBG fabrication system: To experimentally demonstrate the technical feasibility of multiplexing of a very large number of ultra-weak FBGs, a system for efficient and quality fabrication of weak FBGs is required.. To fulfill this need, an automated FBG fabrication system was designed, implemented, tested and made into operation to meet this mass production requirement. There are four key functional parts in the system: fiber feeding system, coating removal system, FBG writing system and fiber collection system. The fiber feeding system uses stepper motors and gears to move an optical fiber accurately to locations where the FBGs are fabricated. The coating removal system is based on the heating effect of a CO2 laser, which chemically decomposes and evaporates the coating of a selected section on the optical fiber. The FBG writing system is based on the UV photosensitivity of the fiber. A phase-mask is placed between the UV light and the optical fiber to produce a periodic interference

pattern, which further modulates the refractive index along the fiber periodically. The fiber collection system is driven by a linear motor and the fiber can be wound around a spool tightly and smoothly at a moderate speed. The whole FBG fabrication system is controlled and synchronized by a computer via some interface circuits and a Graphical User Interface (GUI) program. With this system, it takes only 48 seconds to fabricate one FBG, and up to 500 FBGs can be made continuously. This number was mainly limited by the maximum continuous and consistent working time of the excimer laser we used instead of the system capability. The FBG writing efficiency can be further improved by the use of a more powerful excimer laser.

Interrogation system: Another major component of this dissertation is to construct an FBG interrogation system with the capability of detecting weak high frequency signal. The input light is modulated into pulses to distinguish different FBGs, and the pulse width determines the spatial resolution. To achieve 10 centimeter spatial resolution, the pulse width should be on the order of one nanosecond, corresponding to high frequency (GHz) detection signal. In addition, the FBGs have very low reflectivity, which results to the weak reflected pulse signal. The developed interrogation system has the capability to detect the weak FBG with the peak reflectivity as low as -55dB.

Demonstration of distributed sensing: The feasibility of 1000-multiplexed FBG sensor network was experimentally demonstrated and distributed temperature sensing was realized. Besides the demonstrated distributed temperature measurement, the reported method can also be applied to measure other parameters, such as strain.

References

1. Sohn, H. and L.A.N. Laboratory, *A review of structural health monitoring literature: 1996-2001*. 2004: Los Alamos National Laboratory Los Alamos,, New Mexico.
2. Balageas, D., et al., *Structural health monitoring*. Vol. 493. 2006: Wiley Online Library.
3. Lee, J.R., S.S. Lee, and D.J. Yoon, *Simultaneous multipoint acoustic emission sensing using fibre acoustic wave grating sensors with identical spectrum.* Journal of Optics A: Pure and Applied Optics, 2008. **10**: p. 085307.
4. Giurgiutiu, V., A. Zagrai, and J.J. Bao, *Piezoelectric wafer embedded active sensors for aging aircraft structural health monitoring.* Structural Health Monitoring, 2002. **1**(1): p. 41-61.
5. Kim, S., et al. *Health monitoring of civil infrastructures using wireless sensor networks*. 2007: Ieee.
6. Bocca, M., et al. *A reconfigurable wireless sensor network for structural health monitoring*. 2009.
7. Bates, J., G. Gruzalski, and C. Luck. *Rechargeable solid state lithium microbatteries*. 1993: IEEE.
8. Suster, M., W.H. Ko, and D.J. Young. *Optically-powered wireless transmitter for high-temperature MEMS sensing and communication*. 2003: IEEE.
9. Lee, D.G., et al., *Characterization of fiber optic sensors for structural health monitoring.* Journal of composite materials, 2002. **36**(11): p. 1349-1366.
10. FROGGATT, M., et al. *High density strain sensing using optical frequency domain reflectometry*. 2000: Society of Photo-Optical Instrumentation Engineers.
11. Grattan, K.T.V., *Optical fiber sensor technology: devices and technology*. Vol. 2. 1997: Springer.
12. Chester, A., S. Martellucci, and A. Scheggi, *Optical fiber sensors*. 1967: Nijhoff.
13. Golnabi, H., *Mass measurement using an intensity-modulated optical fiber sensor.* Optics and Lasers in Engineering, 2002. **38**(6): p. 537-548.
14. Kurosawa, K. and K. Shirakawa, *Intensity modulation type optical sensor and optical current/voltage sensor*. 2006, Google Patents.
15. Kurashima, T., et al., *Brillouin optical-fiber time domain reflectometry.* IEICE transactions on communications, 1993. **76**(4): p. 382-390.
16. Dakin, J., et al., *Distributed optical fibre Raman temperature sensor using a semiconductor light source and detector.* Electronics Letters, 1985. **21**(13): p. 569-570.
17. Kersey, A.D., T. Berkoff, and W. Morey, *Multiplexed fiber Bragg grating strain-sensor system with a fiber Fabry—Perot wavelength filter.* Optics Letters, 1993. **18**(16): p. 1370-1372.
18. Barnett, J., S. Block, and G. Piermarini, *An Optical Fluorescence System for Quantitative Pressure Measurement in the Diamond‐Anvil Cell.* Review of Scientific Instruments, 1973. **44**(1): p. 1-9.

19. Dils, R.R., *Blackbody radiation sensing optical fiber thermometer system*. 1988, Google Patents.
20. Thompson, R., *Fluorescence sensors and biosensors*. 2006: CRC.
21. Lo, Y. and T. Yu, *A polarimetric glucose sensor using a liquid-crystal polarization modulator driven by a sinusoidal signal.* Optics communications, 2006. **259**(1): p. 40-48.
22. Enokihara, A., M. Izutsu, and T. Sueta, *Optical fiber sensors using the method of polarization-rotated reflection.* Lightwave Technology, Journal of, 1987. **5**(11): p. 1584-1590.
23. Choi, H.S., H.F. Taylor, and C.E. Lee. *High performance fiber optic temperature sensor using low-coherence interferometry*. 1997: Optical Society of America.
24. Qi, B., et al. *Fiber optic pressure and temperature sensors for oil down hole application*. 2002: Spie.
25. Kyuma, K., et al., *Fiber-optic current and voltage sensors using a Bi12GeO20single crystal.* Lightwave Technology, Journal of, 1983. **1**(1): p. 93-97.
26. Cibula, E., D. Donlagic, and C. Stropnik. *Miniature fiber optic pressure sensor for medical applications*. 2002: IEEE.
27. Jacobson, K.B., *Biosensors and other medical and environmental probes.* ONRL Center for Biotechnology.[Online]. Available: http://www. ornl. gov/ORNLReview/rev29_3/text/biosens. htm, 2003.
28. Culshaw, B., *Fiber optics in sensing and measurement.* Selected Topics in Quantum Electronics, IEEE Journal of, 2000. **6**(6): p. 1014-1021.
29. Juarez, J.C., et al., *Distributed fiber-optic intrusion sensor system.* Journal of Lightwave Technology, 2005. **23**(6): p. 2081.
30. Takada, K., *High-resolution OFDR with incorporated fiber-optic frequency encoder.* Photonics Technology Letters, IEEE, 1992. **4**(9): p. 1069-1072.
31. Murayama, H., et al. *Distributed strain measurement with high spatial resolution using fiber bragg gratings and optical frequency domain reflectometry*. 2006: Optical Society of America.
32. Duncan, R.G., et al. *OFDR-based Distributed Sensing and Fault Detection for Single-and Multi-mode Avionics Fiber-optics*.
33. Hartog, A., *A distributed temperature sensor based on liquid-core optical fibers.* Lightwave Technology, Journal of, 1983. **1**(3): p. 498-509.
34. Froggatt, M.E., *Calculation of birefringence in a waveguide based on Rayleigh scatter*. 2008, Google Patents.
35. Rogers, A., *Polarization-optical time domain reflectometry: A technique for the measurement of field distributions.* Applied Optics, 1981. **20**(6): p. 1060-1074.
36. Niklès, M. *Fibre optic distributed scattering sensing system: Perspectives and challenges for high performance applications*. 2007: International Society for Optical Engineering; 1999.
37. Bao, X. and L. Chen, *Recent progress in Brillouin scattering based fiber sensors.* Sensors, 2011. **11**(4): p. 4152-4187.
38. Murphy, V., et al., *Quasi-distributed fibre-optic chemical sensing using telecom optical fibre.* Electronics Letters, 1997. **33**(7): p. 618-619.

39. Li, H.N., D.S. Li, and G.B. Song, *Recent applications of fiber optic sensors to health monitoring in civil engineering.* Engineering structures, 2004. **26**(11): p. 1647-1657.
40. Tjin, S., et al., *Application of quasi-distributed fibre Bragg grating sensors in reinforced concrete structures.* Measurement Science and Technology, 2002. **13**: p. 583.
41. Na, X.P.P.F.C. and C.Z.W. Tingyun, *A Quasi-Distributed Optical Fiber Temperature Sensor Based on Fresnel Reflection [J]*. Chinese Journal of Lasers, 2008. **12**.
42. Huang, Z., et al., *Intrinsic Fabry-Pe´ rot fiber sensor for temperature and strain measurements.* Photonics Technology Letters, IEEE, 2005. **17**(11): p. 2403-2405.
43. Gangopadhyay, T.K., *Prospects for fibre Bragg gratings and Fabry-Perot interferometers in fibre-optic vibration sensing.* Sensors and Actuators A: Physical, 2004. **113**(1): p. 20-38.
44. Li, W., et al., *Differential pulse-width pair BOTDA for high spatial resolution sensing.* Optics Express, 2008. **16**(26): p. 21616-21625.
45. Farahani, M.A. and T. Gogolla, *Spontaneous Raman scattering in optical fibers with modulated probe light for distributed temperature Raman remote sensing.* Journal of Lightwave Technology, 1999. **17**(8): p. 1379.
46. Kersey, A.D., et al., *Fiber grating sensors.* Lightwave Technology, Journal of, 1997. **15**(8): p. 1442-1463.
47. Zhao, Y., Y. Liao, and S. Lai, *Simultaneous measurement of down-hole high pressure and temperature with a bulk-modulus and FBG sensor.* Photonics Technology Letters, IEEE, 2002. **14**(11): p. 1584-1586.
48. Ferraro, P. and G. De Natale, *On the possible use of optical fiber Bragg gratings as strain sensors for geodynamical monitoring.* Optics and Lasers in Engineering, 2002. **37**(2): p. 115-130.
49. Schroeder, R.J., T. Yamate, and E. Udd. *High pressure and temperature sensing for the oil industry using fiber Bragg gratings written onto side hole single mode fiber*. 1999: SPIE INTERNATIONAL SOCIETY FOR OPTICAL.
50. Kurtaran, S. and M.S. Kılıçkaya, *The modelling of Fiber Bragg Grating.* Optical and Quantum Electronics, 2007. **39**(8): p. 643-650.
51. McCall, M., *On the application of coupled mode theory for modeling fiber Bragg gratings.* Journal of Lightwave Technology, 2000. **18**(2): p. 236.
52. Liu, G.J., et al., *Transfer matrix method analysis of apodized grating couplers.* Optics communications, 2004. **235**(4): p. 319-324.
53. Kogelnik, H., *2. Theory of dielectric waveguides.* Integrated Optics, 1975: p. 13-81.
54. Skaar, J., *Synthesis and characterization of fiber Bragg gratings*. 2000: NTNU.
55. Qiu, Y. and Y. Sheng, *Fiber Bragg Grating Modeling.*
56. Lloyd, G.D., et al., *Resonant cavity time-division-multiplexed fiber Bragg grating sensor interrogator.* Photonics Technology Letters, IEEE, 2004. **16**(10): p. 2323-2325.
57. Chan, C., et al., *Intrinsic crosstalk analysis of a serial TDM FGB sensor array by using a tunable laser.* Microwave and Optical Technology Letters, 2003. **36**(1): p. 2-4.

58. Yi, A.L., et al. *A novel scheme for all-optical automatic polarization division demultiplexing*. 2009: IEEE.
59. Guan, Z.G., D. Chen, and S. He, *Coherence multiplexing of distributed sensors based on pairs of fiber Bragg gratings of low reflectivity.* Lightwave Technology, Journal of, 2007. **25**(8): p. 2143-2148.
60. Hu, Y., et al., *Multiplexing Bragg gratings using combined wavelength and spatial division techniques with digital resolution enhancement.* Electronics Letters, 1997. **33**(23): p. 1973-1975.
61. Nunes, L., et al., *FBG sensor multiplexing system based on the TDM and fixed filters approach.* Sensors and Actuators A: Physical, 2007. **138**(2): p. 341-349.
62. Henderson, P., et al. *Highly-multiplexed grating-sensors for temperature-referenced quasi-static measurements of strain in concrete bridges*. 1999: Spie-Int Soc Optical Engineering.
63. Koo, K., A. Tveten, and S. Vohra, *Dense wavelength division multiplexing of fibre Bragg grating sensors using CDMA.* Electronics Letters, 1999. **35**(2): p. 165-167.
64. Cooper, D.J.F., T. Coroy, and P.W.E. Smith, *Time-division multiplexing of large serial fiber-optic Bragg grating sensor arrays.* Applied Optics, 2001. **40**(16): p. 2643-2654.
65. Wang, Y., et al., *A Quasi-Distributed Sensing Network With Time-Division-Multiplexed Fiber Bragg Gratings.* Photonics Technology Letters, IEEE, 2011. **23**(2): p. 70-72.
66. Chan, C.C., W. Jin, and M.S. Demokan, *Experimental investigation of a 4-FBG TDM sensor array with a tunable laser source.* Microwave and Optical Technology Letters, 2002. **33**(6): p. 435-437.
67. Chan, C., W. Jin, and M. Demokan, *Experimental investigation of a 4 FBG TDM sensor array with a tunable laser source.* Microwave and Optical Technology Letters, 2002. **33**(6): p. 435-437.
68. Inoue, A., et al., *Fabrication and Application of Fiber Bragg Grating - a Review.* Optoelectronics-Devices and Technologies, 1995. **10**(1): p. 119-130.
69. Kashyap, R., *Fiber Bragg gratings*. 2nd ed. 2010, Burlington, MA: Academic Press. xviii, 614 p.
70. Kohnke, G., et al. *Photosensitization of optical fiber by UV exposure of hydrogen loaded fiber*. 1999: IEEE.
71. Nguty, T.A. and R.J. Potton, *Photochemical changes in hydrogen-loaded optical fibres with application to Bragg grating formation.* Measurement Science & Technology, 1997. **8**(10): p. 1055-1058.
72. Grobnic, D., et al., *Sapphire fiber Bragg grating sensor made using femtosecond laser radiation for ultrahigh temperature applications.* Ieee Photonics Technology Letters, 2004. **16**(11): p. 2505-2507.
73. Gharib, B., et al., *Anti-inflammatory properties of molecular hydrogen: investigation on parasite-induced liver inflammation.* Comptes Rendus de l'Académie des Sciences-Series III-Sciences de la Vie, 2001. **324**(8): p. 719-724.
74. Park, H.S., et al., *Noncontact optical fiber coating removal technique with hot air stream.* Journal of Lightwave Technology, 2005. **23**(2): p. 551-557.

75. Koster, E.H.M., et al., *Fibers coated with molecularly imprinted polymers for solid-phase microextraction.* Analytical Chemistry, 2001. **73**(13): p. 3140-3145.
76. Matthewson, M.J., C.R. Kurkjian, and J.R. Hamblin, *Acid stripping of fused silica optical fibers without strength degradation.* Journal of Lightwave Technology, 1997. **15**(3): p. 490-497.
77. Dadsetan, M., H. Mirzadeh, and N. Sharifi, *Effect of CO2 laser radiation on the surface properties of polyethylene terephthalate.* Radiation Physics and Chemistry, 1999. **56**(5-6): p. 597-604.
78. Chattopadhyay, D.K., S.S. Panda, and K.V.S.N. Raju, *Thermal and mechanical properties of epoxy acrylate/methacrylates UV cured coatings.* Progress in Organic Coatings, 2005. **54**(1): p. 10-19.
79. Zhou, C.T., Xinglin; Jiang, Desheng; Peng, Renxiang, *Theoretical and experimental investigation of optical fiber coatings removal by laser irradiation*, in .*Proceedings of the SPIE*. 2005. p. 544-551.
80. Singh, N., et al., *Fibre Bragg grating writing using phase mask technology.* Journal of Scientific & Industrial Research, 2005. **64**(2): p. 108-115.
81. Toliyat, H.A. and G.B. Kliman, *Handbook of electric motors*. 2nd ed. 2004, New York: Marcel Dekker. xxi, 805 p.
82. Keiser, G., *Optical fiber communications*. 2000: Wiley Online Library.
83. Gong, J.M., et al., *Enhancement of wavelength detection accuracy in fiber Bragg grating sensors by using a spectrum correlation technique.* Optics Communications, 2002. **212**(1-3): p. 29-33.